5-2017

Properties and Manipulation of Ionic Liquid-Solid Interfaces in Complex Oxide Materials

Anthony Thomas Wong
University of Tennessee, Knoxville, awong7@vols.utk.edu

To the Graduate Council:

I am submitting herewith a dissertation written by Anthony Thomas Wong entitled "Properties and Manipulation of Ionic Liquid-Solid Interfaces in Complex Oxide Materials." I have examined the final electronic copy of this dissertation for form and content and recommend that it be accepted in partial fulfillment of the requirements for the degree of Doctor of Philosophy, with a major in Materials Science and Engineering.

Philip D. Rack, Major Professor

We have read this dissertation and recommend its acceptance:

Thomas Zac Ward, David G. Mandrus, Claudia J. Rawn

Accepted for the Council:

Dixie L. Thompson

Vice Provost and Dean of the Graduate School

(Original signatures are on file with official student records.)

Properties and Manipulation of Ionic Liquid–Solid Interfaces in Complex Oxide Materials

A Dissertation Presented for the

Doctor of Philosophy

Degree

The University of Tennessee, Knoxville

Anthony Thomas Wong

May 2017

Dedication

To my loving wife Jessica who chose to join me in this adventure through school and through life...

To my parents and my brothers who have always supported me...

Abstract

Ionic liquids are liquid salts that are bringing rapid changes to the field of solid electronic materials. The implementation of ionic liquids in conjunction with these solid materials produces interfacial effects, especially when a bias is applied across the ionic liquid, forming an electric double layer. Electric double layers in ionic liquids are unique in their formation and the interfacial charges that are orders of magnitude higher than conventional techniques they can impart, providing new techniques for device design and implementation. In chapter 1, the fundamentals of the solid state electronic and magnetic materials are introduced, along with ionic liquids, and their essential properties that make them appropriate for use with solid films. Chapter 2 discusses the geometric impacts that should be taken into consideration when designing electric double layer devices, determining that the gate area to device area ratio plays the greatest role. Chapter 3 explores the application of electric double layer interfacial effects on ferroelectric lead zirconate-titanate films. The demonstrated large area switching, coupled with the minimal changes to film quality, and use on low quality films make this ionic liquid-solid interface an exciting proposition for future study and applications. Chapter 4 uses the same electric double layer to interrogate the ability to produce stoichiometry induced crystallographic transformations in strontium cobaltite family of films. Chapter 5 evaluates an antiferromagnetic lanthanum-strontium manganite that shows an unprecedented anisotropic magnetoresistance. These materials are excellent candidates for future spin based devices. The work discussed in this dissertation

demonstrates a wide range of possible applications that can be affected by the use of ionic liquid solid interfaces, while also showing diversity in the types of studies and measurements that can be conducted by ionic liquids. Combining the electrostatic and electrochemical capabilities of ionic liquids with complex oxide films, the manipulation oxide properties can lead to advances in future electronic and magnetic properties and applications.

Table of Contents

List of Tables

List of Figures

Chapter 1

Introduction

1.1 Complex Oxide Materials

Electronic and magnetic materials are ubiquitous in the modern world, and they are the driving force for technological advances in society. The vast majority of electronic materials consist of relatively simple materials including metal conductors, silicon based semiconductors and oxide insulators, the building blocks of electronic circuits. These materials have been studied immensely since their discovery as electronic devices in the middle 20^{th} century[1]. While these original solid state electronic devices originated in a size that would seem enormous today, advancements in technology allowed these devices to rapidly shrink to the point that the mobile devices we carry today are more than 10^5 times more powerful than computers that previously required entire rooms[2, 3].As early as 1965, Gordon Moore predicted this miniaturization[4], and later correctly predicted the bi-annual doubling of logic device density[5] and therefore computing power. This trend has amazingly held constant through to today and depicted in figure 1.1. Despite advances in silicon processing technology, we are rapidly approaching the physical limitations of silicon with the 2015 announcement of 7 nm device nodes, and the theoretical limit for silicon being at approximately 4 nm[2, 3]. Because of this fast approaching limitations, new electronic

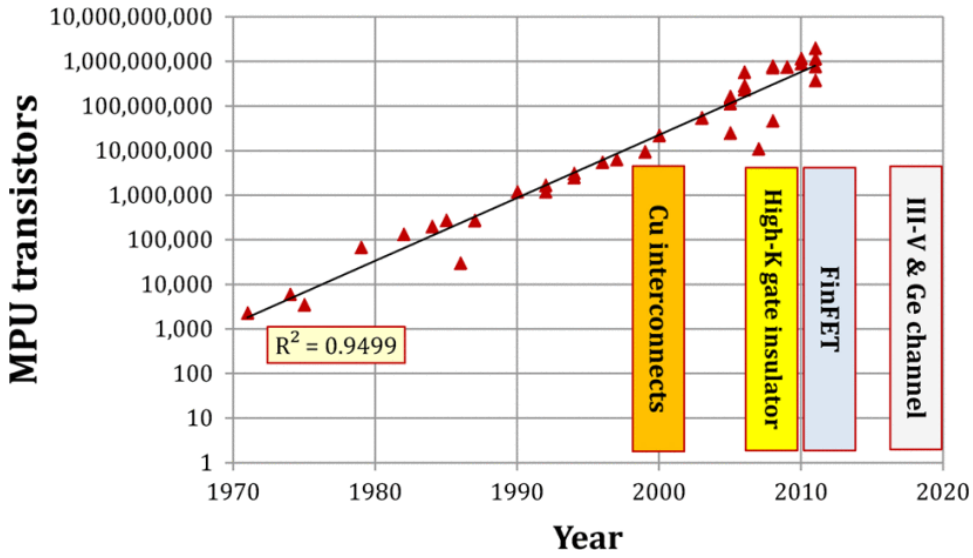

Figure 1.1: The number of transistors per microprocessor chip versus time, showing introduction of new enabling technologies. Figure from [2]

materials, and device types will be required for continuing Moore's law, and advancing functional devices.

Complex oxides are a group of materials that could revolutionize the electronic device industry due to the wide variety of interesting and useful properties, many different techniques that can be used in manipulating these properties, and the possibility of multimodal and tailored functionality to overcome Moore's law[6]. The interest in these materials does not end at miniaturization of next generation electronics, but stretches throughout the range of physics exhibited, including electronic, magnetic, and structural studies, in addition to the complex and intertwined nature of how these properties are manifested. Correlated oxides typically consist of 3 or more elemental components, two metals, often based around transition metals eith either 3d, 4d, or 5d electrons, bonded with oxygen. These oxides are characterized by their strong interactions between multiple different degrees of freedom – spin, charge, lattice, and orbital – unlike the interactions seen in "simple" or more conventional electronic materials[7].

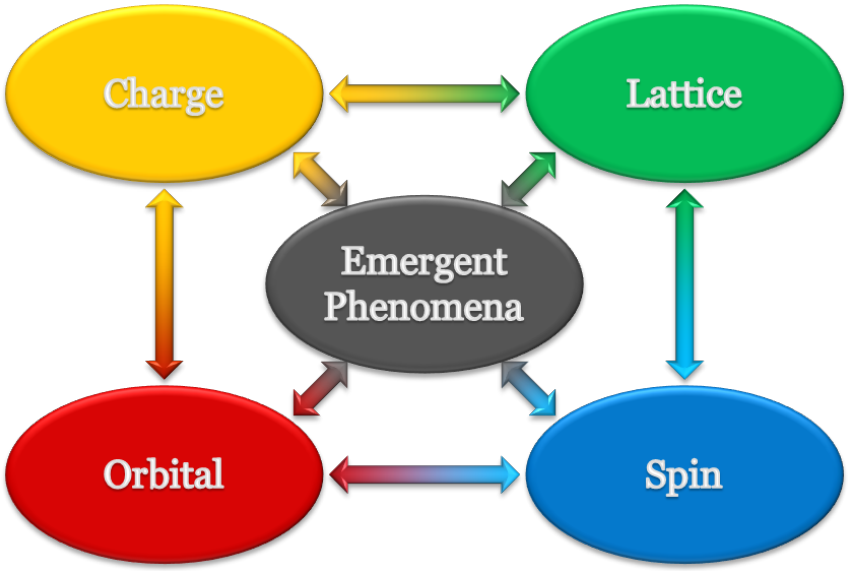

Figure 1.2: Schematic depiction of the degrees of freedom in complex oxide materials.

1.1.1 Order Parameter Degrees of Freedom

The intricacies of complex oxide materials come from the strongly correlated interactions between the varying degrees of freedom that occur in these materials, affecting the emergent phenomenological properties exhibited (In section 1.1.3)[8]. The degrees of freedom include charge, lattice, orbital and spin, and the correlations between these parameters provide various methods of controlling the behaviors of complex transition metal oxides.

Transition metal oxides (TMO) are made up of transition metals which are characteristic for their unfilled d-orbitals. The perovskite crystal strucutre can be viewed as a stereotypical crystal lattice for complex oxides, as many of the structures are paralleled in other structures such as the Ruddelsen-Popper series, and spinnels. In perovskite crystals the transition metal d-orbitals bond with the oxygen p-orbitals to form MO_6 octahedra, and inducing crystal field splitting, separating the energy degeneracy between the e_g and t_{2g} orbitals, where the e_g orbitals point towards the oxygen in the octahedra $(d_{x^2-y^2}, d_{z^2-r^2})$, while the t_{2g} orbitals point to the spaces between them (d_{zx}, d_{yz}, d_{xy}) and are depicted in figure 1.3[8].

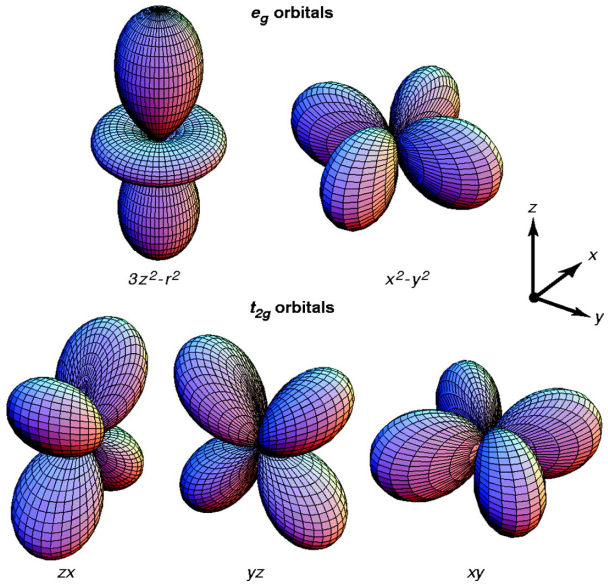

Figure 1.3: Depictions of d-orbital shapes from [8]

When the degeneracy of the d-orbitals is lifted, the orbital filling, guided by Hund's rule of filling which states that every orbital at the same energy level must have 1 electron before any take on a second, becomes integral in determining material properties[8, 9]. Beyond crystal field splitting the d-orbitals are coupled to the lattice, and are affected by Jahn-Teller distortion that further lifts orbital degeneracy when the lattice is changed[8–11]. These energy changes inform the electron filling, which can bring different spin states and magnetic ordering. Bonding with the oxygen p-orbitals also produce an additional layer of complexity as the bond angles and bond lengths impact the magnetic ordering following RKKY, double-exchange, and superexchange contributions. These coupled interactions make complex oxides a rich field of physics on every length scale, going from macroscopic, to nanoscopic, and in an emergent length scale - mesoscopic - which behaves differently than either the macro or nanoscales and could be integral in bridging quantum mechanics and classical mechanics. All these effects lead to phenomena such as Mott insulating states, high temperature superconductivity, colossal magnetoresistance, and metal insulator transitions.

1.1.2 Order Parameter Control

The strong correlations between all the different ordering parameters lead to unique, complex material physics, and a broad range of techniques capable of manipulating these properties. While each of these degrees of freedom can be manipulated individually, the strong correlations cause indirect control of other order parameters. This makes it hard to directly control one single order parameter, and often, combinations of multiple control techniques are implemented to achieve the desired material properties.

Strain

Strain, in the case of thin film manipulation, refers to the change of lattice parameter as compared to the bulk parameters of the material. Lattice strains can induce Jahn-Teller like distortions in the metal-oxide octahedra, effecting the orbital filling, and charge distribution in the crystal[8, 11, 12]. Additionally, strain can have a significant impact on the bond angles in the crystal lattice, and the rotation of the octahedra, affecting transport paths and electron exchange properties through shifts in the orbital degeneracy[13–15].

Epitaxy Induced Strain

Epitaxy induced strain is method of controlling thin film strain by growing films on substrates that have slightly dissimilar lattice constants to the film being grown. Perovskite oxides are commonly manipulated in this fashion by changing the substrates on which they are grown – a list of common substrates and their lattice parameters listed in table 1.1[8, 12]. The substrates lattice parameters can be matched directly to the film such as $[100]_{\text{substrate}} = [100]_{\text{film}}$ or films can be grown on a matching crystallographic substrate orientation such as $[110]_{\text{substrate}} = [100]_{\text{film}}$ depicted in figure 1.4. While there are a broad range of substrates available, especially considering the different substrate facets and arrangements, there is still in relative

Table 1.1: Table of common substrates, crystal structure and lattice constants in order of increasing a lattice parameter (values taken from CrysTec GmbH substrate supplier)

Perovskite Substrates	**Structure**	**a (Å)**	**b (Å)**	**c (Å)**
$LaAlO_3$	cubic	3.82	3.82	3.82
LSAT	cubic	3.87	3.87	3.87
$SrTiO_3$	cubic	3.91	3.91	3.91
$YAlO_3$	orthorombic	5.18	5.31	7.35
$NdGaO_3$	orthorombic	5.43	5.5	7.71
$GdScO_3$	orthorombic	5.45	5.75	7.93
$DyScO_3$	orthorombic	5.54	5.71	7.89

Other Oxide Substrates	**Structure**	**a (Å)**	**b (Å)**	**c (Å)**
$SrLaAlO_4$	tetragonal	3.75	3.75	12.63
$SrLaGaO_4$	tetragonal	3.84	3.84	12.68
MgO	cubic	4.21	4.21	4.21
TiO_2 - Rutile	tetragonal	4.59	4.59	2.96
Al_2O_3	hexagonal	4.76	4.76	13.00
Y:ZrO_2 - YSZ	cubic	5.12	5.12	5.12
$LiNbO_3$	trigonal	5.15	5.15	13.86
$LiTaO_3$	trigonal	5.15	5.15	13.78
$LiAlO_2$	trigonal	5.17	5.17	6.26
$LiGaO_2$	orthorombic	5.41	5.01	6.38
$MgAl_2O_4$ - Spinel	cubic	8.09	8.09	8.09
YAG - $Y_3Al_5O_{12}$	cubic	12.00	12.00	12.00
$Gd_3Ga_5O_{12}$	cuic	12.38	12.38	12.38

terms a very small number of strain states accessible for any crystal growth. If the mismatch (difference between the film lattice and the substrate lattice) is too large, the grown film will not align epitaxial to the substrate, instead growing in a relaxed state more similar to the bulk. Relaxation will also naturally occur in thick films as the distance from the substrate increases[16]. As an interfacial effect, epitaxial strain is imparted on the in-plane lattice of the grown film however the out of plane film is also affected in a complimentary way due to a Poisson effect. Tensile in-plane strain causes the out of plane axis to compress, while compressive in-plane strain causes the out of plane axis to expand, making expitaxial strain an ineffective method of controlling strain along a single crystal axis[8].

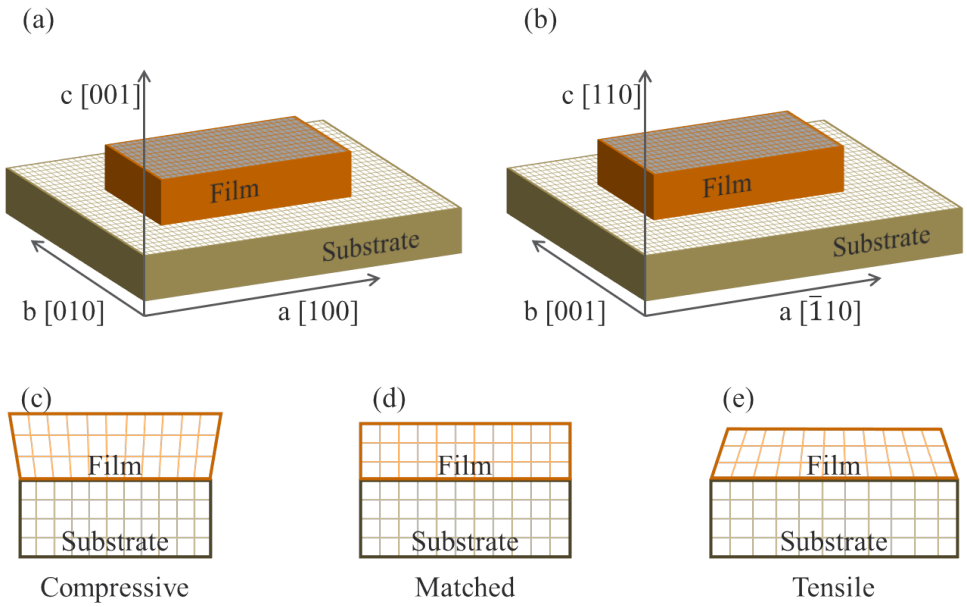

Figure 1.4: Schematic of epitaxial growth: a. Direct lattice matching ($[100]_{\text{substrate}} = [100]_{\text{film}}$) b. Transposed lattice matching ($[110]_{\text{substrate}} = [100]_{\text{film}}$) c. Compressive strained film d. Lattice matched film e. Tensile strained film

Substitution Chemical Pressure Strain

Chemical pressure strain involves using an isovalent atom (one with a similar electronic valency) substitutionally in the lattice of the crystal during growth, for example replacing Ca^{2+} with the larger Sr^{2+})[17]. The strain effects from doping are applied as a long range effect throughout the film. The strain caused by isovalent substitution is relatively small, however there can be large effects on the bond angles and octahedra rotations[13].

Helium Ion Induced Strain (Strain Doping)

Strain doping is an innovative new way of introducing continuous strain control to thin films. He is a small, inert noble gas atom that is ionized and accelerated through standard ion gun techniques into the lattice of the film. The depth of the implanted atoms can be controlled by the ion gun's accelerating voltage, and the thickness of the grown capping layer thickness, while the number of implanted ions can be

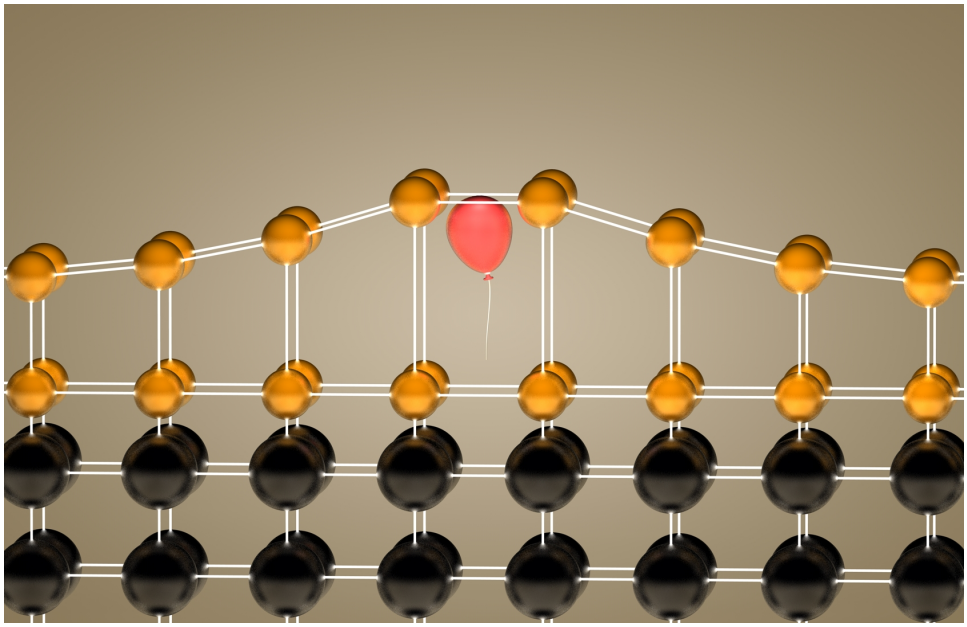

Figure 1.5: Schematic of helium ion implantation in which the helium designated by a balloon sits interstitial within the lattice of the film.

controlled by the dosage, in which ion current or time exposed to the ion source can be varied for specific control[18, 19]. Because He is inert, it does not bond chemically to the crystal lattice, but rather sits interstitial inside the crystal structure causing an internal pressure that is alleviated through an expansion of the lattice as illustrated in figure 1.5. Lattice expansions upward of 2% are achievable with only 1 He atom per 130 unit cells[18–20]. The low energy used in implantation is small enough to minimize sputtering, in conjunction with a thin gold cap which additionally provides electrons to neutralize the He ions and attenuates the ion energy as the ions enter the crystal[18, 19]. Using a flood gun, He ions can be applied globally or using directed ion sources, such as a helium ion microscope, local areas of strain can be directly written into the film. In the case of epitaxial films, the in plane lattice parameters are epitaxially locked to the underlaying substrate which leaves only the free surface out of plane direction capable of expanding; therefore strain doping with He ions allows for the first time a continuously controllable single axis strain[18–20].

Electronic Control

Electronic controls of complex oxide materials are those that directly effect the electrons in the system. This can be done by modulating the electrons globally in the crystal system, through changing the Fermi level, or by manipulating the local electron density of states.

Doping

Electronic doping is a technique that uses chemical substitution where the substitution element has a change in valency as compared to the parent atom that it is replacing. A famous example of doped materials is in Si semiconductors. Si has 4 valence electrons and a band gap of 1.1eV. When a group III element is substituted, such as Ga, with 3 valence electrons, the crystal lattice has an electron deficiency, creating a hole in the crystal system and lowering the energy for hole conduction. These dopants are called acceptors as the create a state the accepts an electron. Conversely when a group V element is substituted, such as P, with 5 valence electrons, an additional electron is added into the crystal lattice, adding a free conduction electron in the system. These dopants are called donors as they donate an extra electron to the system[21].

In complex oxide materials, dopants are chemically bonded at much greater concentrations than the typical part per million done in silicon, such as perovkites where the rare earth in the RMO_3 commonly includes alkaline earth metals and lanthanides such as Sr and La. Looking at the $La_{1-x}Sr_xMnO_3$ (LSMO) phase diagram shows the power doping can have in complex oxide materials as the phase diagram crosses through metallic, insulating, and various magnetic ground states[22]. However, the correlated nature of complex materials also means that the size difference between the doping anion/cation can have a major influence on the local electronic state due to disorder effects.

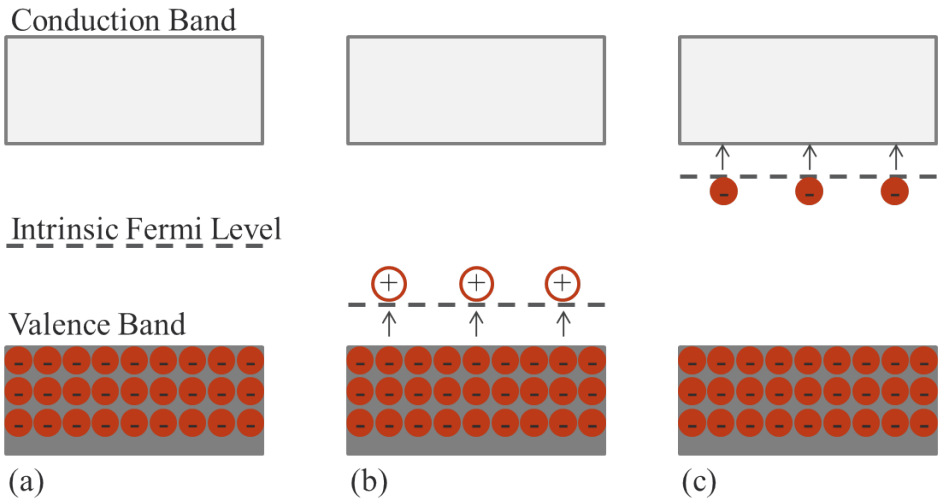

Figure 1.6: A simplified band diagram for silicon. (a) Intrinsic Si has a filled valence band, and empty conduction band. (b) P-type Si introduces accessible hole states moving the Fermi level close to the valence band. (c) N-type Si adds additional electrons that are easily mobilized into the conduction band, moving the Fermi level close to the conduction band.

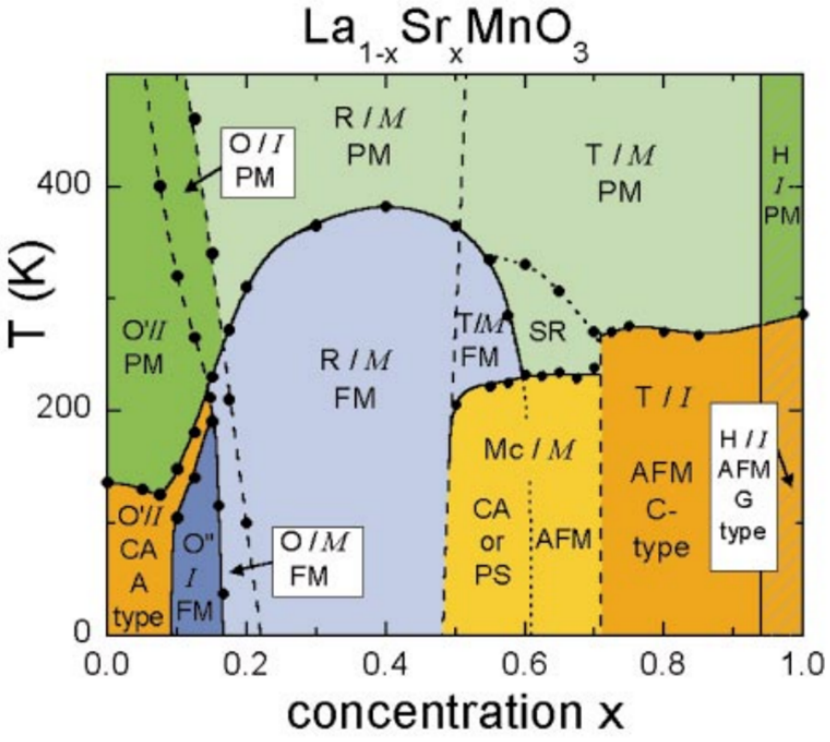

Figure 1.7: $La_{1-x}Sr_xMnO_3$ Phase Diagram from [22]

Electric Field Control

Electric field control is integral in modern electronics. In semiconductors, electric fields are used to modulate the carrier concentration at gated regions, and consequently modulate the conductivity of the material which is classified as a field effect transistor (FET). A common transistor construction is metal-oxide-semiconductor (MOSFET) where the metal is used to modulate the semiconductor, and the two are separated by an oxide insulator which is referred to as a gate dielectric. When a bias is applied between the metal electrode and the semiconductor, the charge is transferred through the gate dielectric, and causes either depletion or accumulation of electrons at the interface of the semiconductor and the gate dielectric depending on the polarity of the applied bias; this is called gating. In semiconductors this method of control has the capability of modulating the conductivity of the semiconducting channel by many orders of magnitude, creating electronic switches. In complex oxide materials this same technique can be utilized as a means of controlling electric and magnetic properties and phenomena[21].

Magnetic Control

Magnetic control of oxide materials can be difficult as it may require extremely large fields applied in order to affect the spin states of the materials. Ferromagnets have coercive fields of varying field strength, which smaller coercive fields being called "weak" ferromagnets and large coercive fields being called "strong" ferromagnets[21]. Antiferromagnets are generally insensitive to magnetic fields until the applied fields become extremely large. These extremely large fields can lead to a spin flip or spin flop effect which breaks the magnetic ordering, aligning the spins in the same direction[23, 24]. Application of these large magnetic fields require equipment which can produce these fields, meaning tightly coiled conductors and very large currents. These fields are commonly produced using superconducting magnets, where cooling power is an added layer of complexity.

Exchange Springs

Exchange springs are created by coupling a ferromagnetic material with an antiferromagnetic material. The interfacial ferromagnetic domains align to match the magnetic orientation of the connected antiferromagnetic material[25, 26]. The coercive field for ferromagnets is the field required to change the orientation of the magnetic domains, and antiferromagnets are relatively insensitive to applied magnetic fields and only change orientation at extremely high fields. By coupling these together, the antiferromagnet increases the coercive field of the ferromagnet, and can be used to manipulate an asymmetry of the hysteresis loop of the ferromagnet. Recent discoveries have created inventive uses for antiferromagnet-ferromagnet exchange springs such as tunneling devices[27].

Spin Torque Transfer

Spin transfer torque is a method coupling the magnetic control of a system with the electronic control. A hard or "fixed" ferromagnetic material polarizes the current that flows through this layer, and the spin polarized current then interacts with a softer or "free" magentic layer[28] illustrated in figure 1.8. When these layers align, the resistance of the stack remains low, however when these layers anti-align, the resistance state increases because of spin scattering. Spin transfer torque devices can be fabricated in all metal systems, and also in magnetic tunnel junctions. When the two magnetic layers are in the high resistance state, a sufficiently high current can apply a spin torque on the free magnetic layer, to cause it to precess or possibly reverse orientation. Used in a controlled fashion, these materials are capable of turning a DC voltage into an tunable AC voltage output[29].

Magnetic Nanoparticles

Magnetic nanoparticles provide another unique method of controlling magnetic and electron properties of some materials, as demonstrated using a $La_{0.7}Ca_{0.3}MnO_3$ film

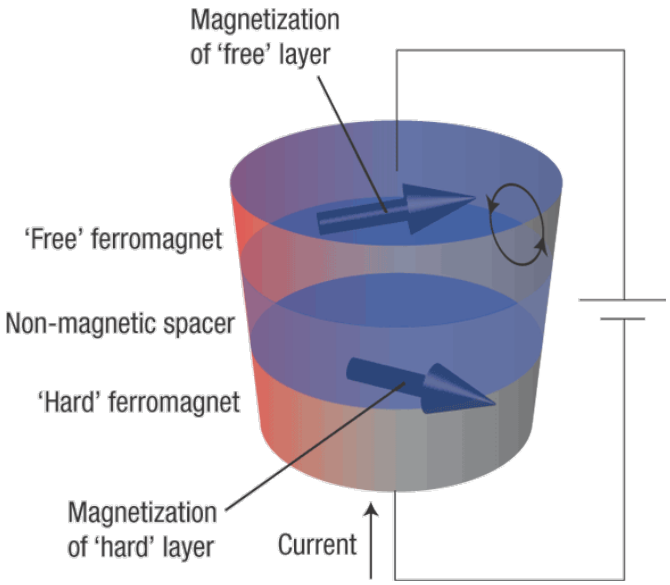

Figure 1.8: "The passage of a current through a 'hard' magnetic layer causes it to become spin-polarized. When this current is subsequently injected across a thin non-magnetic spacer layer and into a 'free' magnetic layer, the realignment of its polarization induces a torque on the magnetic moment of the free layer, causing it to precess and even reverse." from [29]

that undergoes an insulator metal transition when a magnetic field is applied [30]. Instead of using a global magnetic field, magnetic nanoparticles were deposited on the surface of the film, and created locally oriented regions of metallic film changing the global resistance of the film. A schematic of this is shown in figure 1.9. Tuning the conductivity this way provides percolative paths on the surface changing to overall film from an insulator to a metal thus, mesoscale manipulation dirves microscopic functionality[30].

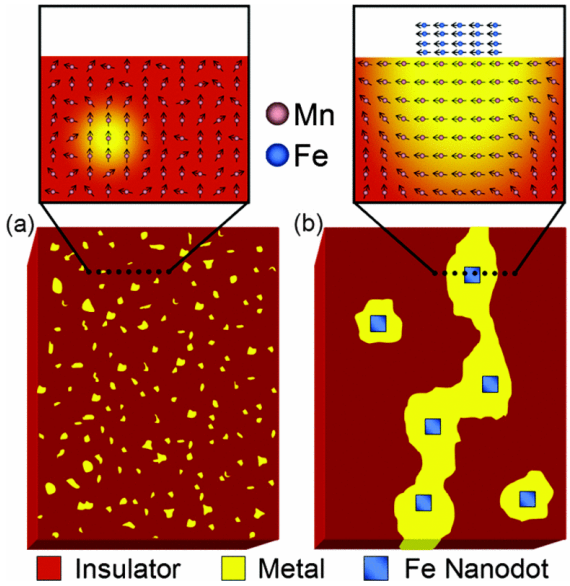

Figure 1.9: Ferromagnetic iron nanodots are applied on the surface of $La_{0.7}Ca_{0.3}MnO_3$ creating conducting channels through magnetic exchange from [30]

1.1.3 Phenomenological Properties

The correlated interactions, and various manipulation techniques in complex oxide materials provide for a means of accessing amazing phenomenological physical properties in these materials. Many of these properties come from competing coexisting electronic and magnetic phases within the crystals, along with more common structural phases. The phenomenological nature of these properties arise when the similar energetics of the competing order parameter mean that small perturbations can lead to dramatic material change. The changes can come in the form of a thermal energy, magnetic field, electric field, among other variable conditions. This section is not intended to discuss every property exhibited in oxides, as that list is rather extensive, but to discuss some of the most famous of these properties.

Coexistent Phase Separation

Phase transitions occur when materials undergo a spontaneous intrinsic change in phase of matter, crystal structure, magnetic ordering, or orbital ordering, among other transitions that occur in response to changes in conditions such as temperature or pressure. The best known phase transitions are changes in phase of matter including melting (going from a solid to a liquid) and boiling (changing from a liquid to a gas), however many materials undergo more subtle phase changes, such as crystal changes in iron going from Face centered cubic (FCC) to body centered cubic (BCC)[21]. The differences between some of the more obvious phase changes and the more subtle ones are described as first order and second order transitions. First order transitions have discontinuity in the first derivative of the free energy curve, and second order show the discontinuity in the second derivative of the free energy curve as the material changes from one phase to the next[21]. At specific conditions two phases coexist, for example at 100°C water can exist as both a liquid and a gas. This example can be extended to solid-solid, and second order phase changes such as resistive or magnetic phase changes. When the two coexistant phases have large changes in resistance, an important concept in electrical transport arises called percolative conduction[31, 32]. As current follows the path of least resistance, the electrons in phase separated systems will conduct through low resistance phases, causing a much lower resistance than would be expected from a simple rule of mixing type of calculation for average material resistance. One interesting method of measuring phase separated materials is by confining them geometrically to eliminate the percolation that occurs in large films. This allows for the measurement of individual domain transitions between resistance states seen as jumps in resistance curves[31, 32].

Metal Insulator Transitions

The most simplistic differentiation between metals and insulators in solid state physics comes from the band models for crystalline materials. In this explanation, electrons

in a crystal system are separated into bands. The Fermi level for these materials is the energy level at which the highest energy electrons are located. In metals, the Fermi energy is located within a band, meaning the band contains occupied and unoccupied states. The electrons can move between occupied and unoccupied states with a negligible change in energy creating the metallic state. In insulators the Fermi energy lies within a gap between two bands, meaning the lower energy band is occupied, and the higher energy band is completely unoccupied[21]. The energy gap between these two bands must be overcome in order for this material to conduct electrons, creating the insulating state. While this is often a good static model, it is not always applicable, particularly in systems in which the electron-electron interactions are not the driving force for the transition. Metal insulator transitions can be driven by crystallographic phase transitions in which the lattice and often the volume changes. Consequent changes to the degeneracy of the system can cause materials with no free electrons to gain free electrons as is seen in vanadium oxides[33–35]. Another way these transitions can occur is from sufficiently high electron potentials causing localization derived insulating states. Once an energy is provided to close a mobility gap as compared to a true band gap, electrons are delocalized and available for conduction. A good example of these types of insulator-metal transitions are seen in doped semi-conductors[36].

Mott Insulators

Mott insulators are an intriguing specific case of metal-insulator transitions. Mott insulators are materials predicted to be metals as they have unfilled valence bands producing available conduction electrons, however they are measured to be insulating materials due to the strong coulomb interactions experience by these conducting electrons preventing their motion through the crystal lattice[8]. Nevill Mott himself described this as "any transition from an antiferromagnetic insulator to a metal, as one essentially involving Hubbard-U"[33].

Colossal Magnetoresistance

Colossal magnetoresistance (CMR) in manganite films is an effect in which there is a colossal change (multiple orders of magnitude) in the material resistance under an applied magnetic field. These appear due to an orbital ordering under magnetic field which impacts the charge transfer properties of the Mn. Because the charge exchange carriers depend strongly on the magnetic order of the system, small perturbations in the magnetic field can cause large changes in the overall resistance. It is also noted that the coexistent phase separation of ferromagnetic metal phases, and antiferromagnetic insulator phases plays an important role, in these materials[37].

Magnetic Ordering

Magnetic order in materials is dependent on the orbital order, and the spin order for the materials. This gives rise to changes in magnetic order from changes in metal valence states in the crystal, but also from Jahn-Teller distortions that affect the orbital filling[8, 11]. There are also changes to these magnetic ordering parameters as the bond angles change[38]. An ideal system demonstrating these phenomena is the manganite perovskite which is defined by an ABO_3 structure where a-sites are often rare earth metals in the corners of a cubic unit cell, b-sites contain transition metals and are located in the center of the cubic unit cell, and the oxygen located at the face centers of the unit cell[8]. When the a-site is occupied by a combination of La and Sr, the material has an incredibly diverse phase diagram seen above in figure 1.7[22]. Sr has a +2 oxidation state and La has a +3 oxidation state, therefore the valence of the Mn changes in order to create the correct bonding in the crystal lattice. Coordination between the chemical ordering, valence states, and crystal structures moves manganites through all types of magnetic ordering going from paramagnetic at high temperature to a-type, c-type, g-type and phase separated antiferromagnetic, or ferromagnetic depending on the doping at low temperature[22].

Piezoelectrics

Piezoeletrics are a class of materials that have their lattice and charge coupled. Mechanical stresses in the crystal lattice produce an electric charge. These crystals also are affected by the converse effect, meaning an applied voltage can induce a mechanical strain. These effects arise from to displacements in the charge centers of the crystal as the strain is applied[21]. These materials are used in many applications including sensors, actuators, motors, and speakers among others.

Ferroelectrics

Ferroelectrics are a subclass of piezoelectric materials whose crystal structure has a broken centro-symmetric inversion symmetry. The non-centro-symmetric lattice means the center atom in the perovskite is offset from the center of the lattice, leading to a spontaneous polarization, an electronic analogue to ferromagnetic materials[21]. Just as ferromagnets have a coercive magnetic field required to change the magnetic orientation, ferroelectrics have a coercive electric field that is required to switch the film's polarization. These films have found numerous uses in modern applications such as motors, actuators, sensors and ultra-high K dielectrics in field effect transistors[39–42].

Multiferroics

Multiferroics are a combination of ferroelectric and ferromagnetic materials where the magnetic orientation and the electric polarization are coupled. The coexistence of these two phases is commonly a contradiction, as the magnetic component often leads to metallicity, while the electronic component requires the material to be a dielectric insulator[43]. The coupling of these two properties can be weak, and can exist from improper effects such as octahedral tilts, chiral or triangular orderings, and distortions, rather than purely electronic or ionic effects[44]. Multiferroics are a budding field which are theorized for numerous potential applications in part because

of the ability to use electric fields to control magnetic moments and *vice versa*, which could open the door for advanced magnetoelectric devices such as magnetic random access memory[43, 44].

Superconductivity

The origin of superconductivity in oxide materials is still under exploration as the BCS theory does not remain true for high temperature superconductors (HTSC). The discovery of the $LaBa_2Cu_3O_7$ as a HTSC revolutionized the search for high temperature superconductors as it was the first time superconductivity had been realized in a non-metal system. The most common group of HTSC are the cuprate family of oxides, however there are also iron arsenides along with other intermetallic compounds that also can form superconductors. The structure of cuprate HTSC is extremely important as it is thought that the superconductivity comes from the 2-dimensional like CuO_2 channels that are formed[8–12]. Additionally the valence of the material also seems to be a valuable contributor, as superconductivity in these materials only appears at a narrow range of doping, and the oxygen stoichiometry is vital in determining the critical superconducting temperatures. The continued discoveries in HTSC, along with advances in cooling technology have the possibility of creating amazing zero loss conductors, in addition to high power electromagnets, and other unprecedented technologies.

1.1.4 Crystal Growth Techniques

Proper thin film growth techniques are essential for studying the properties of films. While there are numerous different methods of preparing thin films, each growth has its advantages and disadvantages, and different operating environments. Some of the important parameters of deposition include the operating temperature, pressure, and parent materials. Growth temperatures can vary based on the film growth, with higher temperatures providing energy to form crystalline materials, and lower temperatures being more likely to form amorphous or polycrystalline films. The base pressure of a system is the pressure in the chamber before the growth is initiated. Lower base pressure, or the pressure in the chamber before the growth is started, mean fewer contaminants during growth, and a higher purity of the deposited film. Growth pressure is a key parameter for all different growth techniques because of the mean free path - the average distance the gas phase particle travels between collisions, which is proportional to pressure with the following relation[45]:

$$\lambda = \frac{k_b \cdot T}{\sqrt{2} \cdot \pi \cdot p \cdot d_m^2}$$

in which λ = average distance between collisions, k_b = Boltzmann's constant, T = temperature in Kelvin, p = pressure, and d_m = molecular diameter. Some example temperature, pressure and corresponding mean free paths are listed in table 1.2. Parent materials include precursors in chemical deposition techniques and pure targets for physical deposition techniques. Selecting the growth technique for each material requires balancing these growth parameters, in addition to the material throughput and growth efficiency.

Table 1.2: Example mean free path calculations for various temperature and pressure ranges

Temperature (K)	Pressure (Torr)	Mean Free Path (m)
300	760	$1.023 \cdot 10^{-7}$
300	1	$0.777 \cdot 10^{-4}$
300	$1 \cdot 10^{-3}$	$0.777 \cdot 10^{-1}$
300	$1 \cdot 10^{-6}$	$0.777 \cdot 10^{2}$
600	760	$2.045 \cdot 10^{-7}$
600	1	$1.554 \cdot 10^{-4}$
600	$1 \cdot 10^{-3}$	$1.554 \cdot 10^{-1}$
600	$1 \cdot 10^{-6}$	$1.554 \cdot 10^{2}$
900	760	$3.068 \cdot 10^{-7}$
900	1	$2.331 \cdot 10^{-4}$
900	$1 \cdot 10^{-3}$	$2.331 \cdot 10^{-1}$
900	$1 \cdot 10^{-6}$	$2.331 \cdot 10^{2}$

Chemical Deposition Techniques

Chemical Vapor Deposition

Chemical vapor deposition (CVD) is chemical reaction based deposition technique in which precursor gases react with each other in a pressure chamber, combining to create the deposited materials. As the precursors react, they create the product material which precipitates out of the gas phase and forms the solid film on the substrate. CVD is a common method of commercial film deposition as it does not require extremely high vacuum, and it is not electrically intensive. It additionally can be used in fabricating a diverse range of materials and material quality[45].

Atomic Layer Deposition

Atomic layer deposition (ALD) is a type of chemical vapor deposition that allows for layer by layer growth using precursor gases that react to the surface of the substrate (or surface of the intermediate material). These reactions occur in such a way that only single layers are grown at a time, utilizing a self limiting procedure. Complete reaction of a precursor gas with the exposed area is known as an ALD cycle. In the

first cycle, the first precursor gas flows over the substrate and reacts, leaving a single layer of the material being grown. This first precursor gas is then flushed from the vacuum chamber, and the second precursor gas is injected. This second precursor gas reacts with the deposited first layer to give the second layer of the material, in a similar fashion to the first[45]. Process temperatures for ALD systems can range from moderate temperatures near (near room temperature) to hundreds of degrees Celsius. The operating pressures for these systems are relatively high, dependent on the precursor gas, and the reaction that takes place, however low base pressures are required to ensure the purity of the material growth. ALD growth is a good method for creating very thin, smooth, uniform films due to the self limiting layer growth, but the overall throughput for this type of growth is relatively low for the same reasons. Some materials commonly grown using ALD include oxides and nitrides, especially binary systems like Al_2O_3, HfO_2, TiN and TaN[46]. The two precursors for these example materials have one that includes the metal compounds reactant, and one that has the oxygen reactant (nitrogen reactant).

Physical Deposition

Physical deposition techniques are techniques that involve a mechanical process of knocking atoms or clusters from a target material and depositing onto a substrate material. These techniques generally require lower pressure than their chemical based counterparts as they typically do not use chemical reactions in the deposition process. While materials can be co-deposited using physical deposition techniques, the co-deposited materials do not interact with each other until they reach the substrate.

Evaporation

Evaporation is a high vacuum deposition technique in which the target material is heated to a vapor phase often by sublimation, but sometimes by vaporization. Heating methods commonly include resistive (joule) heating or e-beam heating as depicted in

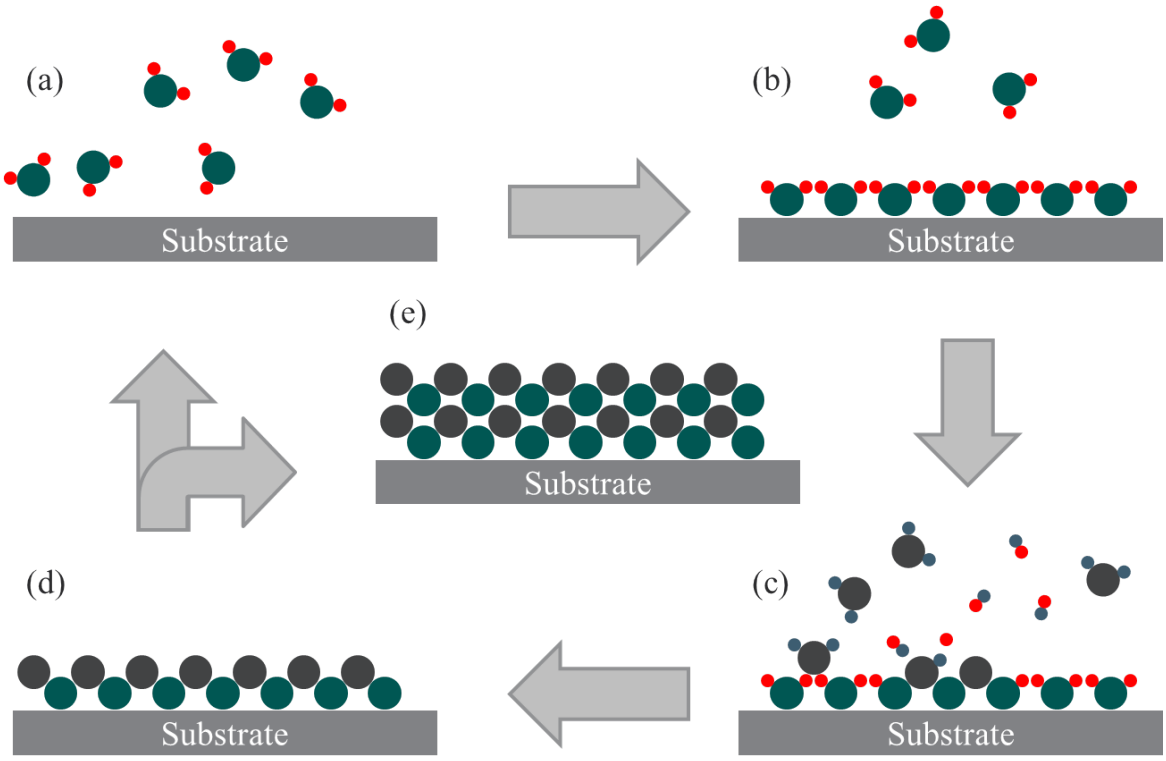

Figure 1.10: Schematic of atomic layer deposition cycles. (a) The first precursor gas is injected into the chamber. (b) Precursor gas interacts with the substrate forming the first layer and excess gas is pumped from the chamber. (c) The second precursor gas is injected into the system, reacting with the first layer forming the second layer. (d) Finished product at the end of an ALD cycle (e) Final film grown at the end of n cycles.

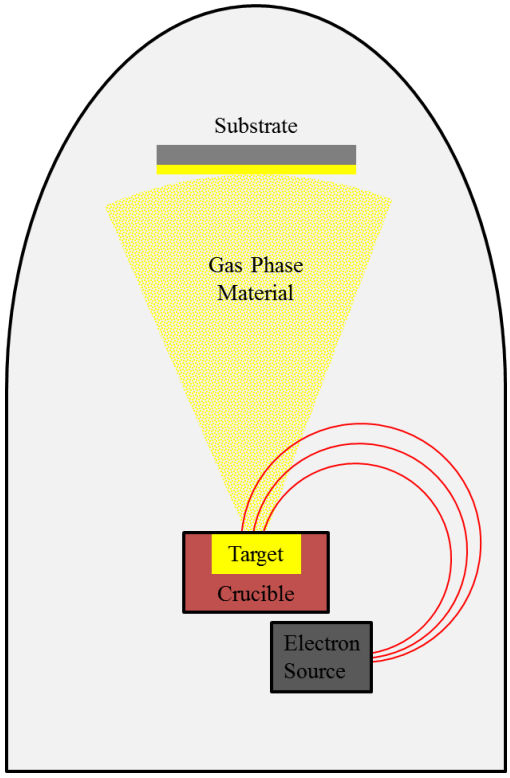

Figure 1.11: Schematic of electron beam evaporation system. Electron beam is bent through a magnetic field and rastered to heat the target, causing evaporation. Gas phase material travels in a line-of-sight path to the substrate.

figure 1.11[45]. The gas phase of the evaporated material then travels through the high vacuum system to the substrate where it condenses. The low operating pressures in evaporation systems lead to line of sight deposition – a property of evaporated film growth that can be utilized in lithographic patterning. Additionally, evaporation systems have the possibility of covering large areas at relatively fast growth rates[45]. All of these combine favorably, making evaporation one of the most common methods for industrial metal film deposition.

Molecular Beam Epitaxy

Molecular beam epitaxy (MBE) is a physical vapor deposition process that is similar to evaporation in that it uses a heating source to vaporize a target material which then travels and condenses on the substrate. Where MBE deviates from standard

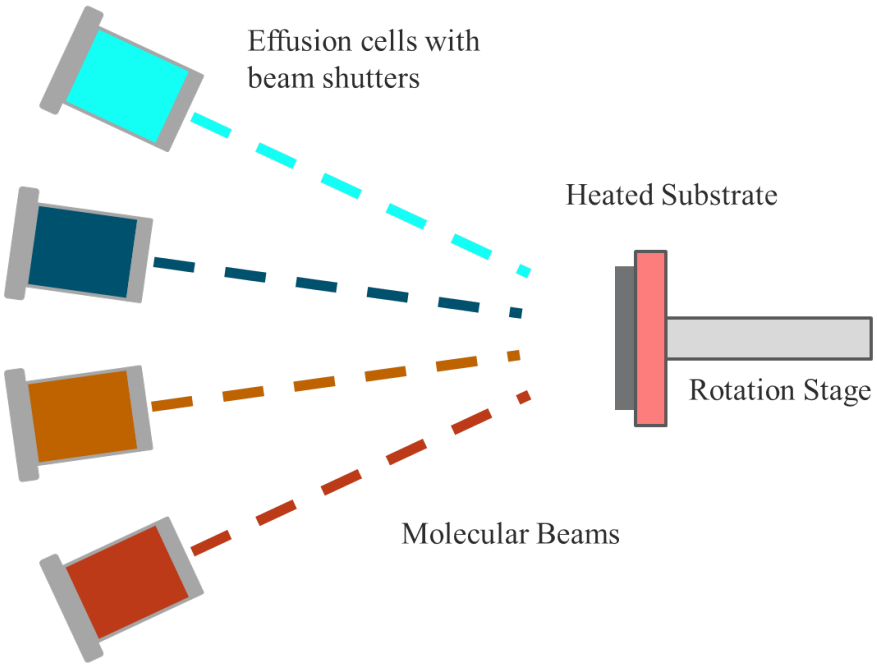

Figure 1.12: Schematic of a molecular beam epitaxy system. Knudsen effusion cells are heated vaporizing target material, creating a beam of target material. When shutters are opened, the molecular beam is directed toward and deposit on the substrate.

evaporation is that it requires ultra-high vacuum (10^{-10}torr), has much slower growth rates, and uses a heated substrate. These combine to provide the growth material sufficient energy, with an optimal flux of physical vapor to promote epitaxial single crystal growth. The target materials are heated either through Knudsen-effusion cells, or through electron beam heating[45].

Pulsed Laser Deposition

Pulsed laser deposition (PLD) can be considered a rapid evaporation process. In PLD a laser is pulsed onto a target, locally vaporizing the target, blasting small clusters of the target material into the chamber, and it condenses and grows on the substrate. PLD is a high vacuum process, and similar to MBE has a relatively slow growth rate, and uses a heated substrate. The energy from the heated substrate allows the material clusters to mobilize on the substrate surface and self-assemble into single

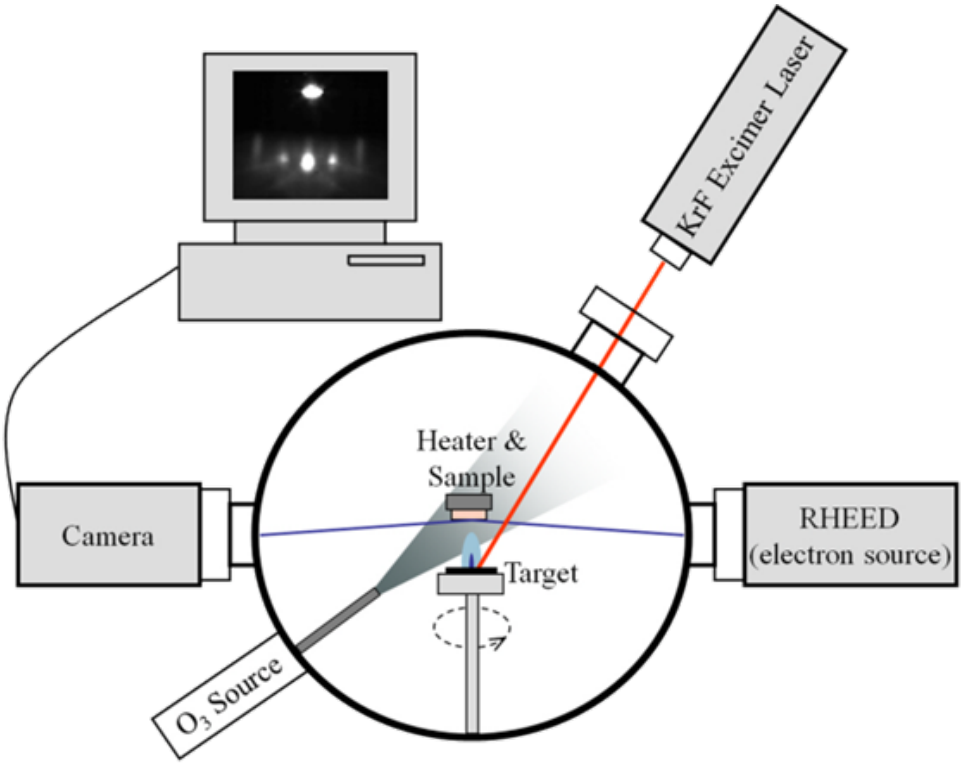

Figure 1.13: Schematic of a pulsed laser deposition system. Laser is pulsed on a target leading to target ablation. Ablated materials deposit and self-assemble on heated substrate. Crystal growth is monitored through RHEED pattern.

crystals. The rapid vaporization of the target causes it to maintain stoichiometric ratios, giving PLD one of its primary advantages over other growth techniques[45]. The phase of the target is important for getting the same phase in the final crystal growth, meaning the fabrication of PLD targets is important for the final product. Additionally this growth method is limited to materials that absorb the laser photons, and therefore is commonly used in insulator growth, as many metals reflect the laser light. PLD growth is commonly monitored by Reflective High Energy Electron Diffraction (RHEED) which can indicate growth mechanism and crystal quality *in situ*.

Sputtering is a versatile physical deposition technique in which a plasma is created near the target to be sputtered and the charged ions in the plasma bombard and

collide with the target, causing a billiards like mechanical knocking effect. The atoms or clusters that are knocked off then move through the vacuum chamber to the substrate where they collect and grow films. Sputtering is commonly conducted with argon gas – ionized into argon plasma – because Ar ions have a combination of a good atomic weight for causing knock-off inducing collisions, while also being a gas that ionizes with high efficiency into a plasma. The two methods of forming the plasma are direct current (DC) sputtering, and radio frequency (RF) sputtering. In DC sputtering a bias is applied across the gap between the housing and the target mounting, which ionizes the gas and accelerates the Ar^+ ions towards the target. RF sputteruing uses an applied radio frequency alternating current to ionize the gas species. The difference in mobility between the ions and the electrons create a self biasing which acclerates the ions toward the target[45]. A variation of these techniques is magnetron sputtering in which a ring of aligned magnets sits in the target holder, with an anti-aligned magnet sitting in the middle, creating a donut shaped magnetic field. This is used to lengthen the plasma lifetime, and create a more efficient plasma bombardment with the target. Sputtering targets can be conditioned with a pre-sputtering period changing the surface stoichiometry to a point where the sputtered film stoichiometry is the same as the bulk of the parent target[45]. Additionally, reactive sputtering is another variation in which a process gas such as oxygen is included in the sputtering chamber, and the sputtered material, for example: silicon, reacts with the process gas and forms a new sputtering product, which in this case would be SiO_2[45].

Growth Modes

Crystal growth modes are important for creating high quality samples. Crystalline materials begin growth in the form of nucleation where a small grain of a single crystal coalesces from clusters or amorphous phases of the material. Nucleation points become regions that promote crystal growth and the films grow out from those regions. Growth parameters such as growth rates, temperatures, critical geometries,

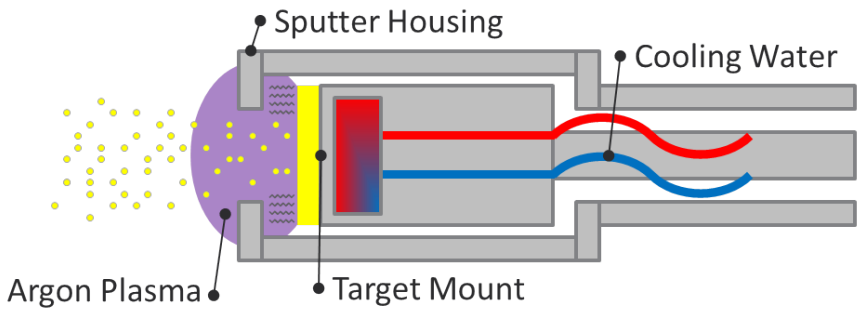

Figure 1.14: Cross sectional view of a sputtering gun. A DC or RF source is applied from the target mount to the outer housing, ionizing the gas, and causing ion impact

and surface energies[45]. Reflective high energy electron diffraction (RHEED) is a measurement technique that can monitor *in situ* the film growth, and is useful in determining the growth modes. High energy electrons are diffracted off the surface of the sample, collected on a RHEED screen and the intensities are monitored during growth. Typical patterns include a primary reflection, and three diffracted spots. The quality and shape of these diffracted spots inform the user of the growth modes and growth rates as full unit cells have higher intensities, and streaky spots indicate island growths.

Island growth is a growth mechanism that arises from multiple nucleation points on the surface which grow in 3 dimensions. This is due to the bonding between deposited atoms is stronger than the bonding of the deposited atoms to the substrate. The islands grow, and eventually connect making thin films[45].

Layer by layer growth occurs when the deposited films grow primarily in two dimensions across the surface of the substrate, or previously grown film layer. These layers grow on top of each other with bonding energies trending towards bulk values[45].

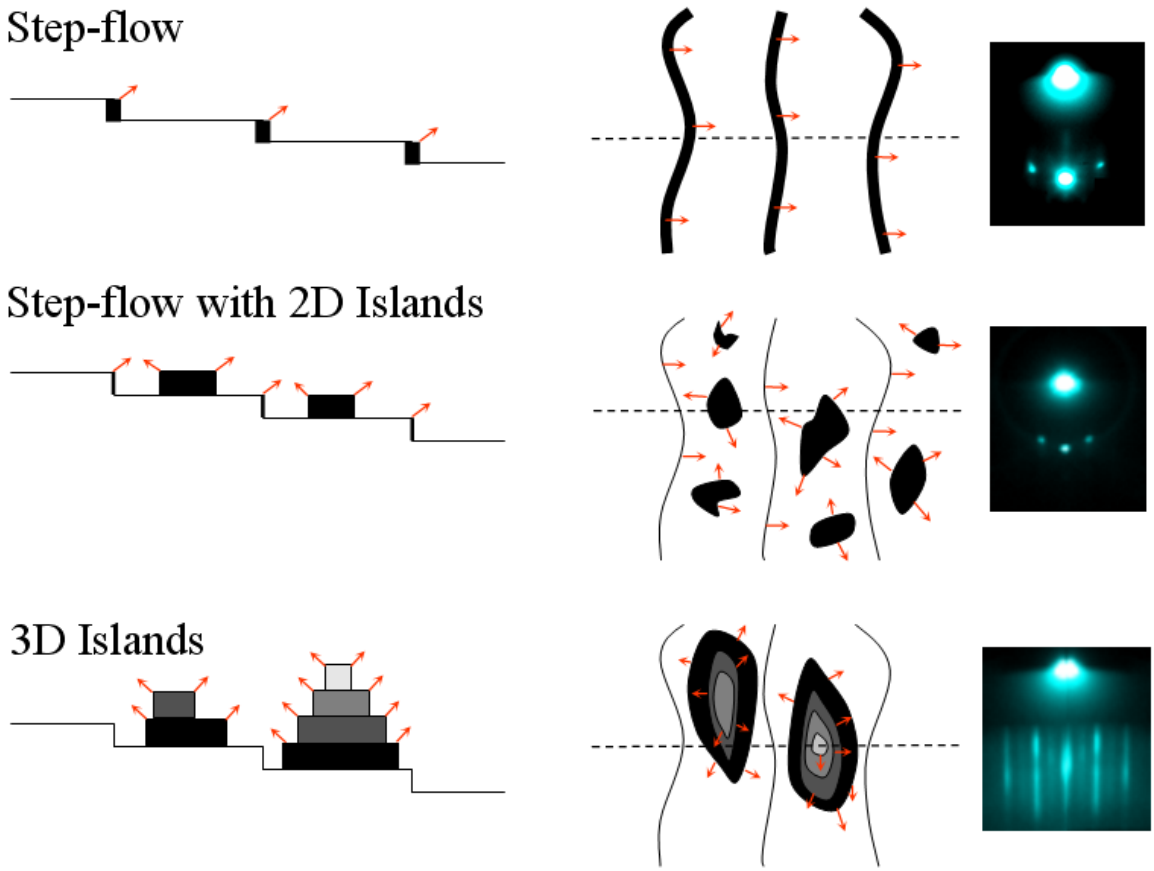

Figure 1.15: "Examples of 3 growth modes and their RHEED signatures. Left column shows side view taken at dotted line in middle column. Red arrows indicate direction of growth. Right column shows typical RHEED images for each growth mode." from [48]

Step flow growth commonly occurs when the substrate has miscut terraces or step edges. These edges create surface energy regions that promote growth. The atoms fill in the corners of the step edges and the film growth flows in the free direction[47].

Mixed growth is the method by which most real systems are created. While in some ideal systems on of the methods stated above will occur, often there are combinations of multiple growth mechanisms. For example islands can initially nucleate, and create the step edges needed for step flow growth. Step-flow, step-flow plus island, and 3D island growth modes are depicted in figure 1.15 along with their characteristic RHEED patterns.

1.1.5 Device Fabrication

Despite the importance of crystal growth, very few - if any - devices and samples are a single film growth. Fabricating devices provides an ability to create multiple test samples from a single as-grown film which is vital in conducting comparative studies, fabricate multiple levels of film growth on the same substrate, and pattern these films into useful interconnected designs. The patterning of these films uses a process called lithography, which is a form of masking regions of the sample for deposition or etching processes[45]. Optical lithography is a process that uses near ultraviolet (UV) light to fabricate relatively large features > 800nm , while smaller features $> 10'$sofnm are created using extreme UV or electron beam lithography. The feature size, and consequently the type of lithography used, is governed by the critical dimension - wavelength of light relationship.

$$CD = \kappa_1 \cdot \frac{\lambda}{NA}$$

in which CD is the critical dimension, κ_1 is a coefficient related to the processing setup, λ is the wavelength of light, and NA is the numerical aperture of the optics, which is dominated by the depth of focus.

Photoresists are polymeric materials that have a sensitivity to light, which causes them to change their mechanical properties. Positive resists are those that "soften" when exposed to the lithographic light, and the exposed areas are washed away in a developing solution. A negative resist is one that when exposed to the lithographic light, the polymeric resist cross links and hardens, making it less susceptible to the developing solution. Due to the diffraction of light at the surface of the resist and absorbtion through the thickenss of the resist, the side walls on the resist (the area separating the exposed, and unexposed areas) typically have some amount of slope depicted in figure 1.17. The positive slope achieved in positive masking techniques make it useful for etching, while the negative slope associated with negative masking makes it more advantageous for liftoff[49].

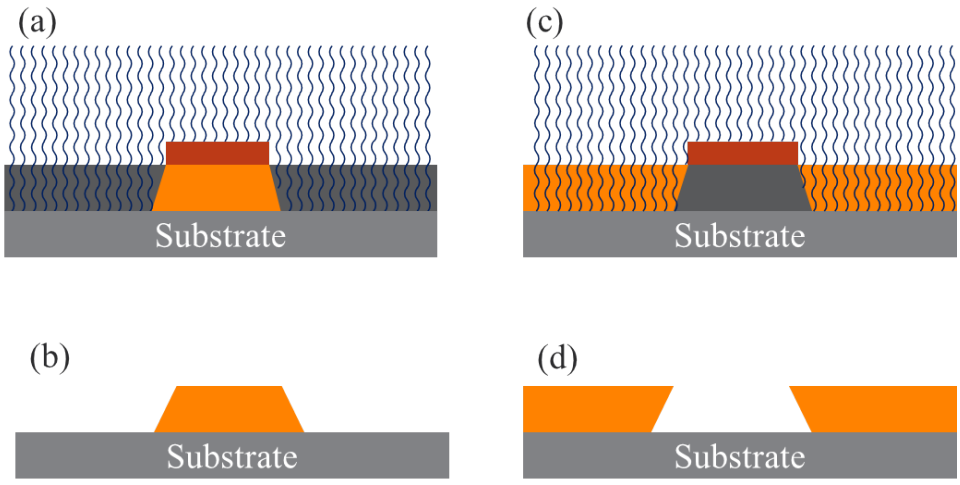

Figure 1.16: Schematic of photoresist processes. (a) Positive photoresist is exposed, softening the exposed areas. (b) Softened areas are developed away leaving the resist covered by the masked region. (c) Negative photoresist is exposed, cross-linking and hardening the exposed areas. (d) Unexposed regions are developed away, leaving the exposed areas.

Etching is a process in which through chemical or physical means, portions of the deposited film are removed and come in the form of wet and dry etches. The most important property of any etch is the etch selectivity, a measure of how sensitive a material is to the etching environment compared to the other materials in that environment ie. photoresists or substrates[45]. Wet etches generally include acid or base reactions with the film in order to dissolve the exposed areas of the film, whereas dry etches come as either a purely physical process involving plasma ions, similar to sputtering, or a reactive ion etching which combines the physical etching process with a chemical reaction that takes place in the plasma to increase etching rates, or etching selectivity. In either case, photoresist layers are used to mask and protect the portion of the film that are intended to remain on the substrate or device[45].

Liftoff conversely is a method of depositing films on top of exposed and developed photoresists. Areas where the photoresist is developed away open areas in the photoresist layer that allow for film deposition onto the substrate, or underlying layers, while the areas still covered by the photoresist have the film deposited on top

of the photoresist. After the film is deposited, the devices are placed in a solution that dissolves the remainder of the photoresist, causing the film deposited on top of the photoresist regions to *lift off* and only the films deposited directly on the underlying layers remain. Combining the deposition techniques discussed above with lithographic patterning (in addition to countless other advanced processing techniques) provides the ability to create incredibly complex multi-level devices on which the modern semiconductor industry is based[50].

1.2 Characterization Techniques

Creating and fabricating thin films and complex devices is instrumental in modern electronics, however these films and devices need to be characterized and interrogated to determine their properties, and quality. There are seemingly infinite methods of material characterization, especially considering the specialization of so many of the characterization techniques, however this section will focus on structural, electrical and magnetic characterization techniques for thin films and devices[45].

1.2.1 Structural Characterization

Bulk and surface structures of crystal systems are valuable information for studying complex oxide crystal systems. These data help determine the material phase, possible impurity phases, strain states, lattice constants, and growth quality, all of which give insight as to the other properties that exist within the material.

X-Ray Diffraction

X-ray diffraction (XRD) is a non-destructive method of probing the material structure in which x-ray radiation is directed towards the probed material, and the reflections of the x-rays are counted in an x-ray collector. The x-ray reflections are counted in

the collector when the conditions for Bragg's law are satisfied

$$n\lambda = 2dsin\theta$$

where n is an integer, λ is the wavelength of the x-ray radiation, d is the separation between the planes reflecting the x-ray radiation, and θ is the angle of incidence of the x-ray radiation. d is related to the crystal structure of the film such that

$$d = \sqrt{\frac{a^2}{h^2} + \frac{b^2}{k^2} + \frac{c^2}{l^2}}$$

where a, b, and c are the lattice constants for the crystal, and h, k, and l are the Miller indices of the Bragg plane which are used to identifiy specific directions and planes within a crystal structure[45].

XRD can show the crystal phases in single crystal, powder, and poly-crystalline samples using a $\theta - 2\theta$ scan, crystal quality by using an ω rocking curve while focused on a crystal peak, and epitaxial coherence between films and substrates by creating a reciprocal space map – done by measuring multiple $\theta - 2\theta$ scans while also varying the ω value. In these measurements, θ is the angle between the deflected beam and the surface of the sample, while ω is the angle between the incident beam and the surface of the sample. The sum of θ and ω is 2θ because in thin film measurements, these two values are often the same. Additionally x-ray reflectivity (XRR) is a $\theta - 2\theta$ scan aligned around the primary reflection of the incident beam at low angles (0.5°) that can measure the thickness of films, as long as the films have flat surfaces and flat interfaces. Using all of these measurements around different, indicative peaks can provide valuable information as to the crystal structure, and quality, all without damaging the crystal[45].

Scanning Probe Microscopy

Scanning Probe Microscopy (SPM) is a family of measurements that use an atomically sharp probe tip on the end of a cantilever in contact or close proximity to the surface of the film to measure the surface characteristics. A laser is focused on the end of the cantilever, and reflected towards a photo detector lens. The photo detector picks up deflections in the cantilever with resolutions down to nm or smaller length scale changes as it interacts with the surface of the film.

Atomic Force Microscopy

Atomic force microscopy (AFM) uses an atomically sharp tip to measure the surface topography. The tip is oscillated at a resonant frequency and tapped across the surface of the sample in tapping mode, or the tip is put in contact with the film and dragged across in contact mode. The cantilever deflects as the tip moves up and down with respect to the sample topography. A photo diode detects the deflection of the the cantilever and converts that signal into an amplitude in tapping mode or a voltage in contact mode. The resulting scan is grafted together into a topographic map of the film[45].

Piezo Force Microscopy

Piezoresponse force microscopy (PFM) is a technique that uses a conducting tip that is connected into a function generator, and operated in contact mode. The function generator is used to create an alternating current that drives a resonant shape deformation in a piezo-electric or ferroelectric material. With the use of a lock-in amplifier, changes in the phase with respect to the driven resonant frequency are imaged as in-phase or out-of-phase, which is used in measuring domains in ferroelectric materials. Another function of PFM is that when a sufficiently high bias is applied to the tip as it contacts the surface, it can cause distortion in ferroelectric material due to the converse piezo-electric effect, or write domains in a specific direction[51].

Electron Microscopy

Electron microscopy is a power tool for imaging materials, sometimes down to the atomic scale. Electron microscopy uses electrons accelerated to high energies and focused on the sample. These high energy electrons interact with the sample, some reflected from the sample as secondary and back-scattered electrons, some exciting the electrons in the system and causing them to emit electrons and/or x-rays as Auger electrons and energy dispersive x-rays, and some transmitted, diffracted and scattered from the crystal both elastically and inelastically as transmission electrons, diffracted electrons, and energy loss electrons, respectively. All of these different interactions reveal different information about the examined material[45].

Secondary Electrons (SE) are electrons that are emitted from the outer levels of the surface and near surface of the samples. These electrons are collected and used to image the surface topography of the sample.

Back Scattered Electrons (BSE) react with the atoms of the sample, and are scattered back toward the primary beam. These electrons help to evaluate the chemical composition as the BSE are sensitive to heavier nuclei providing a Z contrast.

Auger Electrons (AE) are core level electrons that are emitted from the atoms at the surface of the sample, which is accompanied by an outer level electron falling into the vacancy left by the emitted electron. This electron transition releases a characteristic energy in the form of an x-ray for each element, providing surface composition information.

Energy Dispersive X-Rays (EDX) is a similar mechanism as Auger electron spectroscopy in that outer level electrons fill in vacancies left by the emitted core shell electrons, and release a characteristic x-ray. The major difference is that EDX spectroscopy interrogates the bulk of the sample, instead of the surface.

Transmission Electrons are the work horse of transmission electron microscopy with provide for the cross section imaging of thin prepared samples. Advances in transmission imaging have allowed for directly imaging atomic resolution of samples. These cross sectional images are used to look at thin film interfaces, and crystal structures on the atomic level.

Elastic Scattered Electrons create diffraction patterns as they diffract off of the crystal lattice, and are used for diffraction related structural analysis of TEM samples. These diffraction patterns, similar to XRD appear when the Bragg conditions are satisfied, providing crystallographic information.

Inelastic Scattered Electrons are used in Electron Energy Loss Spectroscopy in which transmission electrons are diffracted through the sample, and scattered inelastically, meaning they lose energy as they are scattered. The energy spectrum profile of these electrons can be used in determining chemical composition, valence states, and chemical bonding among other things. This is similar to the other spectroscopic microscopy techniques, but can be more difficult to use.

1.2.2 Electronic Characterization

Electrical characterization comes in many forms and characterizes the various electrical phenomena exhibited by materials. Most electrical measurements are conducted by applying and measuring currents and voltages in various orientations probing different properties.

Resistivity Measurements

Resistivity measurements are a method of measuring the absolute resistance of materials with the geometry of the material taken into consideration. Different arrangements of electrical connections measure different sample resistivities.

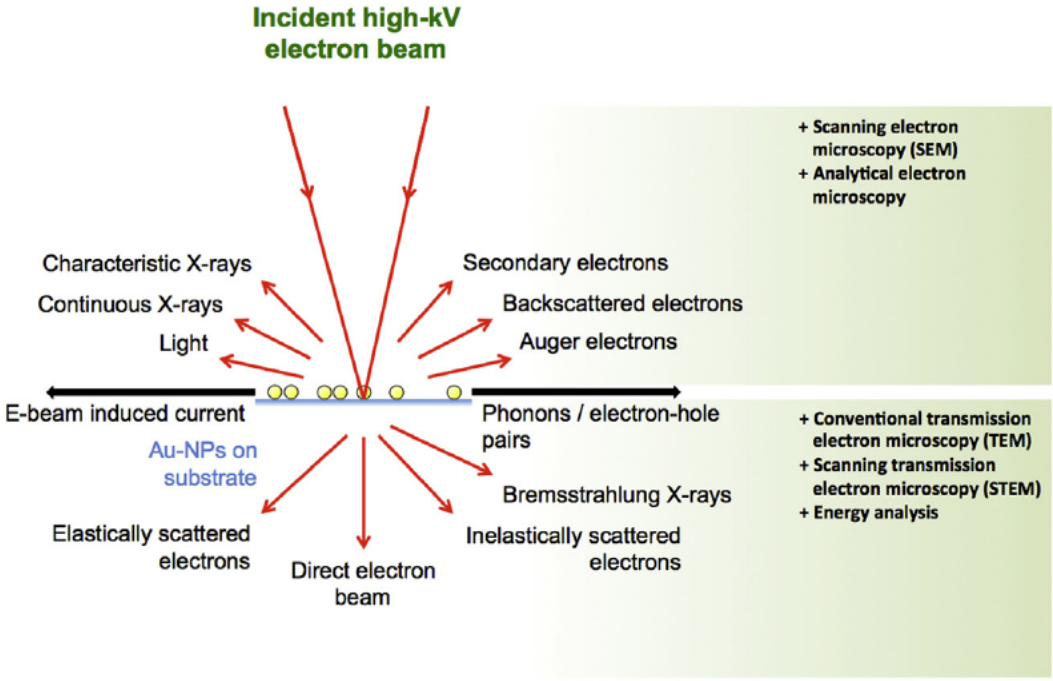

Figure 1.17: Diagram of the various scattering and characterization techniques from electron microscopy, including both scanning electron microscopy, and transmission electron microscopy from [52]

4-Wire Linear measurements have four contacts aligned in a linear arrangement where the outside two wires have current applied between them, and the inside two wires measure the voltage drop across the sample shown in figure 1.18(a). The purpose of the 4-wire measurement is to eliminate the contact resistance that is created when wires are connected to samples, meaning 4-wire measurements are mostly used when measuring metals where the overall resistance can be dominated by the contact resistance. These measurements follow Ohm's law:

$$R = \frac{V}{I}$$

where R is the resistance, V is the voltage drop across the wires, and I is the current. Resistance is an absolute value relating the current and the voltage of the sample, however when the geometry of the sample is considered, we can reduce resistance into

resistivity using the general equation:

$$\rho = \frac{R \cdot A}{l}$$

where A is the cross sectional area (the width times the thickness) of the material between the voltage leads, and l being the distance between the the voltage leads, and are commonly give in the units $\Omega \cdot$ m[53].

Van Der Pauw measurements are a variation of a 4 probe electrical measurement, in which a square sample has two current leads on adjacent corners, opposite two voltage leads on the other adjacent corners. There are four x axis measurement orientations, and four y axis measurement orientations, using the notation in figure 1.18(b), the averages between the four orientations for each direction provide the average resistance for those directions.

$$R_x = \frac{R_{12,34} + R_{21,43} + R_{34,12} + R_{43,21}}{4}$$

$$R_y = \frac{R_{13,24} + R_{31,42} + R_{24,13} + R_{42,31}}{4}$$

Where

$$R_{12,34} = \frac{V_{34}}{I_{12}}$$

In most materials, averaging these two directions together give the resistance of the sample, which can be used to calculate the resistivity. In some cases, anisotropies exist between the two directions in which the R_x will be different than R_y[54].

Two-probe linear resistance measurements are measurements where the voltage drop is measured between the same electrodes as the current is sourced. These measurements are commonly conducted among insulating samples where the sample's resistance will dominate the total resistance, and therefore the contact resistance will be negligible in comparison.

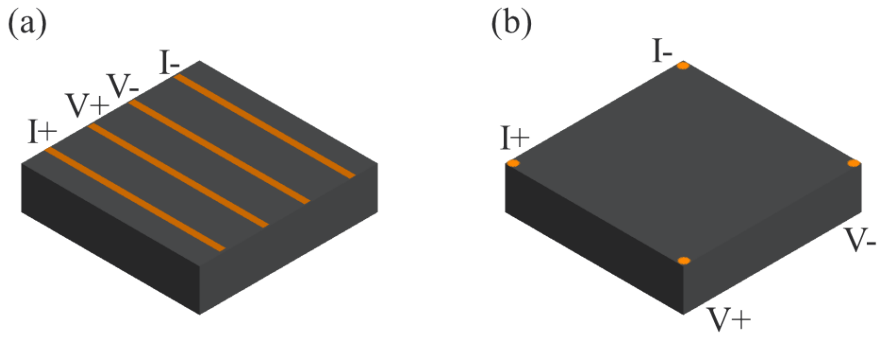

Figure 1.18: Schematics of 4-wire measurements (a) 4-wire linear alignment (b) 4-wire Van Der Pauw alignment.

Hall Measurements

Hall measurements are a specialized resistance measurement in which the voltage leads are placed on an axis transverse as compared to the current leads. In ideal measurements, the transverse voltage electrodes detect a voltage drop when in the presence of a magnetic field, due to the Lorentz force which states that an electron with a velocity within a magnetic field will experiences a force at a right angle such that

$$\mathbf{F} = q(\mathbf{E} + \mathbf{v} \times \mathbf{B})$$

These magnetic fields can come from externally applied fields leading to standard hall measurement, or from internal magnetic fields in the case of anomalous hall measurements and spin hall measurements.

Capacitance Measurements

Capacitance is a measure of a materials ability to store charge. These materials are non-metal dielectrics that are described by their dielectric constant. Measuring the capacitance of materials is done using an LCR meter which probes the inductance, capacitance and resistance. Alternating currents (AC) are applied across the probed capacitor, and the the capacitance is extracted using internal circuitry.

Capacitance measurements are typically measured with respect to varying voltages (C-V measurement) and with respect to AC frequencies (C-f).

Ferroelectric Measurements

Ferroelectrics are a very specific set of materials, and therefore have a specific set of measurements that are used to evaluate them. These measurements include primarily polarization loops, pulse measurements and fatigue measurements.

Polarization measurements (P-E) are measured with respect to electric field. The polarization of a sample is the asymmetric charge accumulation at the surface, and these measurements are conducted by applying voltages in a set waveform and frequency across the ferroelectric material. The polarization change is indicated by a switching current, which is integrated with respect to time to get a charge, and then geometrically normalized to receive the final output in C/cm^2. This is plotted against the electric field, which is obtained by normalizing the voltage to the thickness of the film[55].

Positive Up Negative Down (PUND) measurements are a variation of polarization measurements. The user defines a pulse train for the I-V measurement, allowing for determination of the different I-V components. When the film is first switched to a new orientation, the current is a combination of leakage current components and the switching current. If the next pulse is done in the same direction, only the leakage current components are at play, provided the film has completely switched. and example pulse train is given in figure 1.19[55].

Fatigue is a vital part of ferroelectric integration into devices. Ferroelectrics used as switches are susceptible to switching related breakdown, usually from shorts developed from crystal deformation as the polarization switching occurs. Fatigue measurements are a method of determining the lifetime of the ferroelectric materials.

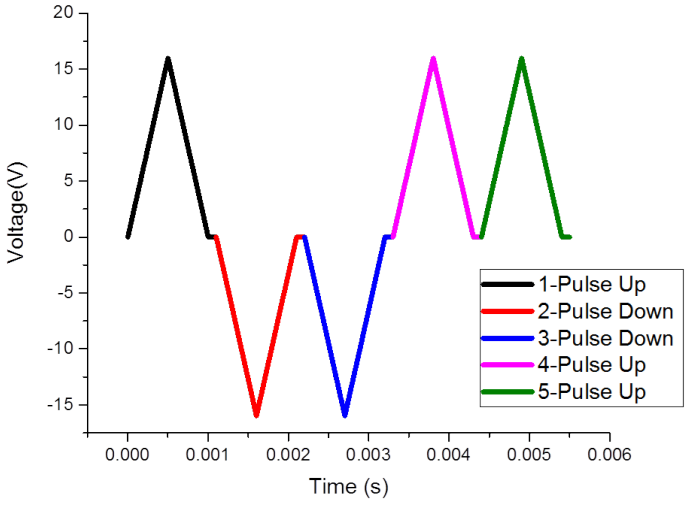

Figure 1.19: Ferroelectric PUND Pulse Train

The ferroelectric is switched at a user defined frequency and voltage, and the polarization is recorded with respect to the number of switching cycles. This number is often in the millions to billions of switches for typical measurements[55].

1.2.3 Magnetic Characterization

Magnetic characterization probes the magnetic moments of the samples, which can be global magnetic moments, magnetic domains, or individual magnetic moments.

SQUID Magnetometry

Superconducting Quantum Interference Device (SQUID) magnetometry is a method of measuring the global magnetization of a sample. The device is made up of two parallel Josephson junctions in a superconducting loop. The sample is mounted inside the superconducting loop, and the magnetic field of the sample interferes with the current going through the two Josephson junctions which then outputs a signal proportional to the magnetic field of the sample. SQUID are very sensitive and can detect small magnetic moments, such as canting of antiferromagnets[56].

Magneto-Optic Kerr Effect

Magneto-Optic Kerr Effect (MOKE) instruments take advantage of the way light interacts with magnetic surfaces. When light is reflected off of a magnetic surface, the light can experience a change in its polarization and intensity. Polarized light is reflected from the surface of the magnetic materials, and the corresponding beam can be analyzed, both in polarization and intensity to directly image the magnetic domains and orientations of the surface of the material[57].

1.2.4 Polarized Neutron Reflectivity

Polarized neutron reflectivity (PNR) is an advanced scattering technique using polarized neutrons to measure the layer by layer magnetization of a sample. Neutrons are ideal for this function as they are electrically neutral, making them unaffected by electrostatic interactions in the crystal. Instead the polarized neutron has a weak magnetic moment that interacts with the magnetism of the sample. The magnetic interactions between the sample and the neutrons cause them to scatter at different angles. These deflections are detected and used to determine the absolute value of the magnetic moment at layers in samples, which is useful in determining interfacial exchange coupling between thin films[58].

1.3 Ionic Liquids

These electrolytes can be simply defined as liquid salts, for example melted salts and oxides. While this definition holds for many different materials, the functionality is limited when the ionic materials have high melt temperatures, therefore we more closely explore the category of room temperature ionic liquids. Room temperature ionic liquids (IL) are typically organic, or organo-metallic salts with melting temperatures below 100°C and usually much lower than that[59–61]. IL were first discovered in the early 20^{th} century, and advanced slowly until the 1980s when their

exploration, characterization, and application took off[59, 62]. IL have recently found uses in wide ranges of applications ranging everywhere from new solvents for chemical reactions like electro-plating, energy materials like liquid based battery electrolytes and supercapacitors, and many bio-sciences applications due to their compatibility with polar and non-polar materials, and non-toxic properties[59, 62]. Another reason for the uptick in research interest in IL is the electric double layer formation when the liquid is in contact with electrically charged surfaces, making liquid interfaces with electronic materials an area of particular interest[60, 61]. The diversity of IL solid interactions are immense as there are at least 10^{16} possible anion/cation combinations, including anions and cations with multiple charge centers, and magnetic ions[59].

1.3.1 Properties

There are a wide variety of properties that make IL useful for applying to the surfaces of electronic materials. The first is the low melting temperatures that are achievable for these materials. Many melting temperatures are at or below room temperature. These melting temperatures compare to the hundreds of degrees C for many ionic compounds and most likely occur because of the large asymmetric cations that prevent the ionic crystallization down to very low temperatures[59]. However, the size of alkyl chain molecules on the ions does not have a monotonic effect on the melting temperature, making it difficult to predict the melting temperatures of new IL[59].

IL viscosity is greater than those for other organic solvents, like alcohol, which is disadvantageous when considering their use as solvents, however the viscosity is sufficiently low when using the IL as an electronic interface with solid materials. Keeping IL viscosity low will be important for future studies as the viscosity can affect the capacitative and electrochemical properties of the liquid[63, 64]. These liquids also have a negligible vapor pressure, making them compatible with low pressure and vacuum chambers while remaining in a liquid form [59, 62, 63]

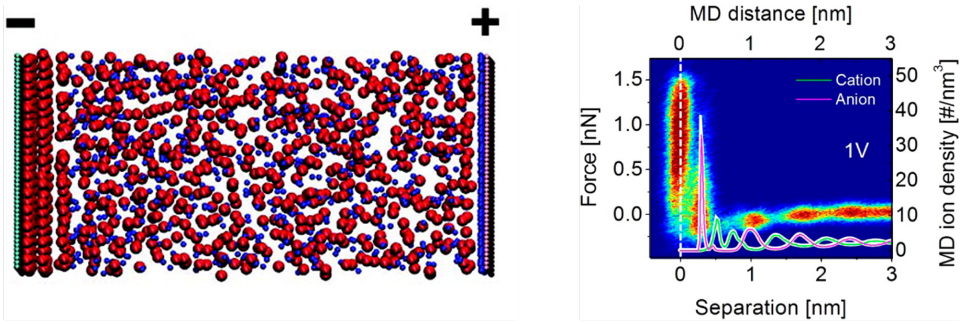

(a) (b)

Figure 1.20: (a) Simulated model of electric double formation from [61] (b) Histogram of force-distance AFM curves showing electric double layer formation, matched with molecular dynamics modeling from [69]

Perhaps the most important property for electronic solid interfaces exhibited by IL is the formation of an electric double layer capacitor. There have been numerous studies looking at the kinetics and dynamics of the electric double layer, however there is still debate as to the behavior of these formations[60–63]. What is certain is that the ions within the liquid separate to charged (or consequently grounded) surfaces. The accumulation of ions at the surfaces impart an ion based charge which can reach densities as high as 8×10^{14} charges per cm^2, orders of magnitude higher than conventional solid state capacitors[65–67]. These extreme interfacial voltage drops occur because the like charged ions stack up against the charged surface, and alternating layers of ions and counter ions form however the ion ordering dissipates as it moves into the bulk of the liquid. The opposite ordering appears against the oppositely charged surface shown in figure 1.20 (a)[60, 61, 68]. These double layer structures have amazingly been observed using atomic force microscopy in figure 1.20 (b), and confirm that the thickness of the liquid is of negligible importance in forming the electric double layers[69].

1.3.2 Solid Interface Applications

Thus far ILs have found many scientific applications that utilize the electric double layer formation and provide spectacular control over phenomenological properties.

Electrostatic charges have been shown to create superconductivity in $SrTiO_3$ and $KTaO_3$, used to gate ambipolar WS_2, and improve conductivity in MoS_2[66, 70–72]. Modifying the stoichiometry in oxides has produced results such as induced metal insulator transitions in VO_2, metalization of transparent conducting WO_3, and transistor activation in amorphous-InGaZnO [73–75]. More strenuous electrochemical effects include the intercalation of lithium ions into layered materials like graphite and transition metal dichalcogenides, electroplating of steel, electrodeposition of CdS, and stabilizing SiO_2 nanoparticles [76–80]. The versatility of ionic liquid-solid interactions makes combining them a powerful tool for interrogating the electrostatic and electrochemical phenomena of complex materials.

Chapter 2

Impact of Gate Geometry on Ionic Liquid Gated Ionotronic Systems

2.1 Preface

A version of this chapter was originally published by A.T. Wong[*1,2], JH Noh[*1,3], P.R. Pudasaini[1,3], B. Wolf[1,3], N. Wisinger[3], A. Herklotz[2], Y. Sharma[2], A.V. Haglund[1], S. Dai[4], D.Mandrus[1], P.D. Rack[#1,3], T.Z. Ward[#2] for an Ionotronics special issue of Applied Physics Letters: Materials (APL Materials) [81]

2.1.1 Author Affiliations

[1] Materials Science and Engineering Department, University of Tennessee, Knoxville, 37996, TN USA

[2] Materials Science and Technology Division, Oak Ridge National Laboratory, 1 Bethel Valley Rd., 37839, Oak Ridge, TN, USA

[3] Center for Nanophase Materials Science, Oak Ridge National Laboratory, 1 Bethel Valley Rd., 37839, Oak Ridge, TN, USA

[4] Chemical Science Division, Oak Ridge National Laboratory, 1 Bethel Valley Rd., 37839, Oak Ridge, TN, USA

[*] Equal Contribution First Author

[#] Co-Corresponding Authors: Email prack@utk.edu, wardtz@ornl.gov

2.1.2 Acknowledgements

PDR and BW acknowledges support for the a-IGZO thin film transistor device was supported by NSF CPS #1544686. JHN acknowledges support by the U.S. Department of Energy (DOE) under Grant No. DOE DE-SC0002136. AVH acknowledges support from the UT JDRD program. ATW, AH, YS, and TZW

acknowledges support by Laboratory Directed Research and Development Program of Oak Ridge National Laboratory, managed by UT-Battelle, LLC, for the U.S. Department of Energy. Some measurements were conducted at the Center for Nanophase Materials Sciences, which is a DOE Office of Science User Facility.

2.1.3 Contributions of Authors

Dr. J.H. Noh is responsible and thanked for the device design, and in working with Dr. P.R. Pudasaini in device fabrication. Dr. J.H. Noh wrote the labview programs used to measure the transport measurements, while I made edits for troubleshooting purposes when necessary. Dr. Noh, Dr. Pudasaini, B. Wolf and I all conducted transport measurements at different times during the study. Dr. T.Z. Ward advised the instrumentation and transport measurements, while Dr. P.D. Rack advised the design and fabrication of these devices.

2.2 Published Version of "Impact of Gate Geometry on Ionic Liquid Gated Ionotronic Systems"

2.2.1 Abstract

Ionic liquid electrolytes are gaining widespread application as a gate dielectric used to control ion transport in functional materials. This letter systematically examines the important influence that device geometry in standard side gate 3-terminal geometries plays in device performance of a well-known oxygen ion conductor. We show that the most influential component of device design is the ratio between the area of the gate electrode and the active channel, while the spacing between these components and their individual shapes have a negligible contribution. These findings provide much needed guidance in device design intended for ionotronic gating with ionic liquids.

2.2.2 Impact of Gate Geometry on Ionic Liquid Gated Ionotronic Systems

Ionic liquids (IL) have garnered recent attention for their unique ability to manipulate and control properties of functional materials through ionic conduction[70, 73, 74, 82–86]. By interfacing IL electrolytes with solids, the IL can function as an electronic gating medium, operating in ways that are not possible in conventional electronic devices due to the exceptionally large electric potential applied at the solid-liquid interface during gating. Ionic control of materials through IL gating has been used to intercalate small ions such as lithium or sodium into layered materials or control oxygen stoichiometry, which can be used to enhance carrier mobility, modify electric screening lengths, tune optical transmission, and increase superconducting critical temperatures [66, 72, 85, 87–89]. One particularly exciting series of results includes

the widespread manipulation of ion mobility and functionalization of oxide materials due to the effect of electrostatic and/or electrochemical phenomena that occur at IL-solid oxide interfaces [74, 82]. Even with the vast spectrum of property control, all of these experiments have a few common features: (i) a gate electrode that applies the bias to the IL, (ii) an active material to which the IL is applied, and (iii) an electrical ground reference, which is often connected to the active material. Beyond these similarities, the way these features are arranged in a test device can vary dramatically. The gate-electrode geometry in these devices can range from relatively crude systems, such as dangling a coil of wire in a bath of IL, to floating a gold foil on the IL, to polymerized forms of IL attached like a membrane, to lithographically patterned electrodes in various coplanar and non-coplanar geometries, to independent electrodes mounted on a sample tray[75, 76, 83, 88, 90–93].

Despite the many materials explored and experiments conducted utilizing liquid electrolyte gating in electronic and ionotronic devices, there have been few studies that examine the optimization of the devices themselves[94]. One of the specific properties that needs to be explored is the relationship between the sizes and geometries of the gate electrodes and the active device channel. A common design for these IL devices utilizes a coplanar "side gate" geometry meaning the gate electrode is offset from the active channel of the device and on the same fabrication level so the IL can be applied as a droplet that covers the gate electrode and the active channel[70, 72–74, 82, 84–86, 89]. The ions in the liquid segregate under an applied bias in a way that gives a layer of ions electrostatically attracted to the electrode, forming the bias-dependent electric double layer which can be exploited to generate extremely large short-range interfacial charges [61, 68, 69, 95]. Many of these devices have operated under a rule of thumb that the ratio of the gate electrode area to the device channel area should be maximized within the geometric constraints of the sample. However, while absolutely critical to understanding and predicting device performance, a methodical study of the effects of gate-electrode size and orientation to channel on physical transport in IL-gated devices is lacking. In this letter, we systematically explore an approach to

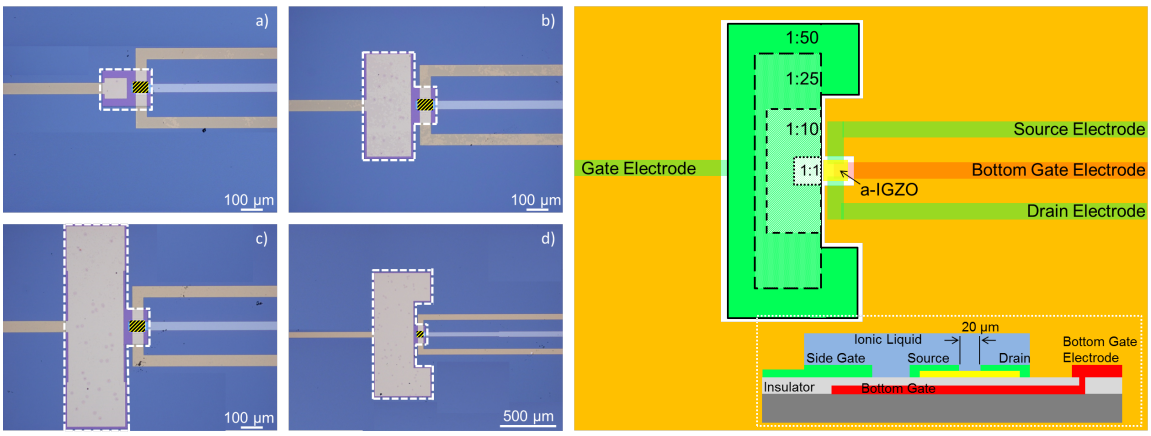

Figure 2.1: Optical micrographs and schematics of the rectangular design devices. The active channel is displayed as the striped yellow and black region, while the area exposed by the photoresist that is in contact with the IL is outlined by the dotted line. Micrographs show active channel to gate area ratios of a) 1:1, b) 1:10, c) 1:25, d) 1:50. e) A schematic showing the relative sizes of each gate electrode overlaid and the photoresist later covering the non-active parts, with the inset showing the cross sectional view of the device.

quantitatively describe the effect of the gate electrode size on the efficiency of side gated devices.

Amorphous indium gallium zinc oxide (a-IGZO) is known to be an effective liquid electrolyte transistor, demonstrating a modified electronic conduction behavior based on its oxygen stoichiometry [73, 86]. In this study, a-IGZO was selected as the active material system to examine the gate-geometry effect and was sputtered and lithographically patterned into the active channel. The devices were designed with the area of the active channel held constant at 1000 μm^2 (50 μm x 20 μm) while the area of the gate electrode was varied to get active channel to gate area ratios of 1:1, 1:10, 1:25 and 1:50. A layer of photo resist was spin coated on the device and a window was exposed in order to uncover the active areas of the device, specifically the side gate electrode and the active a-IGZO channel, while isolating the gold patterns that lead to the electric contact pads. This is done to precisely control the ratio between the active material in the device and the top gate electrode while minimizing any effects from the patterned leads that could cause a self-biasing. The samples were fabricated

to match the work of *Pudasaini et al.* and an aerial schematic of the devices with optical micrographs are seen in figure 2.1[73, 86]. The 0.3 μL droplet of IL, 1-hexyl-3-methylimidazolium bis(trimetheylsulfonyl)imide ([hmim][Tf2N]), was deposited on top of the device using a micropipette covering the area exposed by the developed photoresist. The samples were measured in a Quantum Design Physical Properties Measurement System (PPMS) using two Keithley 2400 source measure units. Transfer and output measurements are conventionally used in studying transistor behavior, in which the gate and the drain are commonly grounded, biased separately, and the currents are recorded. The transfer curves were measured with the gate electrode being biased from -1 V to 2 V in step sizes of 0.02 V for each source-drain bias from 0.1 V to 1.1 V in step increments of 0.25 V. The measurements show a standard transistor behavior, similar to that seen in previous IL gated a-IGZO devices[73, 86, 96]. The maximum current of the transfer curves, which are displayed in figure 2.2, were compared across the different channel to gate ratios with the 1:1 device having a maximum current of approximately 110 μA, the 1:10 device has a maximum current of 205 μA, which is an 186% enhancement over the matched area device, the 1:25 device has a maximum current of 234 μA (212% enhancement), and the 1:50 device has a maximum current of 382 μA (347% enhancement) at 1.1 V applied across the source drain electrodes. For the output measurements, the drain voltage is swept from 0 V to 1 V at increments of 0.02 V for each gate voltage as it is varied from 0 V to 2 V in steps of 0.5 V, and these curves reinforce the trend seen in the transfer curves, displaying an enhanced current going from 90 μA to 145 μA (161%) to 190 μA (211%) to 257 μA (285%) as the ratio between the area of the active channel and the gate electrode increased from 1:1, to 1:10, 1:25 and 1:50, respectively.

These devices were designed with sharp edges and variable spacing between gate electrodes and the active channel, which could lead to non-uniform electric fields in conventional dielectrics, and impact device efficiency. To determine how this geometry affects the operation of the transistor, new devices were designed with a circular layer of a-IGZO and concentric source drain electrodes, the source being a small diameter

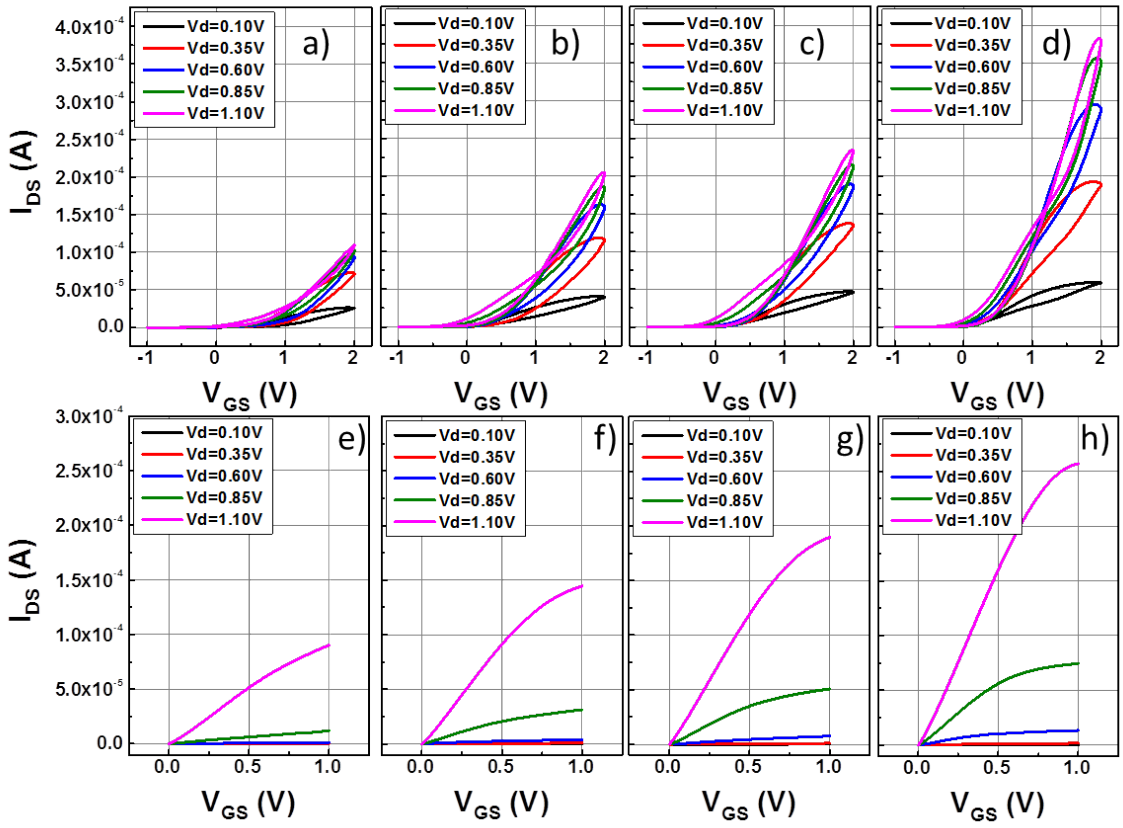

Figure 2.2: (a-d) Transfer curves for devices with channel to gate area ratios of a) 1:1, b) 1:10, c) 1:25, d) 1:50. (e-h) Output curves for devices with channel to gate area ratios of e) 1:1, f) 1:10, g) 1:25, h) 1:50.

circle, and the drain being an arc around the outside of the a-IGZO layer with a spacing of 20 μm to match the source-drain spacing in the rectangular shaped devices. The gate electrode was deposited as an arc with a constant spacing of d = 40 μm from the center of the active region of the device. These devices again had a varied gate electrode size with respect to a constant active channel area. Additionally this device was created with a chromium electrode patterned underneath the SiO_2 layer on which all the devices are grown, to be used as a comparative metal-oxide-semiconductor field effect transistor that utilizes the same active channel but in a standard solid-solid gate type. A second device was fabricated in the same way, but with an increased gate-to-channel spacing, d = 240 μm. Device one was fabricated using gate to channel area ratios of 1:1, 1:5 and 1:10 to compare to the square channel device, while device two was fabricated using gate to channel area ratios of 1:0.25, 1:1, and 1:10 to include a gate that is smaller than the active channel, and to directly compare the spacing between the gate electrode and the active channel. Both devices were similarly created with a photoresist reservoir to isolate the non-active parts of the devices, and contain the regions affected by the IL. Overlaid schematics and optical micrographs of these devices are shown in figure 2.3. [hmim][Tf_2N] was deposited within the photoresist reservoir and the transfer properties of the samples were measured, using the measurement parameters described above and shown in figure 2.4. The small spacing sample had a similar trend of increasing the source-drain current at a drain voltage of 1.1 V and a gate voltage of 2 V from 451 μA for the 1:1 device to 826 μA (183%) for the 1:5 ratio and to 889 μA (197%) for the 1:10 ratio. The increased current for this series of devices resulted from the larger area of the active channel between the source and the drain on the device. Thus, while the absolute current naturally varies with the active channel area, the IL gate enhancement depends on the ratio of the active channel area to gate area.

The devices with the increased distance between the co-planar side gate electrode and the active channel were fabricated with channel-to-gate area ratios of 1:0.25, 1:1, and 1:10 in order to evaluate both the area ratio and the distance between the gate

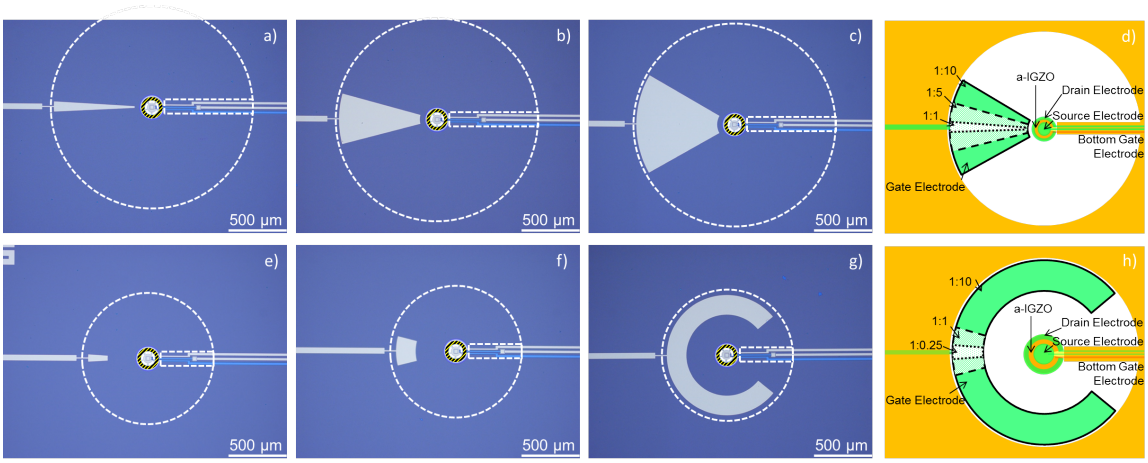

Figure 2.3: Circular patterned devices. (a-c) Optical images of devices with small spacing of d = 40 μm with channel to gate area ratios of a) 1:1, b) 1:5, c) 1:10. d) A schematic of the small spacing device with the different gate electrodes overlaid, and the photoresist covering the non-active area. (e-g) Optical images of devices with large spacing of d = 240 μm with given channel to gate area ratios of e) 1:0.25, f) 1:1, g)1:10. The active a-IGZO channel is shown in a striped yellow and black region. h) A schematic of the small spacing device with the different gate electrodes overlaid, and the photoresist covering the non-active area.

electrode and active channel. The 1:0.25 ratio device shows a predictable decrease in the source-drain current of 207 μA (47%) compared to 438 μA in the 1:1 device. While the 1:10 device shows a high maximum current of 877 μA (200%), which is the same order as for the small spacing device. The absolute current for the two samples was compared for the 1:1 and 1:10 ratios to see the impact of the change in the electrode distance for IL gated materials when the source drain dimensions remain constant. The two devices show nearly identical maximum currents, with overlaid plots given in figure 2.5 demonstrating currents of: 451 μA vs 438 μA for the 1:1 device, and 889 μA vs 877 μA for the 1:10 device. These maximum currents have less than a 2.5% change in current with a 6 fold increase in gate to active channel spacing, demonstrating the relative insensitivity of the gate electrode offset distance from the active channel. This is an important observation as it indicates that device designs based on IL gating can have a great deal of flexibility in where the gate sits in relation to the channel region.

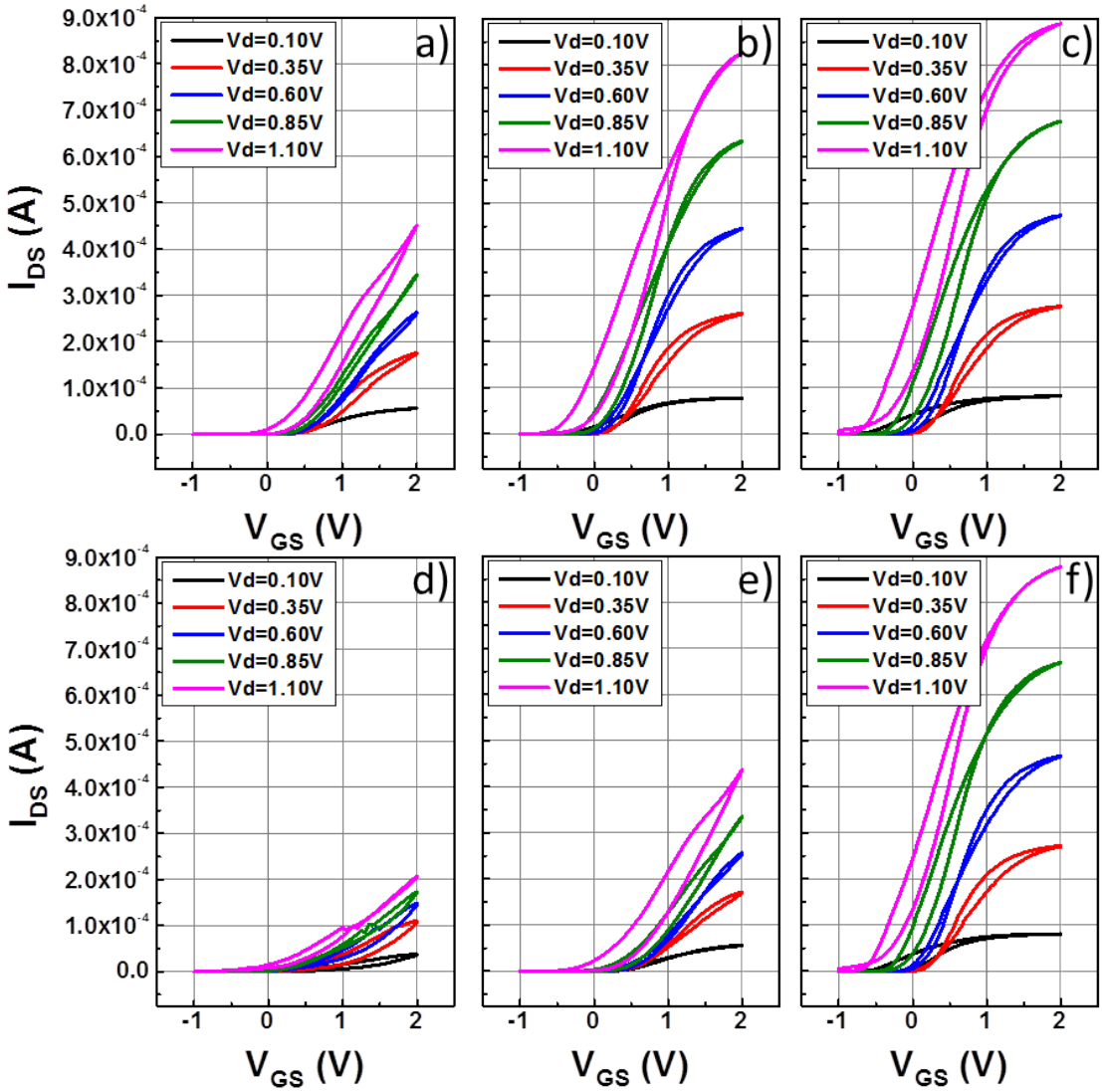

Figure 2.4: Transfer curves for the round patterned devices. The top row shows curves for the devices with gate electrode spacing of d = 40 μm and channel to gate area ratios of a) 1:1, b) 1:5, c) 1:10. The bottom row shows curves for the devices with gate electrode spacing of d = 240 μm and channel to gate area ratios of d) 1:0.25, e) 1:1, f) 1:10.

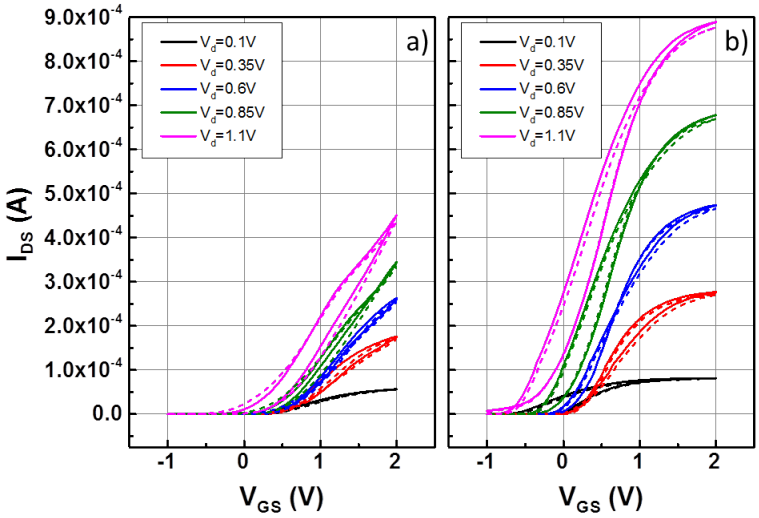

Figure 2.5: Overlay of round device with channel to gate ratios of a) 1:1, and b) 1:10 for direct comparison. The solid curve is for the small spacing of the gate electrode, d = 40 μm, while the dotted curve is for the large spacing of the gate electrode, d = 240 μm.

All the transfer curves measured in this study show an interesting hysteresis between the forward sweep and the reverse sweep of the measurement. To determine the cause of this, the same devices were probed using the patterned chromium bottom gate electrode, using a 100nm SiO_2 insulating layer as a conventional gate dielectric, and acting as a standard field effect transistor (FET). The measurement parameters were changed, due to the decreased charge accumulation that occurs from oxide gated devices as compared to IL gated devices, to a drain voltage of 10.1 V and a gate voltage sweep from -10 V to 20 V. This measurement was done on each of the different 6 IL devices to display the uniformity of the device fabrication and is plotted in figure 2.6. These comparative solid-solid FET measurements have no hysteresis between the forward and reverse gate biases. This is further confirmation that IL-gated devices are capable of driving oxygen ion transport through the underlying a-IGZO layer at very low absolute applied biases and at relatively short time scales[73].

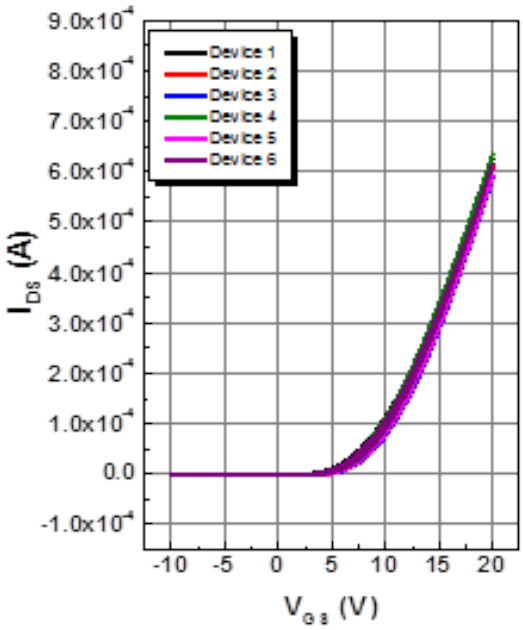

Figure 2.6: Bottom gate transfer curves for round devices. The bottom gate data shows standard transistor curves in which there is no hysteresis from the forward sweep and reverse sweep and highly uniform measurements across the different devices.

The current increase observed through the active channel at higher voltage and higher gate/channel area ratios is attributed to an increase in the interfacial charge, caused by a densification of the ions at the surface. As the gate size increases there is a greater surface area leading to an increased number of ions that can accumulate at that electrode under an applied bias. In order to maintain a neutral charge balance within the IL, the larger number of ions that migrate to the biased gate electrode must equal the number of oppositely charged ions collected at the counter electrode. The densification of these ions can occur by the ion packing, re-orientation or increases in the number of paired ion layers that form on the interface[69, 95].

Devices of varying geometry were fabricated and measured to demonstrate the effects of their gate to channel size ratio, distance between, and absolute geometry on the efficiency of ionic liquid gating. Our results show that the ratio of the gate to channel area is the most significant factor affecting the transistor characteristics of the devices. We observed that a change of an order of magnitude in the area ratio nearly doubles the maximum current in these devices, ascribed to the greater charge accumulation at the IL-solid interface. This charge accumulation is much less affected by other geometric constraints such as the absolute area of the gate for a given electrode ratio and the offset spacing between the gate electrode and the active channel. We also observe that the current continues to be enhanced with increasing gate size, which shows diminishing returns as the gate size continues to increase. These findings offer essential guidance in the optimization of IL gated devices designed for electrostatic and ionic control of functional materials.

Chapter 3

Probing Ionic Liquid-Solid Effects Through an Ionic Liquid-Ferroelectric Interface

3.1 Preface

A version of this chapter will be submitted for publication by A. T. Wong[1,2], A. Herklotz[2], Y. Sharma[2], A. Ievlev[3], D. Lee[2], T. Meyer[2], O. Ovchinnikova[3], N. Balke[3], H.N. Lee[2], P.D. Rack[1,3], and T.Z. Ward[2]

3.1.1 Author Affiliations

[1] Materials Science and Engineering Department, University of Tennessee, Knoxville, 37996, TN USA

[2] Materials Science and Technology Division, Oak Ridge National Laboratory, 1 Bethel Valley Rd., 37839, Oak Ridge, TN, USA

[3] Center for Nanophase Materials Science, Oak Ridge National Laboratory, 1 Bethel Valley Rd., 37839, Oak Ridge, TN, USA

3.1.2 Contributions of Authors

Dr. Meyer, and Dr. D. Lee each deposited samples for this study. The work done here was in conjunction with a study of interfacial magnetism which was conducted by Dr. Herklotz, and Dr. Meyer [97], in which I conducted the IL induced ferroelectric polarization switching for the polarized neutron reflectometry. This paper is currently in preparation to be submitted. I will be updating this section of the thesis as changes are made to the document to be submitted.

3.2 Background of Ionic Liquid - Ferroelectric Experiments - Not Included in to be Submitted Work

Our research on ionic liquid devices started with fabricated thin films, similar to other small scale work that had been conducted by other groups[66, 70–72, 74, 75]. The fabrication of these devices seemed simple enough, however it quickly became apparent that device fabrication was not quite so easy. Original versions of IL devices included crudely rigged devices, particularly one that had a conducting plate, mounted on insulating ceramics and glued with GE varnish to be suspended over the sample. This conducting plate had a threaded hole machined into the middle and a screw was connected. This screw was used as the gate electrode which was precisely raised and lowered into the dropped ionic liquid on the surface of the sample. These samples yielded minimal results which we found later likely had to do with the area ratios between the tip of the screw biasing the liquid, and the area of the sample to be measured.

Additionally the electrical measurement of ionic liquids proved difficult to understand as the liquid systems have associated time constants in which the ions migrate to their electric double layer positions. These measurements commonly continued to change current readings from constant applied voltages for time scales on the order of minutes.

Using the idea of creating an electric double layer, we decided to experiment using ionic liquids as a macro-scale technique for measuring the surface polarization of ferroelectric BFO. In this measurement, we expected the surface polarization to induce the electric double later, which would create a voltage drop that could be measured through a voltage sense Keithley 2400/2450 source measure unit. The resulting voltage was a measurable value, however inconsistent from one measurement to the next as the voltage reading would sometimes switch signs depending on the

measurement time, making it difficult to elucidate the meaning of the measured voltage. This measurement seeded the idea that the opposite use of ionic liquids would be possible in ferroelectrics. While unable to determine the meaning of the voltage received from ferroelectric films, the application of a voltage would allow us to control the ordering of the electric double layer on the surface of these films.

Applying the voltage to the entire surface (or defined area on the surface) of the films required a method of controlling the IL coverage. Previous attempts at containing ionic liquids to a specific area included creating "wells" out of insulating films or photoresists. These were relatively effective for small areas of $< 1\text{mm}^2$, but for larger areas the surface tension of the liquid would wet to any gate material applied, causing the liquid to move off the film in an uncontrolled way. We considered the idea of using ionic gels before deciding on polymeric membranes as a way of absorbing the ionic liquid, and containing it into a specified region. These membranes were connected to a conducting tape - originally carbon tape, and eventually aluminum foil tape which provided electrical access to the IL soaked polymer. We experimented with specified pore size membranes, and also with Kimwipe laboratory wipes and found no difference, therefore leading us to use Kimwipes for our studies.

3.3 In preparation version of "Probing Ionic Liquid–Solid Effects using an Ionic Liquid–Ferroelectric Interface" to be submitted

3.3.1 Abstract

Ionic liquids have been studied intensively in the past decade for their unique properties, especially when combined with complex oxide solids. The extremely large electric fields (on the order of 8×10^{14} charges/cm^2) are orders higher than can be achieved using conventional dielectric materials. Additionally, because the charges are applied through ionic species, not electronic species, the charge accumulation maintains its voltage drop when its connected between metals. The combination of high electric field, and ionic charges make ionic liquids ideal for switching large areas of ferroelectric films in ways previously unobtainable. We demonstrate that large areas of ferroelectric $Pb(Zr_xTi_{1-x})O_3, x = 0.2$ (PZT) film can be switched using ionic liquids, and amazingly that even thin films susceptible to tunneling currents and leaky films with high leakage currents can be switched using this method. We show that the ionic liquid does not negatively impact the fast electronic switching fatigue of the film, and improves the slow switching properties of ferroelectric PZT.

3.3.2 Probing Ionic Liquid-Solid Effects Through an Ionic Liquid-Ferroelectric Interface

Material growth quality is one of the greatest challenges in scaling up advanced electronic materials from laboratory research scale systems that require ultra-high vacuum and deposit small areas at once, such as pulsed laser deposition or molecular beam epitaxy, to industrial scale production techniques such as evaporation,

sputtering or chemical vapor deposition. While there are always ongoing studies to improve the quality of material growth in high efficiency systems, another method in advancing electronic materials is finding ways to utilize less than perfect materials. It is in this scenario that we look to interface room temperature ionic liquids with ferroelectrics as a multi-faceted study in which we explore the effect that ionic liquids and the formation of electric double layers have on ferroelectrics, and utilize the ferroelectric material as a way of *ex situ* monitoring the ionic liquid and how it could behave on comparable electronic materials.

Room temperature ionic liquids (IL) are polymeric materials that are comprised of 2 ionic components that are liquid not dissolved in solvent near room temperature[73, 98]. Cationic and anionic species coexist in a charge neutral liquid, however under an applied bias, these charged ions segregate to the anode and cathode, respectively in these device setups[73, 81, 92, 99]. IL-solid interfaces have garnered broad interest recently for their wide range of properties, and their ability to control, manipulate, and elevate unique phenomena that can arise in the affected solid materials[66, 70–72, 74, 75]. A wide variety of material systems have been evaluated using IL gating, often requiring advanced fabrication techniques to study small scale results of materials such as graphene, 2-d layered dichalcogenides and complex oxides for their uses as electronic, magnetic and neuromorphic material systems[76, 90, 94]. Some of the properties tested have included electrostatic control inducing superconductivity, semiconductor gating and ionic control, inducing lithium ion intercalation and oxygen stoichiometry control, providing new and unique controls techniques for these materials[66, 70–76, 90, 94]. Despite the vast studies of IL-solid interfaces an understudied field is how IL can impact large area in unconventional ways.

Ferroelectrics are well known materials in which non-centrosymmetric inversion symmetry leads to spontaneous domain polarization that are researched intensely for advanced electronic applications[40–42, 100]. There are many known issues related to ferroelectrics and their large scale incorporation into various applications,

which include defect-induced electronic shorts, fatigue related breakdown, and an inability to utilize large areas[40–42, 101]. It has also recently been shown that the switching mechanisms in ferroelectric materials appear to be dramatically more complex than has been conventionally assumed[102, 103]. As ferroelectrics retain a set polarization state that can be measured *ex situ*, these materials can be used as a framework material system for evaluating ionic liquid-solid interfaces as a means of quantifying the electric double layer that is formed, but additionally we can employ these methods to evaluate unique properties in ferroelectric films. The combination of IL and ferroelectric solid properties can be implemented into new technologies, such as large scale multiferroics, advanced scattering characterization techniques requiring large scattering cross sections, or direct electronic gating without dielectric materials[39–44, 92, 104, 105]. We demonstrate in this letter how the combination of IL and ferroelectrics opens up new routes in manipulating ferroelectric films that were previously unavailable.

For these experiments we selected $Pb(Zr_xTi_{1-x})O_3, x = 0.2$ (PZT) as the ferroelectric film, as it a well-known ferroelectric ceramic with tetragonal symmetry, leading to 180° domain walls and c-axis polarization[100, 106, 107]. 3 separate PZT films were fabricated, one 43nm with a 6nm $La_{0.7}Sr_{0.3}MnO_3$ (LSMO) back electrode on 10 mm x 10 mm (0 0 1) oriented $SrTiO_3$ (STO) using pulsed laser deposition (PLD) growth methods at Growth Specifications which will be referred to as the thick sample; one with 7nm of PZT using a 6nm LSMO back electrode which will be referred to as the thin sample; one with 18nm of PZT using 6nm of rough $SrRuO_3$ (SRO) as the back electrode to induce leakage channels through the film roughness which will be referred to as the leaky sample. XRD measurements are included in the suplemental information, and were used to determine that the proper material phase was grown, and confirm the thicknesses of the films. In figure 3.1, a schematic is given for the experimental setup in which the back gate of the film is grounded by contact through a scratch on the surface of the film and applied silver paint, and connected via a voltage source applying a positive voltage. The IL gate is created by taking a

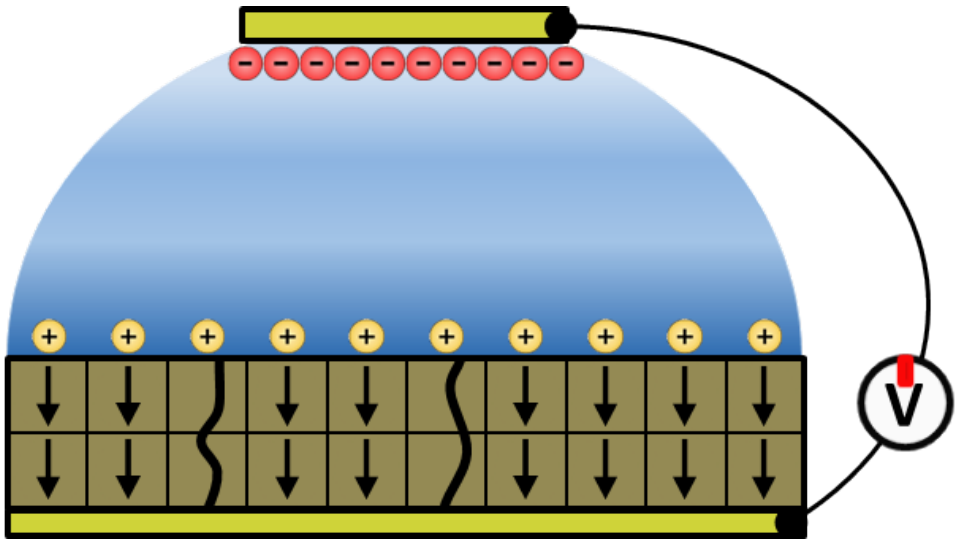

Figure 3.1: Schematic of an ionic liquid device as applied to a ferroelectirc film. In this schematic a positive bias is applied, causing the negative ions to accumulate at the gate electrode, and the positive ions to accumulate that the interface of the film. These positive ions remain at the surface, despite the leakage shorts shown by the vertical curved lines. The positive ions induce a down orientation or one where the surface potential is negative.

conductive Al foil tape with a Kimwipe used as an absorbent membrane soaked with IL to control the area where the liquid is applied, verifying the area of the gate remains at a 1 : 1 ratio with respect to the affected area of the sample[81]. The IL top gate and the back electrode are contacted using micromanipulator probes and electrically controlled using a Keithley 2400 source meter. The IL used in this experiment is 1-Butyl-3-Methylimidazolium-Bis(trifluoromethylsulfonyl)imide (Bmim-Tf_2N), due to its relative insensitivity to atmospheric moisture, and proven efficiency in other IL gating experiments.

As grown films are initially measured using Piezoresponse Force Microscopy (PFM) to determine the orientation of the spontaneous polarization that occurred during film deposition. Using a Pt coated contact cantilever tip, biases are written using a concentric square method to write a known contrast onto the film, against which the remainder of the film is measured. The first square with a size of 2μm is written with a +4V bias applied across the film from the tip to the LSMO backgate.

The second square is 1μm and written with a -3V bias from the tip to the back gate. The resulting 3μm square was measured with 0V tip bias in order to read out the polarization state which appears as a 2 separate phases, 180° out of phase from each other, yielding a graphical contrast of light and dark coloration[100]. The thick and thin films in figures 3.2a and 3.2d match the inner written square (-3V bias), depicting that the films are grown with a positive surface charge, or by convention in a poled up orientation. IL is applied to approximately half of the as grown thick PZT film, and a series of biases are applied, increasing from +1V to +4V, with the intermediate non-switching biases seen in supplementary data. After each applied bias, the IL is removed from the surface using organic solvents and deionized water, and dried with nitrogen. PFM measurements are conducted to determine the final polarization after the IL bias is applied, and demonstrates that the +4V bias successfully switches the region of the film where the ionic liquid is applied, depicted in figure 3.2b. This switching occurs as a consequence of the interfacial charge that is built up due to the ions that align at the surface of the film, switching the film to the down polarization. While expected that a thick film should be switched due to an interfacial charge, thin PZT films (and other ferroelectrics) experience difficulty in conventional electronic switching due to an inability to hold the surface bias because of leakage currents[39, 106–108]. However the difference in how IL biases are applied could provide an effective means of switching as compared to conventional electrodes, because the imparted charge comes from ionic species rather than electronic ones. We applied IL to approximately half of the surface of the film, again doing a series of biases from +1V to +4V and using PFM to determine the polarization of the film. Again a bias of +4V is sufficient to switch these films shown in figure 3.2e, whereas the lower biases are not (seen in supplemental data). A negative bias of -4V is applied to each of these films, and similarly cleaned to demonstrate the reversibility of these films in figures 3.2c and 3.2f, consistent with conventional electronic switching of ferroelectric materials.

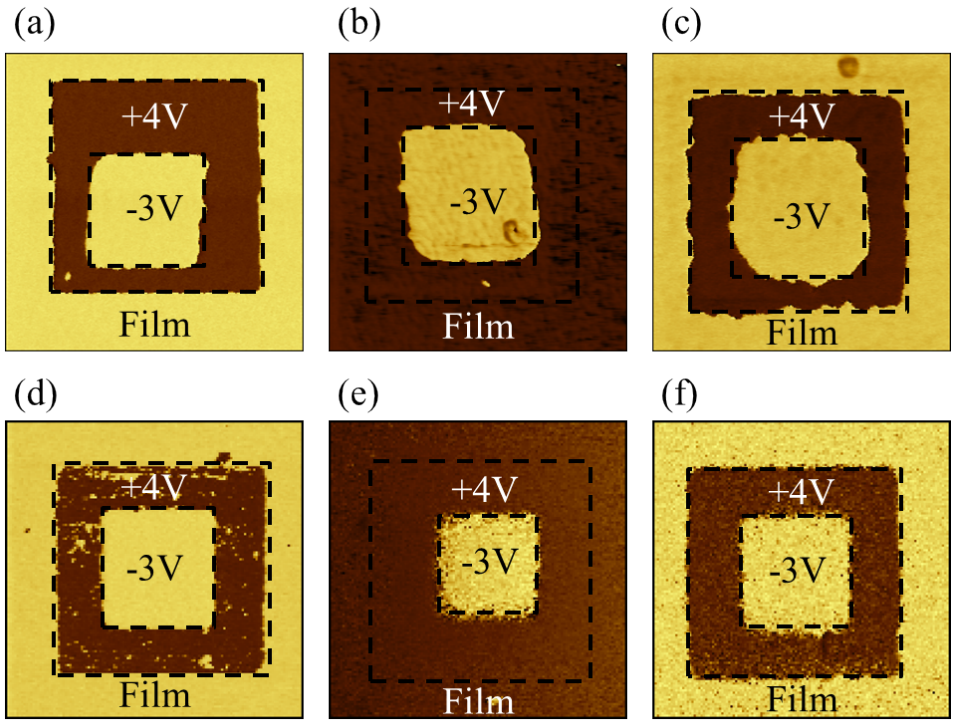

Figure 3.2: Switching series for (a)-(c) thick film, and for (d)-(f) thin film. (a) and (d) are respective as grown films, with the 2μm square written with a +4V bias and the 1μm square is written with a -3V bias. The film region matches the 1μm written square indicating a polarization up film. (b) and (e) are the respective films after an ionic liquid bias of +4V applied. The film region matches the 2μm written square indicating a polarization down film. (c) and (f) show the films after being switched back using a -4V applied bias to the original polarization up orientation.

While conventional electrodes are susceptible to electronic defects, tunneling leakage currents and other mechanisms that could prevent switching, the ionic charge from the IL retains its charge buildup due to the large ionic species that do not short electrically through these defect sites, and maintain a bias across the film[42]. To test this hypothesis we grew PZT films on intentionally roughened $SrRuO_3$ back electrodes that have regularly spaced large particles of phase pure SRO. The large particles prevent fully dense crystalline PZT from growing directly on top of them, imparting electronic defects in the PZT film. In figure 3.3a atomic force microscopy (AFM) shows the roughened topography of the film with regular spacing of surface particles, yielding an average roughness of 1.37nm RMS. To confirm the conductivity of these particles we measured conducting-AFM (C-AFM) which shows a similar pattern of conductive channels in figure 3.3b, matching the topography of the film, whereas the area around these particles remain non-conductive, implying the high quality PZT film we see from the film's XRD pattern. Initial PFM from this film show in figure 3.3c again the as grown film in the polarized up orientation, however the 2μm written square demonstrates an inability to switch regions of the film that match the topographic features from AFM measurements, and conductive features from C-AFM measurements. An IL bias of +4V was applied from the surface of the sample, and through the film to attempt to switch the polarization of the film. PFM measurements after the IL was cleaned from the sample show in figure 3.3d the dark contrast of the down oriented film for the area surrounding the topographic features, but still the topographic features remain in the as grown state. Additionally, this IL biasing technique opens the opportunity to apply a bias across a large area of the film, as compared to locally biased small scale electrodes. A series of fiducial marks are deposited across the center of the film, across the biased and unbiased region seen as black circles in figure 3.3e. Then using the same settings as the other PFM measurements, single scans were conducted across the film using the fiducial marks as spatial references, with measurements made at the depicted filled in circles to visualize the area polarized using the IL bias seen in figure 3.3e. The scans taken

on the as grown region of the film keep the bright color as compared to the written boxes, staying in the polarized up orientation, and the biased regions have the dark color contrast, corresponding to the switched polarization down orientation. While conventional electrodes would have been unable to maintain a charge bias across this film due to the leakage channels which would have shorted the voltage drop, the IL keeps the film bias despite the defects, allowing the high quality regions of the film to be switched while the leaky regions of the film continue to be inaccessible. These types of measurements could allow for increased usage of lower quality films, such as polycrystalline, phase impure films that have cheaper and faster production in many different applications, provided the film properties are not dramatically affected by the IL biasing.

Knowing the effective switching of the IL biasing, we chose to evaluate the film properties of the ferroelectric to determine if this switching technique is detrimental to the films, and therefore lead to difficulty in their integration into applied systems, specifically the fatigue properties of the system. Round platinum electrodes with a diameter of 100 μm were lithographically patterned and deposited using RF sputtering and a liftoff technique on a small region of the as grown film, and measured using an alternating triangle wave form with an amplitude of 4V, and a frequency of 1000Hz in a 100 μA range. Fatigue data in figure 3.4 shows the samples have a standard polarization of approximately 85 μC/cm^2 initially and that value decreases through 1 million cycles to approximately 74 μC/cm^2, only a 13% decrease in polarization. The samples were then biased through the IL at alternating voltages of $+/-4$V, each for 30 seconds for a total of 400 switches to the film. The IL was again removed, and a new set of pt electrodes were patterned and deposited on a region of the sample different from the initial region, to ensure that the new measurement are in a region that underwent IL bias switching. These new fatigue measurements show a slight decrease in the initial polarization of the film to approximately 83 μC/cm^2 and again show a minimal decrease in the film polarization through 1 million switches down to approximately 72 μC/cm^2, again only a 13% decrease in film

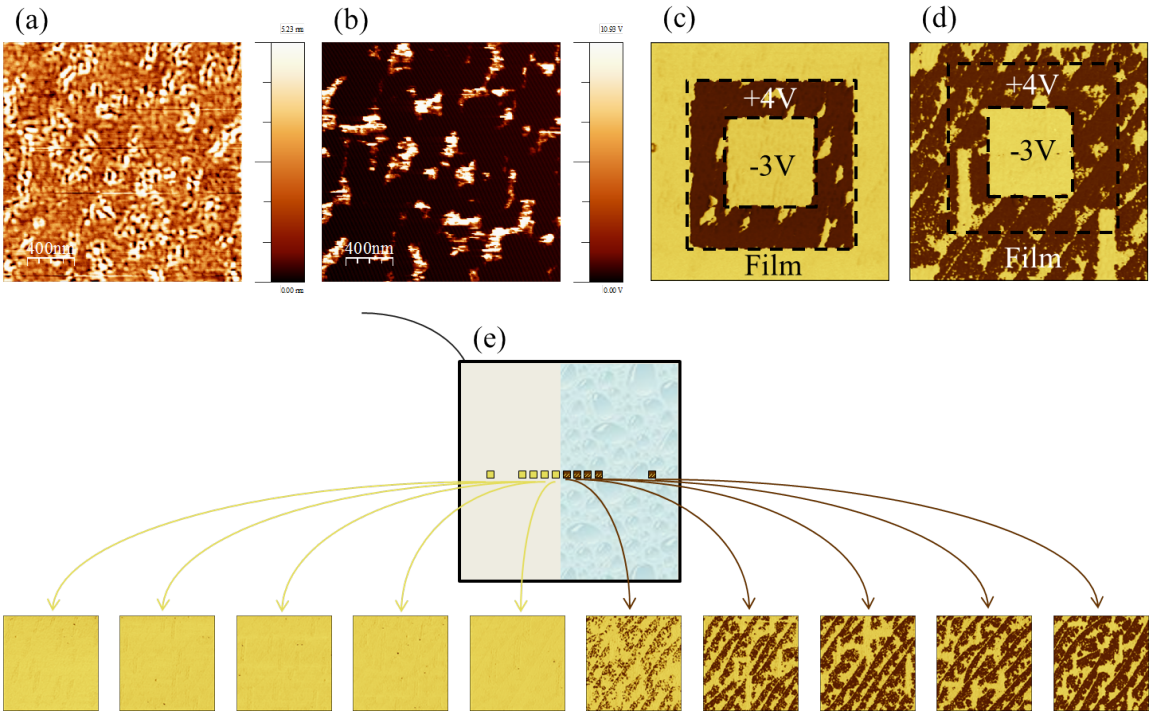

Figure 3.3: (a) Topography of the leaky film showing surface roughness. (b) Conducting-AFM measurement of the correspond area measured in (a). This measurement confirms that the areas of high roughness are also areas of high leakage current. (c) The as grown film PFM measurement demonstrates the polarization of the as an polarization up orientation. The 2μm shows unswitched regions, corresponding to the topographically rough regions. (d) The film after a +4V ionic liquid bias. This measurement shows the switching of the bulk of the film, but again unswitched ares corresponding to the topographically rough areas. (e) Single PFM scans of 3μm across the switched film. The left side of the film remains as grown, while the right side of the film has the applied ionic liquid bias. The right 5 measurements show an unswitched film while the left 5 measurements show the switched orientation of the film. The schematic shows the approximate location of each scan with respect to the PZT film.

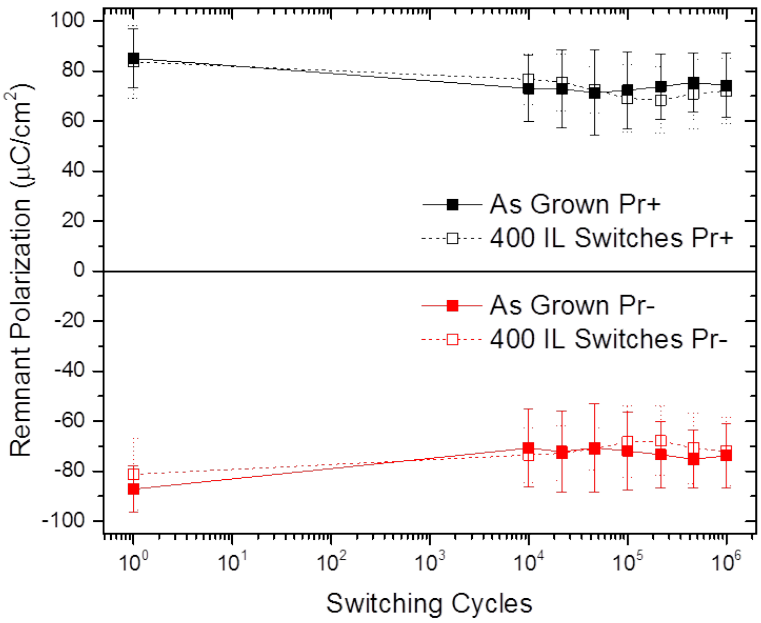

Figure 3.4: Ferroelectric fatigue measurements out to 1 million switches done at 100,000Hz . The solid markers are for the as grown film while the open markers show the film after 400 pulses of +4V/-4V for 30 seconds each. Each measurement is conducted on 10 individual spots and averaged with the electrodes for the ionic liquid switched test being deposited after the switching occurs.

polarization, helping to demonstrate that the IL biasing does not have a major effect on the films overall properties. We have grown PZT samples of various thicknesses and varying crystal quality and using IL applied ionic charge biases across broad areas of the films. We have found that the interfacial charge imparted by the IL is sufficient to switch the polarization orientation of the films, which was measured by PFM. Additionally the polarizations of all films were switched, regardless of the thickness or quality of the film, due to the unconventional mechanism by which the bias is applied to the films. Switching films using IL applied biases also shows a negligible effect on the ferroelectric properties of the PZT films, allowing the idea that this new method of controlling interfacial biases could be used in applications that require biases applied over large areas, or across imperfect films. This study also

demonstrates a framework for future experiments for studying other material systems that may require interfacial charge control over large areas like multiferroic systems, advanced scattering techniques, electronically leaky systems, direct electronic gating for materials incompatible with high-K dielectrics.

3.3.3 Future Work

After evaluating the fatigue measurements that were done, we realized that the comparison is not direct as the fatigue properties of ferroelectric films is highly dependent on the switching frequency. In order to confirm this measurement, we must evaluate the film under conventional switching at the same time scale as is used in ionic liquid switching[109]. To do this we are currently measuring as grown film fatigue properties under a 0.03Hz frequency, which is roughly 30 seconds of applied bias. The fatigue bias should be applied in the form of a square function to again match the switching pattern done using ionic liquid biases. The slow fatigue measurement should provide a better understanding to the comparative quality between the IL switched film and the conventionally switched film.

3.4 Supplemental Information

Figure 3.5(a) shows the $\theta - 2\theta$ scans for these films and figure 3.5(b) the x-ray reflectivity confirming the high quality deposition, and the thicknesses of the films interrogated in this work. The (0 0 2) peak of the PZT film occurs at approximately 43.5° for the thick sample, and at approximately 42.8° for the two thinner samples, which is expected as the thicker films are more likely to relax from a strained state towards the bulk lattice constants. XRD scans also confirm the phase pure back electrodes, with the thick and thin samples having the LSMO (0 0 2) peaks on the right shoulder of the STO (0 0 2) peak, and the leaky sample having the SRO (0 0 2) peak on the left shoulder of the substrate peak. The reflectivity scans yield strong internal reflections, which in combination with the Kiessig fringes from the diffraction scan confirm the thicknesses of the samples. In figure 1c a schematic is given for the experimental setup in which the back gate of the film is grounded by contact through a scratch on the surface of the film and applied silver paint, and connected via a voltage source applying a positive voltage.

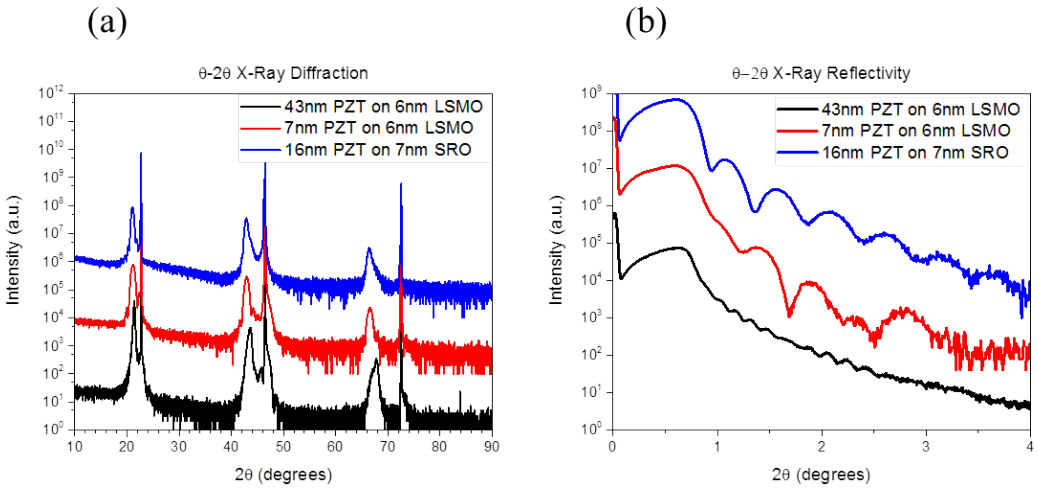

Figure 3.5: (a) $\theta - 2\theta$ x-ray diffraction scan aligned on the STO (0 0 2) substrate peak. The left shoulders show coherent film peaks for the thin and leaky sample with the thick sample showing a relaxed film peak. (b) $\theta - 2\theta$ x-ray reflectometry used to confirm the film thickness using X'Pert Reflectometry software.

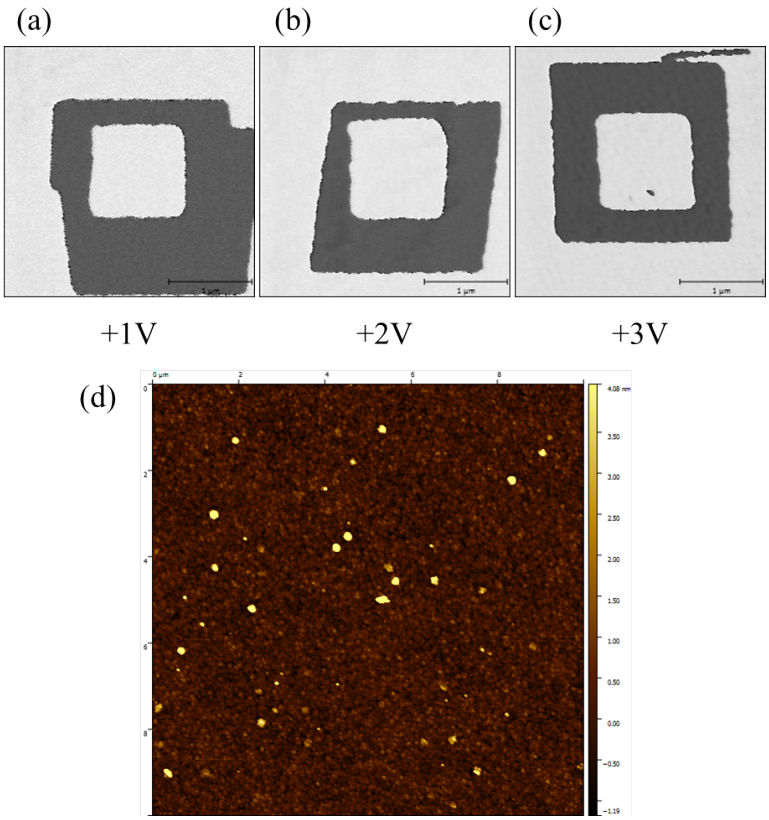

Figure 3.6: PZT film after ionic liquid biases not high enough to induce switching. (a), (b) and (c) show PFM measurements for +1V, +2V and +3V biases applied through the ionic liquid. (d) AFM topography giving the relative roughness of the film.

The non switching voltages are shown in figure 3.6(a)-(c). The applied voltages are applied through the ionic liquid using the top gate and removed from the sample using acetone, isopropyl alcohol, and deionized water under ultra-sonication. (a)-(c) reveal the film remaining in the up orientation for applied ionic liquid biases of +1V, +2V and +3V, respectively each for 1 minute. Figure 3.6(d) shows the atomic force measurement of the surface of the "thick" film demonstrating the relative roughness of the film.

Figure 3.7 shows a region of 3 stitched PFM loops, 15μm wide by 3μm tall combined for 45μm wide, for the leaky film that had a +4V bias applied for 3 minutes. This region was found using the fiducial marks on the surface of the film. The fiducial

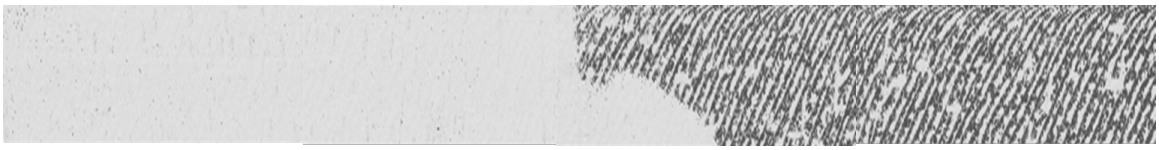

Figure 3.7: Stitched PFM scans across what appears to be the interface where ionic liquid biases are applied. The left side shows the as grown polarization up orientation, while the right side shows the switched polarized down orientation.

marks are approximately spaced every 200μm apart, causing the spacial resolution insufficient to accurately state the delineation of where the ionic liquid is applied to the surface, vs approximate region. While we can infer that the area switched is where the IL is applied, more specific studies must be conducted.

Chapter 4

Controlling Room Temperature and Ambient Pressure Topotactic Phase Transition in $SrCoO_3$

4.1 Preface

A version of this chapter will be submitted for publication by A. T. Wong[1,2], A. Herklotz[2], Y. Sharma[2], A. Ievlev[3], D. Lee[2], O. Ovchinnikova[3], P.D. Rack[1,3], H.N. Lee[2], and T.Z. Ward[2]

4.1.1 Author Affiliations

[1] Materials Science and Engineering Department, University of Tennessee, Knoxville, 37996, TN USA

[2] Materials Science and Technology Division, Oak Ridge National Laboratory, 1 Bethel Valley Rd., 37839, Oak Ridge, TN, USA

[3] Center for Nanophase Materials Science, Oak Ridge National Laboratory, 1 Bethel Valley Rd., 37839, Oak Ridge, TN, USA

4.1.2 Contributions of Authors

Samples for this work were grown by D. Lee. A. Herklotz and T.Z. Ward assisted in design and construction of the *in situ* electrochemical measurement cell.

4.2 In preparation version of "Controlling Room Temperature and Ambient Pressure Topotactic Phase Transition in $SrCoO_3$" to be submitted

4.2.1 Abstract

Phase changes in materials can lead to dramatic alterations in material properties. These types of changes can be utilized for creating functional devices, however often these transitions require specific environments to occur such as high temperatures, pressures or atmospheric conditions. Finding mechanisms and techniques allowing for these transitions to be manipulated at room temperature and/or ambient pressure could unlock these materials for use in applications. We explore the use of ionic liquids as a means of applying extremely large electric fields which can be used to move oxygen ions into and out of a crystal lattice. Using the $SrCoO_{3-\delta}$ crystal system, we explore the reversible ionic liquid switching from brownmillerite to perovskite using *in situ* XRD measurements.

4.2.2 Controlling Room Temperature and Ambient Pressure Topotactic Phase Transition in $SrCoO_3$

Phase transitions are a vital part of materials science, as they can lead to dramatic changes in physical properties as materials go from one phase to another. Often, phase transitions occur with changes in temperature, changes in doping or changes in stoichiometry; however enacting these transitions typically require very specific environments or treatments, such as temperatures, atmospheres, precursor materials,

or any combinations of these. Using these specific environments creates a new thermodynamically preferable phase, meaning in short, when the environment is reverted the original phase returns. An interesting application of these phase transitions arises when the phases can be controlled under a controlled, accessible environment between two stable or meta-stable phases[110–112].

$SrCoO_{3-\delta}$ is a complex oxide material that has garnered recent interest for its use as an oxygen transport material, specifically in oxidation evolution reactions, as use in solid oxide fuel cells, and more generally for the interesting properties that appear and disappear with relation to the oxygen stoichiometry[113–121]. There are 2 meta-stable phases at room temperature for the SCO system which are brownmillerite SCO (BM-SCO) with an oxygen stoichiometry of 2.5, and perovskite (P-SCO) with oxygen stoichiometry of 3. The topotactic transition between these two phases occur as alternating layers CoO_6 octahedra transform into CoO_4 tetrahedra, thereby opening channels seen in the (1 1 0) face of the P-SCO structure[113, 114, 116, 118]. Studies of this material include the magnetic, transport and optical properties of the differing films, many of which can be attributed to these open channels and demonstrating the dynamic changes between the different crystal structures. The brownmillerite phase is thermodynamically stable at lower oxygen partial pressures making it an easier phase to attain under common growth conditions; however techniques have been utilized to get the perovskite phase of the SCO, including high temperature post growth annealing under high oxygen pressure, ozone partial pressure, or under electrical bias[116, 118, 122–124].

Ionic liquids (IL) have been used in a diverse range of liquid solid interaction studies that examine the unique interfacial charges that build up due to the electric double layer formation when an electric bias is applied across the IL. This interfacial charge is transferred by ionic charge species instead of charged metal electrodes, and consequently yields interfacial charges that are orders of magnitude higher than can be conventionally achieved[65–67]. These immense interfacial charges can induce strong electrostatic and electrochemical effects in the base material, leading to

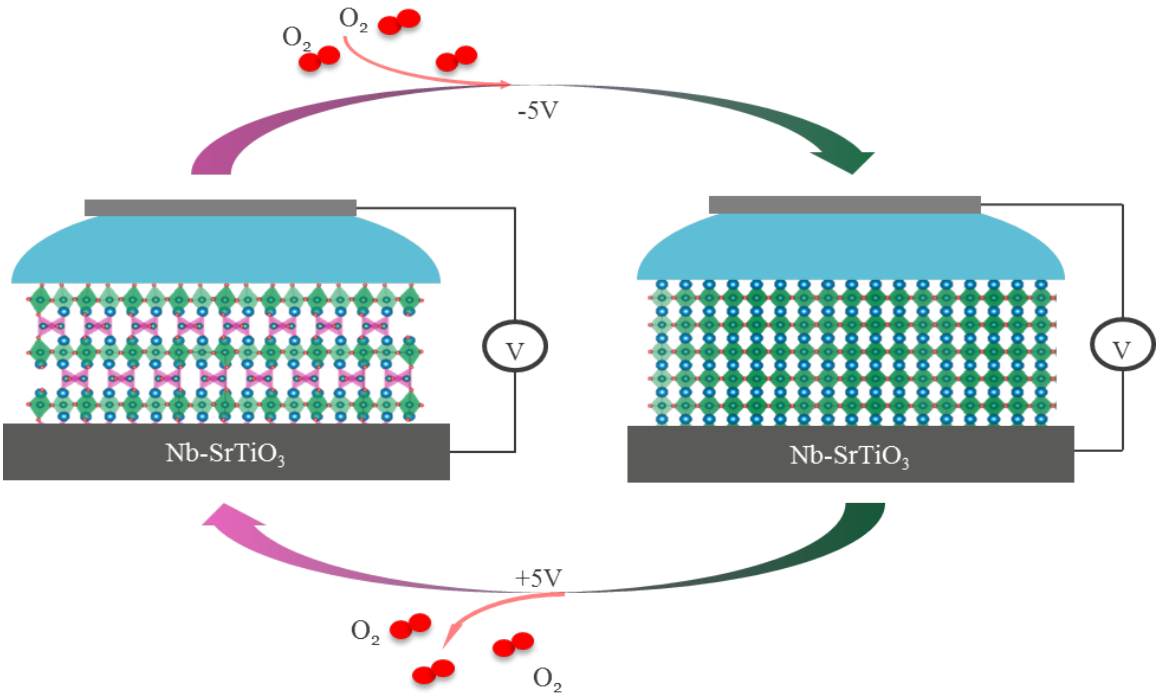

Figure 4.1: Schematic of room temperature, ambient pressure IL gated SCO. The substrate acts as the grounding point, and the gate contacting the IL is biased. On a negatively applied bias, oxygen from the atmosphere is moved through the liquid and inserted into the crystal lattice, inducing a stoichiometry controlled topotactic phase change. On a positive bias, the oxygen in the crystal lattice is pulled from the crystal into the ionic liquid, causing the reverse transformation.

phenomena such as superconductivity, metal-insulator transitions and semiconductor device activation[66, 67, 72, 74, 75, 83, 125]. Following the work of similar studies, IL may be the ideal system for studying electrochemical induced phase transitions, particularly at room temperature and ambient pressure environments.

Samples of brownmillerite $SrCoO_{2.5}$ (BM-SCO were grown on Nb-$SrTiO_3$ substrates using pulsed laser epitaxy. Standard single crystal x-ray measurements were conducted on the samples as grown and demonstrate a high quality single crystal of BM-SCO. The $\theta - 2\theta$ scans show the brownmillerite (0 0 4) and (0 0 8) peaks as shoulders to the left of the STO substrate (0 0 1) and (0 0 2) peaks respectively. We conducted rocking curve measurements on the substrate and the film, and demonstrated that both are highly oriented single crystal materials. Reciprocal space

scans were measured around the ($\bar{1}$ $\bar{1}$ 4) STO substrate peak which shows a nearby reflection of (2 2 15) of the BM-SCO film. The film peak aligns with the substrate peak in q_x reciprocal space therefore showing that the films are grown epitaxial to the Nb-STO substrate.

The high quality films were mounted in a homemade *in situ* x-ray cell to measure the $\theta - 2\theta$ scans under an applied ionic liquid bias[83, 117, 126]. The conducting substrate was contacted using copper tape on a glass slide, and remaining exposed portions of the copper tape were covered with insulating kapton tape. Additionally a piece of Pt foil was connected by copper tape to the glass slide near the sample, and exposed regions of the copper tape were again covered by kapton tape. A viton O-ring is attached around the outside of the Pt foil and the sample, creating a well like area to contain the ionic liquid. The IL, 1-Butyl-3-methylimazolium bis(trifluoromethylsulfonyl)imide ([Bmim][Tf2N]) was deposited into the well area created by the O-ring to cover the sample, the Pt foil and to nearly the top of the O-ring. At this point, a piece of kapton tape was attached over the top of the O-ring to seal in the IL such that the sample mounting can be rotated 90° and mounted onto the same panalytical 4-circle X-ray diffractometer. The kapton tape has a minimal effect in attenuating the x-ray intensity (approximately 1 order of magnitude) as it is received in the detector and therefore is used to seal the IL in contact with the SCO sample and the Pt foil. The samples are mounted and aligned such that the samples can be alternately measured around indicative peaks, and *in situ* biasing of the samples. The measurement scanned around the substrate, STO (0 0 2) at 46.54°, which captures the BM-SCO (0 0 8) peak near 46°, along with the P-SCO (0 0 2) peak near 47.7°. The as grown measurement confirms the BM-SCO phase remains even after mounting the sample into the *in situ* XRD electrochemical cell with the BM-SCO (0 0 8) peak appearing as a shoulder on the left side of the STO (0 0 2) peak. A series of alternating biases and measurements were conducted over short time periods at $-4V$ bias, the full timing sequence is given in table 4.1. The $-4V$ bias through a series of biases and measurements shows no change in the XRD peak

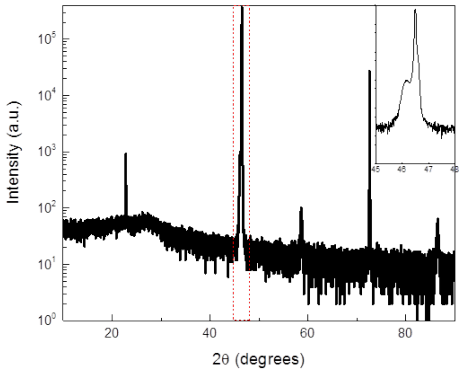

(a) Fig. 1

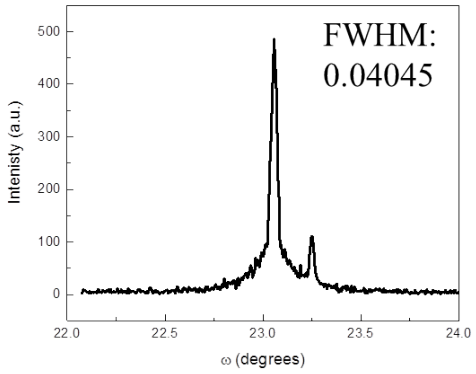

(b) Fig. 2

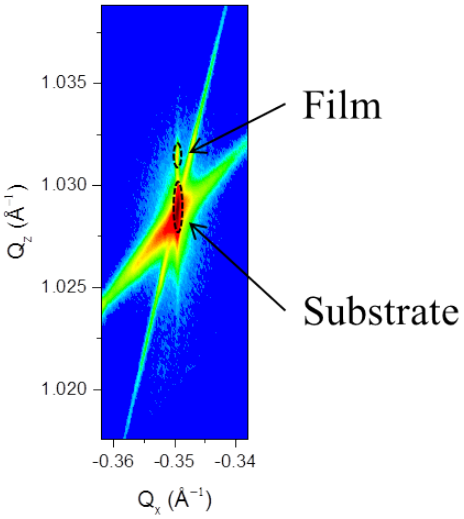

(c) Fig. 3

Figure 4.2: As grown x-ray characterization of BM-$SrCoO_{2.5}$ film. (a) $\theta - 2\theta$ scan aligned on the $SrTiO_3$ (0 0 2) peak. Substrate (0 0 1) peak is highly attenuated due to the *in situ* measurement cell. The inset show an enlarged view of the STO (0 0 2) peak, with the BM-SCO (0 0 8) peak on the left shoulder near 46.0°. (b) ω rocking curve of the film peak gives a narrow full width half max of 0.04045° demonstrating high crystallinity. (c) Reciprocal space map of the STO ($\bar{1}$ $\bar{1}$ 4) peak shows the BM-SCO (2 2 15) aligned in Q_x demonstrating film epitaxy.

positions, so the bias was increased to a $-5V$ bias. As the $-5V$ biases are applied to the IL, a sufficient electric field is applied to the surface to move oxygen ions into the crystal structure, which decreases the intensity of the BM-SCO (0 0 8) peak, and continually increases the intensity of the P-SCO (0 0 2) peak. After 7 cycles of biases, equaling 15:00 minutes, the intensity of the BM-SCO peak has decreased to the background levels, and the P-SCO has emerged, showing a complete shift from the BM phase to the P phase, which shows an incorporation of oxygen, changing the total stoichiometry from $SrCoO_{2.5}$ to $SrCoO_3$. A subsequent positive bias was applied to the same sample, in a series of alternating biases and measurements to observe the reversible effect of the IL biasing as it relates to the stoichiometric control of these crystals. A series of $+5V$ biases were applied to the IL and consequently to the crystal sample with the time sequence outlined in the methods section. The peak shift moves back from the P-SCO (0 0 2) peak to the BM-SCO (0 0 8) peak. This reversal happens as a much shorter time of applied biases as compared to the peak shift that occurs for the negative bias. The peaks shift within 10 cycles over 15:00 minutes back to the BM-SCO phase as indicated by the (0 0 8) peak.

The sample was removed from the *in situ* XRD electrochemical cell and cleaned using organic solvents. The samples were then re-measured to evaluate the final state, especially as compared to the as grown state, as for this effect to be truly reversible, the final state should match the as grown state. $\theta - 2\theta$ scans were conducted and demonstrate again a high quality, phase pure BM-SCO (0 0 8) oriented film peak on the same STO (0 0 2) substrate. We also again measured the ϕ scans which show a minimal widening of the FWHM of the film peak to 0.05284°, with respect to the as grown value. A reciprocal space scan around the STO $(1\bar{1}\bar{4})$ peak confirms that the film has remained locked epitaxial with respect to the substrate, demonstrating that the quality of the films is maintained through this topotactic phase transition.

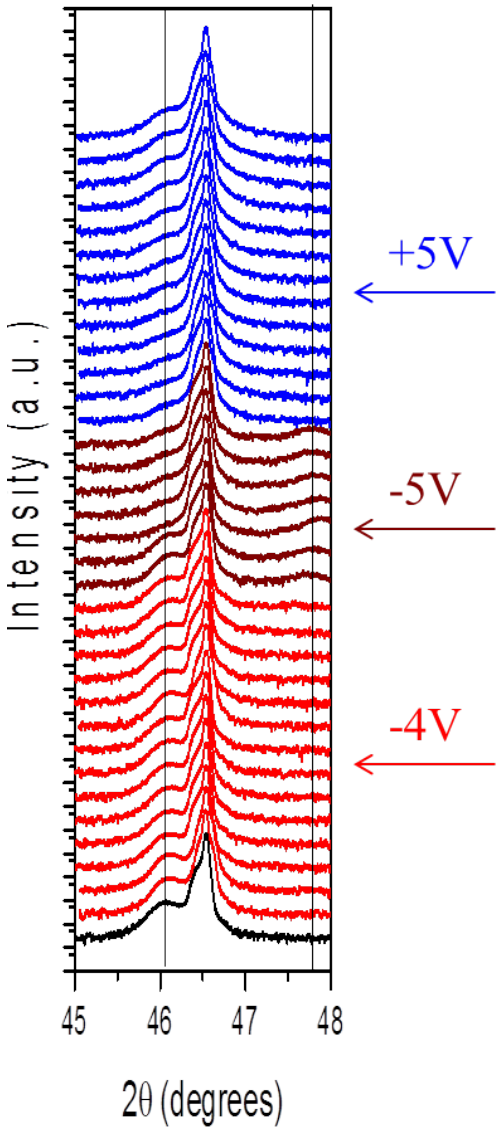

Figure 4.3: *In situ* xrd measurement of IL biased SCO. Time series for these measurements are seen in table 4.1. The peak near 46° is the BM-SCO (0 0 8) and the peak near 47.7° is the P-SCO (0 0 2). -4V is insufficient to switch the film, remaining in the BM-SCO phase. -5V switches the film, showing a brief state of mixed phase, before converting entirely to the P-SCO phase. +5V reverses the switch, showing after 15 minutes of total applied bias a switch back to the BM-SCO phase.

Table 4.1: Time sequence of applied ionic liquid biases between XRD measurements.

No.	Bias	Time	Total Time	Phase(s)
1	-4V	0	0	BM
2	-4V	15s	15s	BM
3	-4V	15s	30s	BM
4	-4V	15s	45s	BM
5	-4V	15s	1:00m	BM
6	-4V	15s	1:15m	BM
7	-4V	15s	1:30m	BM
8	-4V	30s	2:00m	BM
9	-4V	30s	2:30m	BM
10	-4V	30s	3:00m	BM
11	-4V	60s	4:00m	BM
12	-4V	60s	5:00m	BM
13	-4V	120s	7:00m	BM
14	-4V	120s	9:00m	BM
15	-4V	120s	11:00m	BM
16	-4V	120s	13:00m	BM
17	-4V	120s	15:00m	BM
18	-4V	120s	17:00m	BM
19	-4V	300s	22:00m	BM
20	-5V	120s	2:00m	BM, P
21	-5V	120s	4:00m	BM, P
22	-5V	120s	6:00m	P
23	-5V	120s	8:00m	P
24	-5V	120s	10:00m	P
25	-5V	120s	12:00m	P
26	-5V	120s	14:00m	P
27	+5V	15s	0:15m	BM
28	+5V	15s	0:30m	BM
29	+5V	15s	0:45m	BM
30	+5V	15s	1:00m	BM
31	+5V	15s	1:15m	BM
32	+5V	30s	1:45m	BM
33	+5V	30s	2:15m	BM
34	+5V	60s	3:15m	BM
35	+5V	60s	4:15m	BM
36	+5V	120s	6:15m	BM
37	+5V	120s	8:15m	BM
38	+5V	120s	10:15m	BM
39	+5V	300s	15:15m	BM

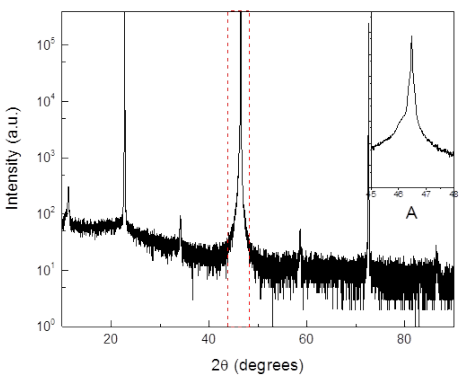

(a) Fig. 1

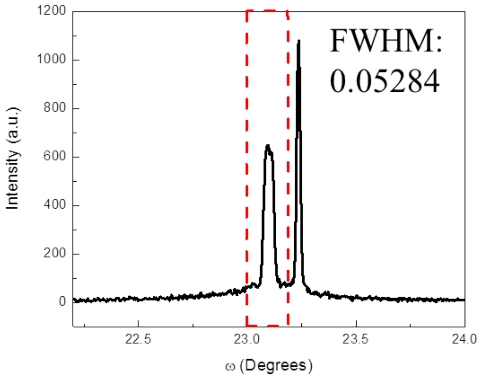

(b) Fig. 2

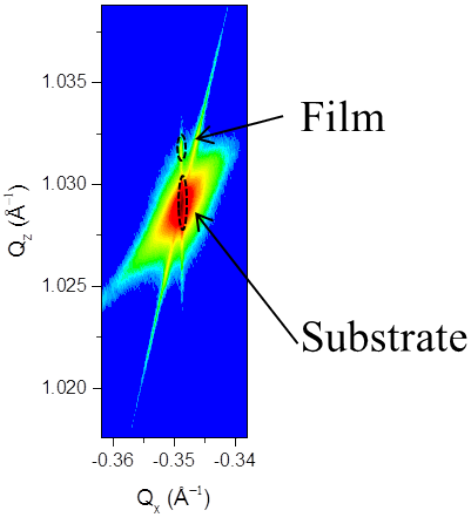

(c) Fig. 3

Figure 4.4: X-ray characterization of BM-$SrCoO_{2.5}$ film after switching through IL bias. (a) $\theta - 2\theta$ scan aligned on the $SrTiO_3$ (0 0 2) peak. The inset show an enlarged view of the STO (0 0 2) peak, with the BM-SCO (0 0 8) peak on the left shoulder near 46.0°. This film beak is slightly broadened from the as grown measurement. (b) ω rocking curve of the film peak gives a narrow full width half max of 0.05284° confirming the broadening of the film peak, however remaining in a relatively crystalline state. (c) Reciprocal space map of the STO ($\bar{1}$ $\bar{1}$ 4) peak shows the BM-SCO (2 2 15) aligned in Q_x demonstrating film epitaxy.

4.2.3 Future Work

The *in situ* measurement of these films, matched with the *ex situ* measurements of the films before and after switching show a complete reversible topotactic phase transition. The decrease in film quality from the as grown state, to the switched, and switched back state show that there is still a voltage and time optimization that needs to be done. This work could be aided through development of an improved multi-use electrochemical *in situ* cell for use in XRD measurements. Finer voltage and time steps will provide the precise switching parameters needed to effectively control the topotactic phase transition.

Once these measurements are confirmed, cycling of this crystal through the topotactic phase transition to determine the lifetime of the switched film is imperative, particularly for use in applications. Is is likely that the lifetime of such cycling is low, due to the defects that would be created from ionic species entering and leaving sices in the crystal lattice.

Our measurements are currently conducted on Nb-STO in order to create an effective back gate for the applied IL bias. Unfortunately the metallic Nb-STO prevents our ability to measure the the transport of the SCO films, and the magnetic signal is strong enough to prevent us from determining the film magnetism. These properties are what would enable the films to be used in reversible switching applications but acquiring these measurements could prove difficult. If we use a metallic back gate material, the transport properties could continue to be dominated by this film layer. There is a chance that the film itself could behave as the virtual ground for the IL biasing experiment, but that could add a layer of complexity as the virtual ground would be changing resistance as the film changes phases.

Additional measurements we are currently preparing and conducting includes using O^{18} as a tracer element to determine the IL induced filling mechanism, filling depth, and possibly the kinetics associated with the SCO topotactic phase transition[74, 127]. The sample is mounted with the previously stated IL gate, and

put in a vacuum chamber which is pumped into the 10^{-6} torr. The chamber is then back filled with O^{18} up to 150 torr. The chamber is then filled up to 760 torr with He to mimic atmospheric pressure, and atmospheric oxygen partial pressure. Bias is applied to insert oxygen into the crystal lattice and then the sample is measured using a Secondary Ion Mass Spectrometer, which sputters the film, and measures the sputtered ions. Knowing the beginning and ending oxygen stoichiometry will provide unique information as to how much oxygen is moved into the crystal lattice from the local environment. It will also be useful in determining the penetration depth of ionic liquid inserted species.

Chapter 5

Additional Research Contributions in Complex Oxide Crystals

5.1 Preface

A version of this work has been published by A. T. Wong[1,2], C. Beekman[1], H. Guo[1,3], W. Siemons[1], Z. Gai[4], E. Arenholz[5], Y. Takamura[6], and T. Z. Ward[1,a)] in Applied Physics Letters[128].

5.1.1 Author Affiliations

[1] Materials Science and Technology Division, Oak Ridge National Laboratory, Oak Ridge, Tennessee 37831, USA [2] Materials Science and Engineering, University of Tennessee, Knoxville, Tennessee 37996, USA

[3] Department of Physics and Astronomy, University of Tennessee, Knoxville, Tennessee 37996, USA

[4] Center for Nanophase Materials Sciences, Oak Ridge National Laboratory, Oak Ridge, Tennessee 37831,USA

[5] Advanced Light Source, Lawrence Berkeley National Laboratory, Berkeley, California 94720, USA

[6] Department of Chemical Engineering and Materials Science, University of California, Davis, Davis,California 95616, USA

5.1.2 Acknowledgements

This effort was supported by the U.S. Department of Energy (DOE), Office of Basic Energy Sciences (BES), Materials Sciences and Engineering Division, (T.Z.W., C.B., and W.S.) and under U.S. DOE grant DE-SC0002136 (A.W. and H.W.G.). Magnetization measurements (Z.G.) were conducted at the Center for Nanophase Materials Sciences, which is sponsored at Oak Ridge National Laboratory by the Scientific User Facilities Division, Office of BES, U.S. DOE. The Advanced Light

Source is supported by the Direction, Office of Science, Office of BES, of the U.S. DOE under Contract No. DE-AC02-05CH11231. Y.T. acknowledges the support of the National Science Foundation Contract No. DMR 0747896.

5.1.3 Contributions of Authors

In studying the LSMO crystal system, Dr. Ward and Dr. Guo made the initial target, and grew the initial samples for study, while I created the target used in later studies. Dr. Gai measured the sensitive magnetic moments of the antiferromagnetic samples. Dr. Takamura conducted the x-ray linear dichroism measurements.

5.2 A version of "Strain driven anisotropic magnetoresistance in antiferromagnetic $La_{0.4}Sr_{0.6}MnO_3$" accepted and published by Applied Physics Letters

5.2.1 Abstract

We investigate the effects of strain on antiferromagnetic (AFM) single crystal thin films of $La_{1-x}Sr_xMnO_3(x = 0.6)$. Nominally unstrained samples have strong magnetoresistance with anisotropic magnetoresistances (AMR) of up to 8%. Compressive strain suppresses magnetoresistance but generates AMR values of up to 63%. Tensile strain presents the only case of a metal-insulator transition and demonstrates a previously unreported AMR behavior. In all three cases, we find evidence of magnetic ordering and no indication of a global ferromagnetic phase transition. These behaviors are attributed to epitaxy induced changes in orbital occupation driving different magnetic ordering types. Our findings suggest that different AFM ordering types have a profound impact on the AMR magnitude and character.

5.2.2 Strain driven anisotropic magnetoresistance in antiferromagnetic $La_{0.4}Sr_{0.6}MnO_3$

Antiferromagnets (AFM) have been shown to be a promising alternative to ferromagnets (FM) in spintronic applications[27, 129–132]. The reason stems from the fact that at high data storage densities stray fields may destroy the FM set states, while an AFM would be relatively insensitive to these stray fields and maintain its anisotropic magnetoresistance (AMR). Recent studies have focused on AFM

bimetallics as they have high magnetic ordering temperatures and extremely low magnetizations[131, 132]. While strongly correlated oxides are considered to have immense promise in next generation electronic and sensing devices, few studies exist for AFM spintronic applications[30, 31, 107, 132–134]. In most cases, these materials have rich electron/hole doping phase diagrams populated with vastly different resistive and magnetic properties. Dopings that lie near phase boundaries are often of particular interest due to their high sensitivity to perturbations in their underlying spin-charge-orbital order parameters, which can lead to colossal changes in resistive and magnetic properties. $La_{1-x}Sr_xMnO_3$ (x = 0.6) (LSMO) is one such material. It has been shown in bulk samples to have a region of short range magnetic ordering (i.e., a deviation from Curie-Weiss behavior) between 320K and 210K and to straddle a canted AFM/A-type AFM phase boundary below 200K[22]. Surprisingly, this material has not been synthesized in thin film form even though its complex phase behavior should make it highly sensitive to orbital populations controlled by epitaxy induced strain effects. While AMR in other perovskite manganites has been reported, the mechanism is typically still associated with FM phase coexistence or transition[135–138]. In this Letter, we investigate strain effects on the resistive and magnetic properties of (x = 0.6) doped LSMO films and find that differences in AFM ordering type can have a profound impact on the AMR magnitude and character.

Experiments were performed on 10nm LSMO films grown epitaxially on $SrTiO_3$ (STO), $(LaAlO_3)_{0.3}(Sr_2AlTaO_8)_{0.7}$ (LSAT), and $LaAlO_3$ (LAO) substrates using pulsed laser deposition. Growth was performed in an ultrahigh vacuum system with a base pressure of $< 1 \times 10^{-10}$ Torr. Substrates were held at 760°C in a flowing O_2 environment at 0.5 mTorr. A 248nm pulsed KrF excimer laser was operated at 1Hz and 0.8 J/cm^2 fluence to give an average deposition rate of 0.1Å/s. Reflection high-energy electron diffraction (RHEED) was used to monitor surfaces during growth and conformed to a layer-by-layer growth mode. After growth, samples were post annealed at 700°C in 1atm flowing O_2 for 2h. *in situ* RHEED and *ex*

situ atomic force microscopy confirmed flat, single phase surface morphologies. X-ray measurements were carried out on a PanAlytical XPert thin film diffractometer with Cu Kα radiation. X-ray linear dichroism (XLD) measurements were conducted at beamline 4.0.2 at the Advanced Light Source in total electron yield mode by monitoring the sample drain current. The linearly polarized x-rays were incident upon the sample with a 60° angle relative to the sample normal and the $\boldsymbol{E}$ vector was oriented parallel or perpendicular to the scattering plane. Transport measurements were taken in a Quantum Design Physical Properties Measurement System (PPMS) using Keithley 2400 source-measure electronics at lμA constant current in a 4-probe geometry. Magnetization measurements were conducted on a Quantum Design Magnetic Properties Measurement System (MPMS3) in DC scan mode.

Figure 15.1 shows the $\theta - 2\theta$ XRD data containing the $(0\ 0\ 2)_{\mathrm{pc}}$ LSMO and substrate peaks for each of the three substrates (where pc is pseudocubic). We observe that all films have grown in a uniform single phase (Figure 5.1 inset) and present thickness fringes correlating to 10nm thicknesses. Figure 5.1(b) gives reciprocal space maps taken through the (1 0 3)$mathrm_{pc}$ peak, which indicate that the 10 nm films are fully strained on each of the three substrates. In-plane a-b axes (out-of-plane c axis) lattice values are shown to be 3.906Å (3.79982Å± 0.00115) for STO, 3.872Å (3.83942Å± 0.00585) for LSAT, and 3.790Å (3.97381Å± 0.00769) for LAO. These dimensions are consistent with expected unit cell volumes for the x=0.6 doping[139]. From these values, we calculate c/a ratios of 0.9728±0.0003 for STO, 0.9916±0.0015 for LSAT, and 1.0485±0.0020 for LAO. The offset from c/a=1 is a known indicator of orbital state preference where modulation of the e_g electrons orbital occupancy with tensile strain (c/a < 1) promoting in-plane $x^2 - y^2$ filling, and compressive strain (c/a > 1) promoting out-of-plane $3z^2 - r^2$ filling[15, 140]. We performed x-ray linear dichroism measurements on the LSAT and LAO samples (Fig. 5.1). Integrating the area under the L_2 peak has been shown to be an important indicator of orbital occupancy preference[15]. Here, the compressively strained LAO sample (c/a > 1) has a positive integrated value of 0.12 indicating a $3z^2 - r^2$ preference. The nominally

lattice matched LSAT sample is very slightly tensile strained and has a negative integrated value of 0.03 which indicates a weak $x^2 - y^2$ preference. The more strongly tensile strained STO sample is expected to continue this trend and possess a stronger $x^2 - y^2$ preference due to its relatively smaller c/a value.

Figure 5.2 show the resistive properties of the LSMO films from 400K to 10K and demonstrate a strong sensitivity to applied strain. Here, resistivity loops from 400K $\rightarrow$ 10K $\rightarrow$ 400K were taken at 3K/min with magnetic field along the out-of-plane direction. In each case, distinct transitions are observed; however, the number and onset temperatures vary while no hysteresis is observed. Compressive strain (on LAO) induces three distinct insulating regions. Between 70K and 400K, little difference is observed in the insulating behavior. Below 200K, the magnetoresistance (MR), defined as $MR = [(R_0 - R_H)/R_H] \times 100\%$, where R_H and R_0 are, respectively, the resistances under field=H and 0, has a weak temperature dependence (Fig. 5.2), which then increases sharply below 70K. Since the sample resistance exceeded measurable ranges below 60K, the absolute MR at low temperatures may be much higher than the 40% value shown. The nominally matched LSAT sample shows four insulating regions below 400K, while presenting the strongest MR response with a maximum of 140% at 10K. It is worth noting that unlike other manganite compositions exhibiting colossal magnetoresistance in which MR presents itself in a relatively narrow temperature region, the lattice matched LSMO film exhibits $> 20\%$ MR from 240K to 10K[37, 141]. The tensile strained film grown on STO is the only system that displays a metal-insulator transition, T_{MIT} 280K, while a reentrant insulator behavior occurs below 120K. We also observe that tensile strain acts to suppress MR across all temperatures with a small peak near T_{MIT} and a sharp upturn below 100K. A comparison of behaviors suggests that the unstrained film may be comprised of mixed phases, as strong MR is known to be one signature[37]. The relatively weak MR and vastly different resistive behaviors present in the tensile and compressive states at low temperatures may indicate that their preferential orbital occupations drive different but more homogeneous orderings. Since different ordering

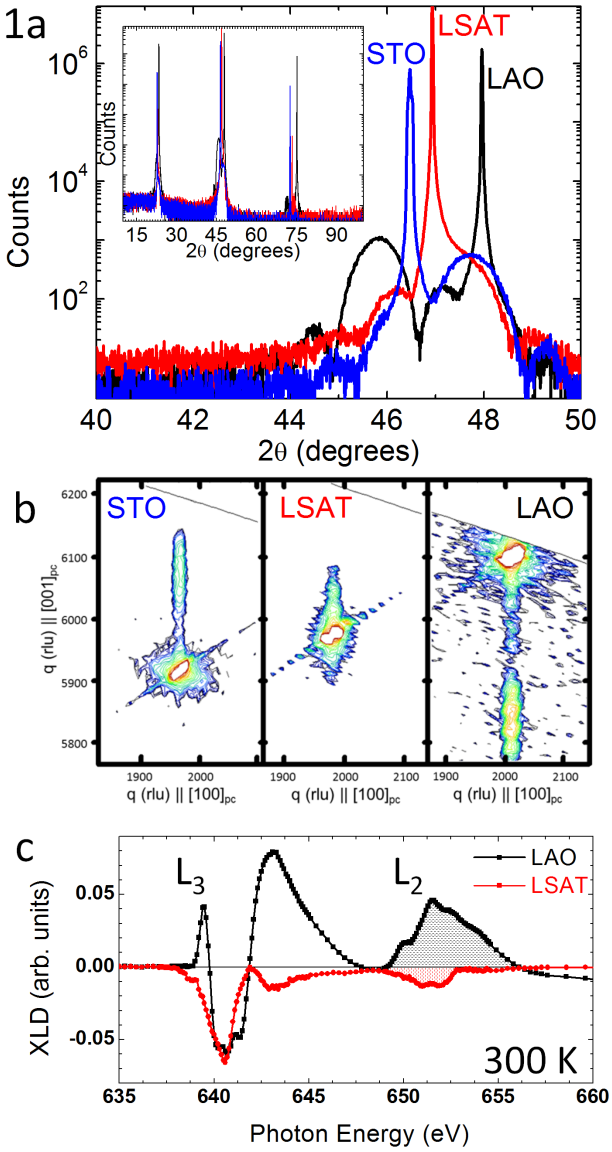

Figure 5.1: (a) $\theta - 2\theta$ XRD scans around the (0 0 2)$mathrm_{pc}$ peak of 10nm thick LSMO films grown on different substrates. Inset shows longer range XRD results and present no spurious phases. (b) Reciprocal-space maps taken through the (1 0 3)$mathrm_{pc}$ peak to demonstrate that LSMO films are commensurate with underlying substrates. (c) XLD spectra taken at 300K on films on LAO and LSAT substrates. Integration of L_2 peaks, denoted by thatched regions, show an orbital preference dependent on c/a values where compressive strain gives preference to $3z^2$-r^2 and weak tensile strain gives a slight preference for x^2-y^2 orbital occupation from [128]

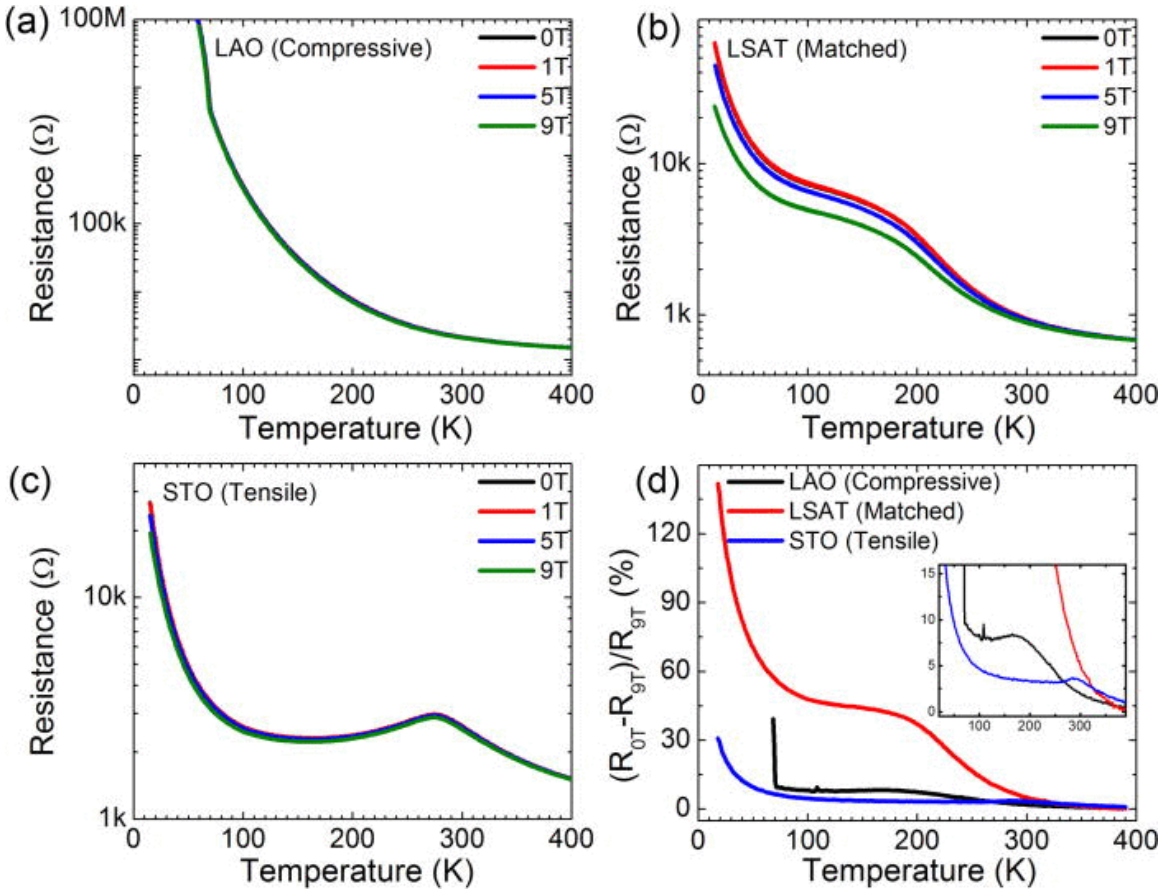

Figure 5.2: Resistance as a function of temperature loops under increasing out-of-plane magnetic fields for (a) compressively strained film on LAO, (b) lattice matched film on LSAT, and (c) tensile strained film on STO. (d) MR at 9T for each of the three films from [128]

types are known to have varying sensitivity to magnetic field direction, we investigate the effects of field direction on resistivity for each of the samples.

Angular dependences of the resistivity under 9T magnetic fields for the LSMO samples are given in Figure 5.3 The samples were field cooled under 9T with $\theta = 0°$ and rotation scans taken in order from the highest temperature to the lowest. Here, $\theta = 0°$ denotes the magnetic field, H, perpendicular to the current direction, J, and the sample surface, while $\theta = 90°$ corresponds to H parallel to J in the film plane. AMR can then be taken as $[(R_\theta - R_0)/R_\theta] \times 100\%$, where R_θ and R_0 are the resistances at θ and θ=0, respectively. Under compressive strain, there is a strong response to

field direction, which presents as a 2-fold symmetric curve similar to the shape and amplitude of the highest reported AMR values in ferromagnetic based manganite devices and following the same $\cos^2(\theta)$ dependence[137, 142]. Values range from 5% at 200K to 63% at 60K with maxima occurring when the magnetic field is perpendicular to the film. The sharp jump in AMR from 75K to 60K suggests that these percentages might be much higher at lower temperatures, but we are unable to measure due to the high resistances. The lattice matched LSAT sample also shows 2-fold symmetric behavior at high temperature, but a resistive plateau of several degrees around field perpendicular begins to present itself at 100K that breaks the $\cos^2(\theta)$ dependence shown in the compressively strained case. The AMR values range from 1% at 150K to 8% at 10K with the biggest jump in response occurring between 100K and 50K. The differences between AMR in the tensile and lattice matched samples is interesting, as the absolute MR is considerably higher in the lattice matched sample, while the compressively strained sample is much more sensitive to field direction. Tensile strain in the STO sample nearly extinguishes the AMR response with values on the order of 0.1% at all temperatures below 300K. However, at 100K, 50K, and 10K, we observe an intriguing response characterized by sharp increases in resistance occurring near magnetic field perpendicular to film surface. The angular position of the peaks increases slowly with decreasing temperature (i.e., $\pm 7^\circ$ at 100 K, $\pm 15^\circ$ at 50 K, and $\pm 17^\circ$ at 10 K), while the minima occur at $\pm 90^\circ$ for all temperatures. This behavior is not consistent with any previous explanations involving phase coexistence or substrate miscut induced anisotropy[135, 136, 138, 143]. Also, the relatively high 9T magnetic field should be more than sufficient to overcome inherent magnetic anisotropy arising from non-uniform mesoscale distribution of strain caused by STO twinning effects[144, 145]. STO twinning can be further ruled out as the cause by the fact that the observed effect changes with decreases temperature well below the STO phase transition. Instead, as we suggest below, these peaks may be the result of electron scattering from a canted AFM phase.

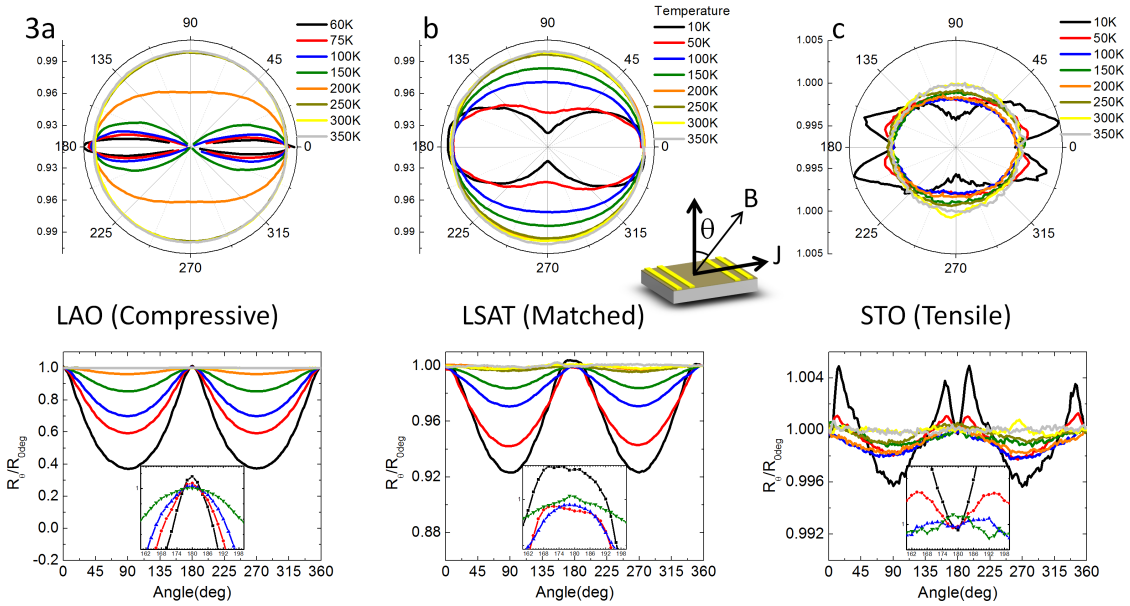

Figure 5.3: Angular dependent AMR with H=9T, the inset shows the measurement geometry where θ is the angle between H and J for (a) compressively strained film on LAO, (b) lattice matched film on LSAT, and (c) tensile strained film on STO. Insets show regions $\pm 20°$ around field perpendicular to highlight anomalous low angle AMR behavior from [128]

Figure 5.4 presents field cooled (FC) and zero field cooled (ZFC) magnetization data under a 30mT field for each of the samples. The substrate induced diamagnetic background has been subtracted from each set of data; however in each case there is still an upturn in magnetization below 50K that may be caused by substrate induced paramagnetic onset. Since we cannot say with certainty what causes these upturn, we will restrict our discussion to temperatures above this region. None of the samples show a clear ferromagnetic onset and all present a weak total magnetization across the entire temperature range. Without a FM transition, we can rule out PM to FM transitions as the instigator of the magnetoresistive responses which is a common avenue for strong MR and AMR in manganites[138]. The compressively strained LAO sample shows a weak signature of magnetic ordering below 200K. This temperature corresponds to the bump in MR% and the onset of strong AMR. However, there is no change in magnetic behavior corresponding to the sharp increase in resistivity below

70K. This may signal a freezing out of the conduction along the $3z^2 - r^2$ dominated superexchange channel. The nominally matched LSAT sample shows a slight decrease in magnetization from 350K to 300K which may indicate a transition away from a high temperature paramagnetic phase similar to what is reported in bulk samples[22]. This transition also coincides with an increase in resistivity and MR% in transport measurements. We observe a weak ordering signature slightly below 200K which again coincides with a large jump in AMR. The tensile strained STO sample shows an increase in magnetization from 350K to 310K on FC that coincides with the metal-insulator transition seen in resistivity; however magnetization vs field loops show no indication of ferromagnetism (not shown). When combined with the fact that this magnetic transition is not seen in the ZFC data and that there is a change in MR near 300K, a region of mixed phases or short range ordering can be assumed between 310K and 120K[30]. At 120K, the strongest magnetic ordering signature of the three strain states appears. It is important to note that this temperature is above the STO cubic-tetragonal phase transition at 105K so we can conclude that the observed magnetic ordering is not the result of a substrate transition. Further, the unusual AMR responses of hard axis peaks at ± several degrees to perpendicular magnetic field application occur below 100K which is well within the ordered window. This is within the temperature range where a magnetically ordered canted AFM phase is known to reside in bulk, so we speculate that these resistive peaks at set angles may be the result of scattering from the ordered spin canted sites. We also note that the magnetoresistive behavior appears to conform to a spin-flop type of response for all three strain states; as neither out-of-plane ± 9T magnetic field dependent resistivity loops nor ± 7T magnetic field dependent magnetization loops (data not shown) present the typical sharp discontinuities that signal a spin-flip transition seen in other AFM manganites[146, 147]. Figure 5.5 presents low field AMR scans taken at 2T for the compressively strained sample and 3T for the matched and tensile strained samples at 60K and 10K, respectively, and were nearly identical to the 9T AMR angular response curves but with lower absolute MR response magnitude which

suggests that the AFM ground state has not been melted in any of the samples even at the highest field.

It is known that magnetic degrees of freedom can be indirectly controlled by tuning orbital degrees of freedom and has been shown theoretically that for the $La_{1-x}Sr_xMnO_3$ system slight variations around $c/a = 1$ at x=0.6 could lead to different magnetic ground states[148]. Specifically, $c/a < 1$, where $x^2 - y^2$ orbital occupation dominates, leads to an A-type AFM phase; and $c/a > 1$, where $3z^2 - r^2$ orbital occupation dominates, leads to a C-type AFM phase[149, 150]. This is consistent with our results where compressive strain arising from the LAO substrate has a $c/a = 1.049$, while the nominally lattice matched LSAT sample and tensile strained STO sample have c/a values of 0.992 and 0.973, respectively. Thus, the large differences in AMR values may be the result of these different ordering types where the coupling between orbital occupation and spin ordering dominates behavior. AMR in AFM materials has been predicted and experimentally confirmed; but only in tunnel junctions[27, 130] and at much lower AMR values in simple ohmic devices[131, 132] than what we observe in the compressively strained and near lattice matched x=0.6 LSMO films. The strong field orientation results suggest that this material would be a good candidate for tunnel junction devices where spin coupling across the interface may give unprecedented response. Future studies are needed to identify the exact magnetic ordering types induced by the different strain states and whether mixed electronic phases may play a role. These studies suggest that complex oxides may find use in harnessing AMR for AFM spintronic applications.

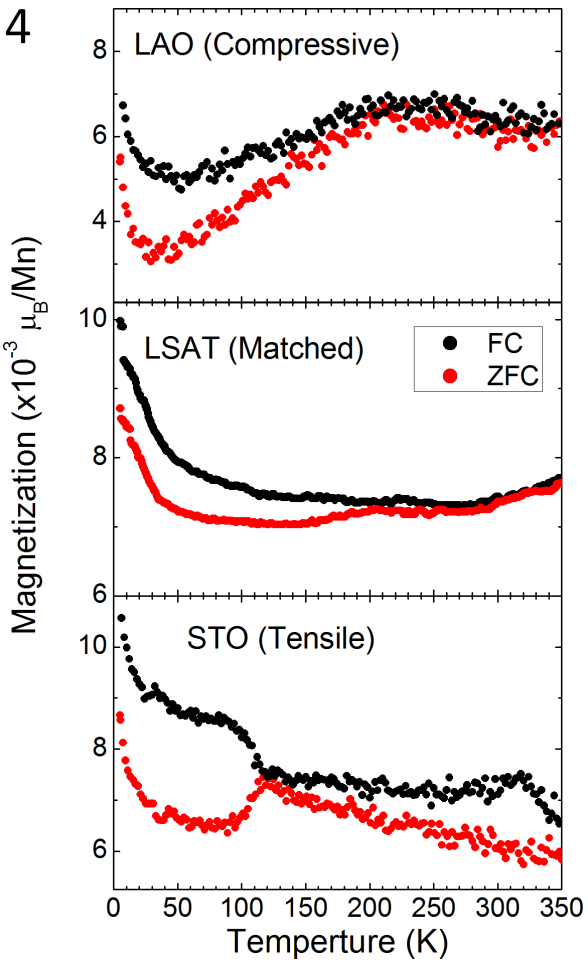

Figure 5.4: FC and ZFC magnetization values under a 30mT magnetic field from 5K to 350K show signatures of magnetic ordering from [128]

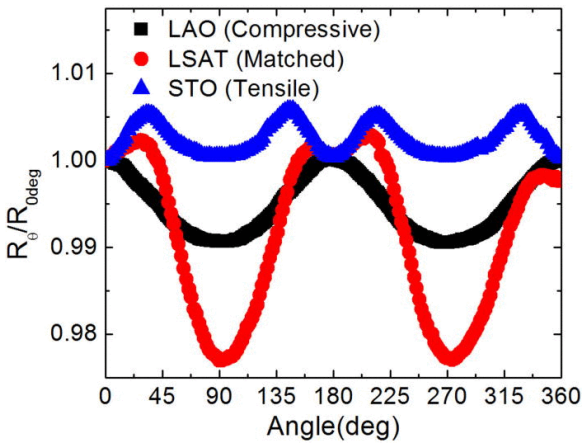

Figure 5.5: Low field angular dependent AMR for LSAT and STO at 10K under a 3T magnetic field and for LAO at 60K under a 2T magnetic field from [128]

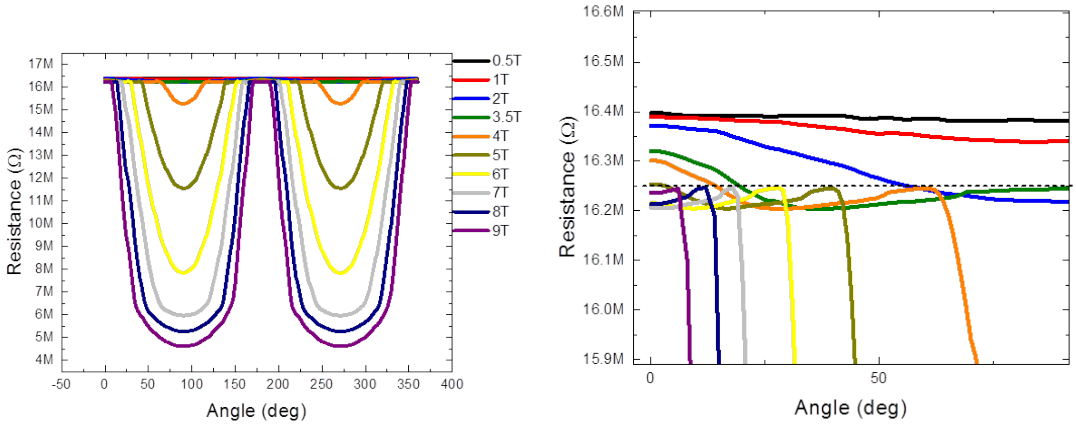

(a) 4-Wire AMR vs. H of $La_{0.4}Sr_{0.6}MnO_3$

(b) 4-Wire AMR vs. H of $La_{0.4}Sr_{0.6}MnO_3$ Zoomed-in View

Figure 5.6: (a) 4-wire anisotropic magnetoresistance measurements of $La_{0.4}Sr_{0.6}MnO_3$ crystal system, done on 10nm thick films at 60K. (b) A zoomed in view of the angle dependence occuring near 16.25MΩ resistance.

5.3 Unpublished studies on $La_{0.4}Sr_{0.6}MnO_3$ anisotropic magnetoresistance

Further investigation of these materials demonstrated what appeared initially to be a never before seen angle dependent anisotropic magnetoresistance. This data befuddled us for a long time, and should be used as a precautionary tale for high resistance measurements. The biggest issue in modeling this data came from the perceived angle dependent drop in resistance that occurs at changing angles with increasing magnetic fields. Upon further inspection these dramatic decreases in resistance occurred at similar voltages shown as a resistance value as all of these samples were measured at the same applied current (highlighted in figure 5.6. This prompted a look into the instrumentation of the measurement to ensure the property is real. Multiple repetitions of this measurement showed the same effects which were 4-fold symmetric angle dependent magnetoresistance.

When 2-wire measurements were conducted, suddenly the angle dependence of the measurements disappeared. The normalized value comparison between the 2-wire and 4-wire measurements are shown in figure 5.7 demonstrating the difference that can be seen between 2-wire and 4-wire measurements. This is a slightly surprising effect, particularly in it's consistency as the common differences between 2-wire and 4-wire measurements are seen in low resistance materials, not high resistance materials. In low resistance materials, the contacts to the sample have an interfacial resistance or contact resistance which can be dominant in the transport properties of low ($< 1k\Omega$) resistance samples. By applying the drive current from 2 leads, and measuring the voltage drop across the other 2 leads, this contact resistance can be eliminated from the measurement. However in high resistance measurements, while 4-wire measurements are not necessary, typically they do not create instrumental error, and therefore nearly all of our electrical measurements had used a 4-wire geometry, when the sample space was large enough. Finding the cause of this error is not completely clear, however it appears to be related to the voltage drop that occurs between the source and measure electrodes in the 4-wire setup. When this voltage becomes too large, the internal circuits of the source meter throttle the applied current with respect to the read voltage. The consistency at which this effect occurred in this sample is remarkable - and enough to trick even experienced transport experts.

Despite these difficulties, and the absence of some dramatic angle dependent anisotorpic magneto-resistance, the $La_{0.4}Sr_{0.6}MnO_3$ crystal system remains of great interest due to the extraordinarily high, unprecedented ansiotropic magnetoresistance particularly for an antiferromagnet with values approaching 70%.

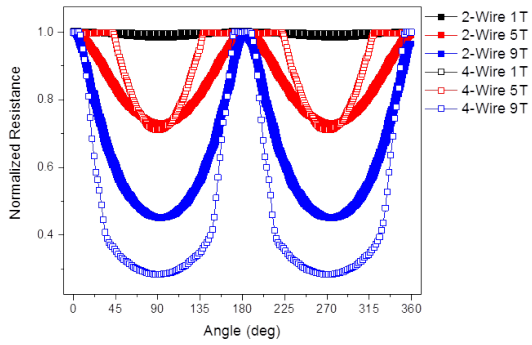

(a) 2 and 4-Wire AMR Comparison

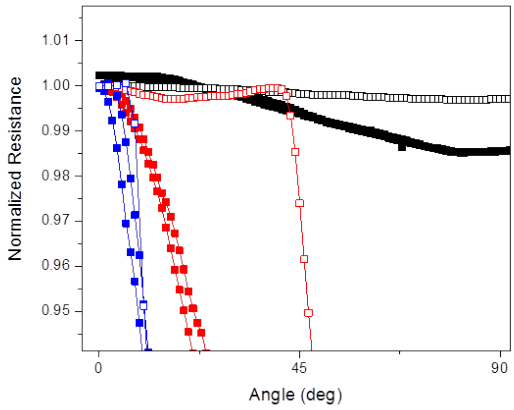

(b) 2 and 4-Wire AMR Comparison Zoomed-in View – 2 and 4-wire measurements

Figure 5.7: (a)Normalized AMR comparison between $La_{0.4}Sr_{0.6}MnO_3$ 2-wire and 4-wire measurements. The filled in symbols are the 2-wire measurements, while the open symbols are the 4-wire measurements. (b)A zoomed in view of the angle dependent error driven effect as compared to the 2-wire measurement effect which shows a standard $Cos^2(\theta)$ behavior for anisotropic magnetoresistance.

Chapter 6

Discussion and Conclusions

This dissertation presents novel work that evaluates combining the unique properties of complex transition metal oxide films, and room temperature ionic liquids. The interface between these two materials opens a door to manipulating material properties, and stoichiometry due to the immense electric fields that are generated in the formation of the electric double layer. Electric fields generated in this fashion can be used to apply electrostatic material changes, such as those found in traditional field effect transistors, however these fields are also strong enough to induce ionic changes within the systems such as oxygen mobility in amorphous, and crystalline films.

The details in creating electric double layer transistors is something that had not previously been evaluated, particularly when it comes to the geometric layout of the components of standard EDLT devices. We designed various devices in multiple geometries in order to probe the effects that arise from the spacing between the coplanar side gate and the active channel of the device, the shape of the gate and the active channel, and the relative sizes between the gate and the active channel. This study demonstrates the large impact that comes from the relative size between the coplanar side gate, and the active channel, and the negligible effect caused by the

separation distance and the shapes of the device components. This work should be useful in future design of electronic double layer devices with solid films.

Ferroelectric materials have been studied extensively in recent decades, especially in their possible uses in applications because of their remnant switchable charge polarization at material surfaces. The ability to switch large areas however is currently unavailable and the material lifetimes can be relatively low, especially at low frequency switching. Through interfacing these materials with ionic liquids we demonstrate the ability to switch large areas - entire thin films - while providing stability in low frequency switching.

Oxygen stoichiometry induced topotactic phase transitions are a promising method of creating multiple resistance electronics. $SrCoO_{3-\delta}$ is an exceptionally interesting material for these as it has a near room temperature paramagnetic to ferromagnetic transition that occurs in conjunction with its resistivity change and crystal transition as it moves between the brownmillerite phase that occurs at oxygen stoichiometry $SrCoO_{2.5}$ and the perovskite phase at oxygen stoichiometry $SrCoO_3$. Using the electrical energy provided by the extremely high electric fields generated with ionic liquid electric double layer the thermal energy load required is reduced to a room temperature range. Combining the room temperature magnetic and electronic properties with the possibility of room temperature, reversible topotactic phase transitions makes this combination very exciting for future applications.

With the fields of ionic liquids and thin film physics only recently coming together within the past decade, the future work in examining these interfaces is virtually endless. These work include combinations of theoretical and experimental work that can be used to determine the interfacial dynamics of ionic liquids, including absolute charges applied at local areas, and ion mobility within the liquids. Questions such as what is the ordering depth of electric double layers, what at what frequency can electric double layers be switched will prove valuable for moving ionic liquids beyond a clever manipulation technique and into device applications.

Only a small percentage of possible ionic liquids have been evaluated, and there is no doubt that more unique properties will be discovered as different ionic liquids are studied. Some new ionic liquids that could find rapid uses and implementations include liquids that have magnetic ions like [$FeCl_4$], dysprosium(III) compund [$Dy(SCN)_{8-x}(H_2O_x$], and others that have yet to be discovered[151–153]. Determining the magnetic ordering of these types of liquids, and how that relates to the electronic components of the ionic liquids could lead to revolutionary methods of electronic and magnetic control. Liquids with multiple charge centers also provide intriguing possibilities, considering how those charge centers could affect double layer formations or interfacial charge densities.

Ionic species control is another interesting field requiring further study. With the well known oxygen ion control through ionic liquid interfacing - between the $SrCoO_{3-\delta}$ work presented here in addition to many works done on other systems[73, 74, 125, 126] and the intercalation of lithium into layered materials like graphene or transition metal dichalcogenides[79, 154, 155] - the question remains to be seen if this type of control can be translated to other anionic species like sulfides or other, larger metallic cations like beryllium or sodium. Studies like these could lead to mixed anion crystals or metal doped layered materials, which could each yield incredible results.

The solid materials that can be probed can also be expanded. With the large area capabilities of ionic liquids, and the static charges on metallic surfaces, the gating effects can be applied to a wide range of new materials that were not previously possible. In combining advanced materials with ionic liquids the possibilities are endless, and this work simply scratches the surface of what appears to be a emerging field of advanced physics and interfacial material correlations.

Bibliography

[1] John Bardeen and Walter Hauser Brattain. The transistor, a semi-conductor triode. *Physical Review*, 74(2):230, 1948. 1

[2] R. K. Cavin, P. Lugli, and V. V. Zhirnov. Science and Engineering Beyond Moore's Law. *Proceedings of the IEEE*, 100(Special Centennial Issue):1720–1749, May 2012. 1, 2

[3] W. Haensch, E. J. Nowak, R. H. Dennard, P. M. Solomon, A. Bryant, O. H. Dokumaci, A. Kumar, X. Wang, J. B. Johnson, and M. V. Fischetti. Silicon CMOS devices beyond scaling. *IBM Journal of Research and Development*, 50(4.5):339–361, July 2006. 1

[4] G. E. Moore. Cramming more components onto integrated circuits, Reprinted from Electronics, volume 38, number 8, April 19, 1965, pp.114 ff. *IEEE Solid-State Circuits Society Newsletter*, 11(5):33–35, September 2006. 1

[5] G. E. Moore. Progress in digital integrated electronics [Technical literaiture, Copyright 1975 IEEE. Reprinted, with permission. Technical Digest. International Electron Devices Meeting, IEEE, 1975, pp. 11-13.]. *IEEE Solid-State Circuits Society Newsletter*, 20(3):36–37, September 2006. 1

[6] Andreas Herklotz, Hangwen Guo, Anthony T Wong, Ho Nyung Lee, Philip D Rack, and Thomas Z Ward. Multimodal Responses of SelfOrganized Circuitry in Electronically Phase Separated Materials. *Advanced Electronic Materials*, 2(9), 2016. 2

[7] J. Mannhart and D. G. Schlom. Oxide InterfacesAn Opportunity for Electronics. *Science*, 327(5973):1607–1611, March 2010. 2

[8] Y. Tokura and N. Nagaosa. Orbital Physics in Transition-Metal Oxides. *Science*, 288(5465):462–468, April 2000. 3, 4, 5, 6, 16, 17, 19

[9] D. I. Khomskii and G. A. Sawatzky. Interplay between spin, charge and orbital degrees of freedom in magnetic oxides. *Solid state communications*, 102(2-3):87–99, 1997. 4

[10] Hanns-Ulrich Habermeier. Thin films of perovskite-type complex oxides. *Materials Today*, 10(10):34–43, October 2007.

[11] Elbio Dagotto. Complexity in Strongly Correlated Electronic Systems. *Science*, 309(5732):257–262, July 2005. 4, 5, 17

[12] Pu Yu, Ying-Hao Chu, and Ramamoorthy Ramesh. Oxide interfaces: pathways to novel phenomena. *Materials Today*, 15(78):320–327, July 2012. 5, 19

[13] A. Vailionis, H. Boschker, W. Siemons, E. P. Houwman, D. H. A. Blank, G. Rijnders, and G. Koster. Misfit strain accommodation in epitaxial $AB{\mathrm{O}}_{3}$ perovskites: Lattice rotations and lattice modulations. *Physical Review B*, 83(6):064101, February 2011. 5, 7

[14] S. J. May, J.-W. Kim, J. M. Rondinelli, E. Karapetrova, N. A. Spaldin, A. Bhattacharya, and P. J. Ryan. Quantifying octahedral rotations in strained perovskite oxide films. *Physical Review B*, 82(1):014110, July 2010.

[15] D. Pesquera, G. Herranz, A. Barla, E. Pellegrin, F. Bondino, E. Magnano, F. Snchez, and J. Fontcuberta. Surface symmetry-breaking and strain effects on orbital occupancy in transition metal perovskite epitaxial films. *Nature Communications*, 3:1189, November 2012. 5, 96

[16] C. Merckling, M. El-Kazzi, G. Delhaye, V. Favre-Nicolin, Y. Robach, M. Gendry, G. Grenet, G. Saint-Girons, and G. Hollinger. Strain relaxation and critical thickness for epitaxial LaAlO3 thin films grown on SrTiO3(0 0 1) substrates by molecular beam epitaxy. *Journal of Crystal Growth*, 306(1):47–51, August 2007. 6

[17] J. D. Baran, M. Molinari, N. Kulwongwit, F. Azough, R. Freer, D. Kepaptsoglou, Q. M. Ramasse, and S. C. Parker. Tuning Thermoelectric Properties of Misfit Layered Cobaltites by Chemically Induced Strain. *The Journal of Physical Chemistry C*, 119(38):21818–21827, September 2015. 7

[18] Hangwen Guo, Shuai Dong, Philip D Rack, John D Budai, Christianne Beekman, Zheng Gai, Wolter Siemons, CM Gonzalez, R Timilsina, and Anthony T Wong. Strain Doping: Reversible Single-Axis Control of a Complex Oxide Lattice via Helium Implantation. *Physical review letters*, 114(25):256801, 2015. 8

[19] Andreas Herklotz, AT Wong, T Meyer, MD Biegalski, HN Lee, and TZ Ward. Controlling octahedral rotations in a perovskite via strain doping. *Scientific reports*, 6, 2016. 8

[20] Andreas Herklotz, Stefania Florina Rus, and Thomas Zac Ward. Continuously Controlled Optical Band Gap in Oxide Semiconductor Thin Films. *Nano Letters*, 16(3):1782–1786, March 2016. 8

[21] Charles Kittel. *Introduction to Solid State Physics*. Wiley, 8th edition, 2005. 9, 11, 15, 16, 18

[22] J. Hemberger, A. Krimmel, T. Kurz, H.-A. Krug von Nidda, V. Yu. Ivanov, A. A. Mukhin, A. M. Balbashov, and A. Loidl. Structural,

magnetic, and electrical properties of single-crystalline ${\mathrm{La}}_{1-x}{\mathrm{Sr}}_{x}{\mathrm{MnO}}_{3}$ $(0.4<x<0.85)$. *Physical Review B*, 66(9):094410, September 2002. 9, 10, 17, 95, 102

[23] F. Keffer and H. Chow. Dynamics of the Antiferromagnetic Spin-Flop Transition. *Physical Review Letters*, 31(17):1061–1063, October 1973. 11

[24] Alexander V. Khaetskii and Yuli V. Nazarov. Spin-flip transitions between Zeeman sublevels in semiconductor quantum dots. *Physical Review B*, 64(12):125316, September 2001. 11

[25] E. F. Kneller and R. Hawig. The exchange-spring magnet: a new material principle for permanent magnets. *IEEE Transactions on Magnetics*, 27(4):3588–3560, July 1991. 12

[26] Eric E. Fullerton, J. S. Jiang, M. Grimsditch, C. H. Sowers, and S. D. Bader. Exchange-spring behavior in epitaxial hard/soft magnetic bilayers. *Physical Review B*, 58(18):12193, 1998. 12

[27] B. G. Park, J. Wunderlich, X. Mart, V. Hol, Y. Kurosaki, M. Yamada, H. Yamamoto, A. Nishide, J. Hayakawa, H. Takahashi, A. B. Shick, and T. Jungwirth. A spin-valve-like magnetoresistance of an antiferromagnet-based tunnel junction. *Nature Materials*, 10(5):347–351, May 2011. 12, 94, 103

[28] M. D. Stiles and A. Zangwill. Anatomy of spin-transfer torque. *Physical Review B*, 66(1), June 2002. 12

[29] Maxim Tsoi. Magnetic tunnel junctions: Spin-torque measured up. *Nature Physics*, 4(1):17–18, January 2008. 12, 13

[30] T. Z. Ward, Z. Gai, X. Y. Xu, H. W. Guo, L. F. Yin, and J. Shen. Tuning the Metal-Insulator Transition in Manganite Films through Surface Exchange Coupling with Magnetic Nanodots. *Physical Review Letters*, 106(15):157207, April 2011. 13, 14, 95, 102

[31] Hangwen Guo, Joo H. Noh, Shuai Dong, Philip D. Rack, Zheng Gai, Xiaoshan Xu, Elbio Dagotto, Jian Shen, and T. Zac Ward. Electrophoretic-like Gating Used To Control MetalInsulator Transitions in Electronically Phase Separated Manganite Wires. *Nano Letters*, 13(8):3749–3754, August 2013. 15, 95

[32] T. Z. Ward, X. G. Zhang, L. F. Yin, X. Q. Zhang, Ming Liu, P. C. Snijders, S. Jesse, E. W. Plummer, Z. H. Cheng, E. Dagotto, and J. Shen. Time-Resolved Electronic Phase Transitions in Manganites. *Physical Review Letters*, 102(8):087201, February 2009. 15

[33] Nevill Mott. On metal-insulator transitions. *Journal of Solid State Chemistry*, 88(1):5–7, 1990. 16

[34] N. F. Mott. Metal-insulator transition. *Reviews of Modern Physics*, 40(4):677, 1968.

[35] A. Zylbersztejn and Nevill Francis Mott. Metal-insulator transition in vanadium dioxide. *Physical Review B*, 11(11):4383, 1975. 16

[36] R Milligan and G Thomas. The Metal-Insulator Transition. *Annual Review of Physical Chemistry*, 36(1):139–158, 1985. 16

[37] Elbio Dagotto, Takashi Hotta, and Adriana Moreo. Colossal magnetoresistant materials: the key role of phase separation. *Physics Reports*, 344(13):1–153, April 2001. 17, 97

[38] Nirat Ray and Umesh V. Waghmare. Coupling between magnetic ordering and structural instabilities in perovskite biferroics: A first-principles study. *Physical Review B*, 77(13):134112, April 2008. 17

[39] J. F. Scott. Applications of Modern Ferroelectrics. *Science*, 315(5814):954–959, February 2007. 18, 66, 68

[40] Gene H. Haertling. Ferroelectric Ceramics: History and Technology. *Journal of the American Ceramic Society*, 82(4):797–818, April 1999. 65, 66

[41] P. Muralt. Ferroelectric thin films for micro-sensors and actuators: a review. *Journal of Micromechanics and Microengineering*, 10(2):136, 2000.

[42] N. Setter, D. Damjanovic, L. Eng, G. Fox, S. Gevorgian, S. Hong, A. Kingon, H. Kohlstedt, N. Y. Park, G. B. Stephenson, I. Stolitchnov, A. K. Taganstev, D. V. Taylor, T. Yamada, and S. Streiffer. Ferroelectric thin films: Review of materials, properties, and applications. *Journal of Applied Physics*, 100(5):051606, September 2006. 18, 65, 66, 70

[43] R. Ramesh and Nicola A. Spaldin. Multiferroics: progress and prospects in thin films. *Nature Materials*, 6(1):21–29, January 2007. 18, 19

[44] Sang-Wook Cheong and Maxim Mostovoy. Multiferroics: a magnetic twist for ferroelectricity. *Nature Materials*, 6(1):13–20, January 2007. 18, 19, 66

[45] Milton Ohring. *Materials Science of Thin Films: Deposition and Structure*. Academic Press, San Diego, second edition, 2002. 20, 21, 22, 24, 25, 26, 27, 28, 30, 31, 32, 33, 34, 35

[46] Steven M. George. Atomic Layer Deposition: An Overview. *Chemical Reviews*, 110(1):111–131, January 2010. 22

[47] C. Ratsch and A. Zangwill. Stepflow growth on strained surfaces. *Applied Physics Letters*, 63(17):2348–2350, October 1993. 29

[48] Thomas Ward. *Emergent Phenomena in Spatially Confined Manganites*. PhD thesis, University of Tennessee, 2008. 29

[49] Elsa Reichmanis and Larry F Thompson. Polymer materials for microlithography. *Chemical Reviews*, 89(6):1273–1289, 1989. 30

[50] MicroChem Corp. Positive vs. Negative Tone Photoresists, 2017. 32

[51] J. A. Christman, R. R. Woolcott, A. I. Kingon, and R. J. Nemanich. Piezoelectric measurements with atomic force microscopy. *Applied Physics Letters*, 73(26):3851–3853, December 1998. 34

[52] Christine Kranz. *Microscopic Techniques for the Characterization of Gold Nanoparticles (PDF Download Available)*. 2014. 37

[53] Rolf E. Hummel. *Electronic Properties of Materials*. Springer, New York, fourth edition, 2011. 38

[54] Ronald Chwang, B. J. Smith, and C. R. Crowell. Contact size effects on the van der Pauw method for resistivity and Hall coefficient measurement. *Solid-State Electronics*, 17(12):1217–1227, 1974. 38

[55] M Stewart and M. G. Cain. Ferroelectric Hysteresis Measurement and Analysis, 1999. 40, 41

[56] M. Sawicki, W. Stefanowicz, and A. Ney. Sensitive SQUID magnetometry for studying nanomagnetism. *Semiconductor Science and Technology*, 26(6):064006, 2011. 41

[57] Z. Q. Qiu and S. D. Bader. Surface magneto-optic Kerr effect. *Review of Scientific Instruments*, 71(3):1243–1255, March 2000. 42

[58] C. F. Majkrzak. Polarized neutron reflectometry. *Physica B: Condensed Matter*, 173(1-2):75–88, 1991. 42

[59] K. N Marsh, J. A Boxall, and R Lichtenthaler. Room temperature ionic liquids and their mixturesa review. *Fluid Phase Equilibria*, 219(1):93–98, May 2004. 42, 43

[60] Maxim V. Fedorov and Alexei A. Kornyshev. Towards understanding the structure and capacitance of electrical double layer in ionic liquids. *Electrochimica Acta*, 53(23):6835–6840, October 2008. 43, 44

[61] Maxim V. Fedorov and Alexei A. Kornyshev. Ionic Liquid Near a Charged Wall: Structure and Capacitance of Electrical Double Layer. *The Journal of Physical Chemistry B*, 112(38):11868–11872, September 2008. 42, 43, 44, 50

[62] Michel Armand, Frank Endres, Douglas R. MacFarlane, Hiroyuki Ohno, and Bruno Scrosati. Ionic-liquid materials for the electrochemical challenges of the future. *Nature Materials*, 8(8):621–629, August 2009. 43

[63] Jairton Dupont, Roberto F. de Souza, and Paulo A. Z. Suarez. Ionic Liquid (Molten Salt) Phase Organometallic Catalysis. *Chemical Reviews*, 102(10):3667–3692, October 2002. 43, 44

[64] Makoto Ue, Masayuki Takeda, Akiko Toriumi, Asao Kominato, Rika Hagiwara, and Yasuhiko Ito. Application of Low-Viscosity Ionic Liquid to the Electrolyte of Double-Layer Capacitors. *Journal of The Electrochemical Society*, 150(4):A499–A502, April 2003. 43

[65] Patrick Gallagher, Menyoung Lee, Trevor A. Petach, Sam W. Stanwyck, James R. Williams, Kenji Watanabe, Takashi Taniguchi, and David Goldhaber-Gordon. A high-mobility electronic system at an electrolyte-gated oxide surface. *Nature Communications*, 6:6437, March 2015. 44, 81

[66] K. Ueno, S. Nakamura, H. Shimotani, H. T. Yuan, N. Kimura, T. Nojima, H. Aoki, Y. Iwasa, and M. Kawasaki. Discovery of superconductivity in KTaO3 by electrostatic carrier doping. *Nature Nanotechnology*, 6(7):408–412, July 2011. 45, 49, 62, 65, 82

[67] Hongtao Yuan, Hidekazu Shimotani, Atsushi Tsukazaki, Akira Ohtomo, Masashi Kawasaki, and Yoshihiro Iwasa. High-Density Carrier Accumulation in

ZnO Field-Effect Transistors Gated by Electric Double Layers of Ionic Liquids. *Advanced Functional Materials*, 19(7):1046–1053, April 2009. 44, 81, 82

[68] Martin Z. Bazant, Brian D. Storey, and Alexei A. Kornyshev. Double Layer in Ionic Liquids: Overscreening versus Crowding. *Physical Review Letters*, 106(4):046102, January 2011. 44, 50

[69] Jennifer M. Black, Deron Walters, Aleksander Labuda, Guang Feng, Patrick C. Hillesheim, Sheng Dai, Peter T. Cummings, Sergei V. Kalinin, Roger Proksch, and Nina Balke. Bias-Dependent Molecular-Level Structure of Electrical Double Layer in Ionic Liquid on Graphite. *Nano Letters*, 13(12):5954–5960, December 2013. 44, 50, 59

[70] Daniele Braga, Ignacio Gutirrez Lezama, Helmuth Berger, and Alberto F. Morpurgo. Quantitative Determination of the Band Gap of WS2 with Ambipolar Ionic Liquid-Gated Transistors. *Nano Letters*, 12(10):5218–5223, October 2012. 45, 49, 50, 62, 65

[71] K. Ueno, S. Nakamura, H. Shimotani, A. Ohtomo, N. Kimura, T. Nojima, H. Aoki, Y. Iwasa, and M. Kawasaki. Electric-field-induced superconductivity in an insulator. *Nature Materials*, 7(11):855–858, November 2008.

[72] J. T. Ye, S. Inoue, K. Kobayashi, Y. Kasahara, H. T. Yuan, H. Shimotani, and Y. Iwasa. Liquid-gated interface superconductivity on an atomically flat film. *Nature Materials*, 9(2):125–128, February 2010. 45, 49, 50, 62, 65, 82

[73] Pushpa Raj Pudasaini, Joo Hyon Noh, Anthony T. Wong, Olga S. Ovchinnikova, Amanda V. Haglund, Sheng Dai, Thomas Zac Ward, David Mandrus, and Philip D. Rack. Ionic Liquid Activation of Amorphous Metal-Oxide Semiconductors for Flexible Transparent Electronic Devices. *Advanced Functional Materials*, pages n/a–n/a, February 2016. 45, 49, 51, 52, 57, 65, 110

[74] Jaewoo Jeong, Nagaphani Aetukuri, Tanja Graf, Thomas D. Schladt, Mahesh G. Samant, and Stuart S. P. Parkin. Suppression of Metal-Insulator Transition in VO2 by Electric FieldInduced Oxygen Vacancy Formation. *Science*, 339(6126):1402–1405, March 2013. 49, 50, 62, 65, 82, 89, 110

[75] Carlos ViolBarbosa, Julie Karel, Janos Kiss, Ovidiu-dorin Gordan, Simone G. Altendorf, Yuki Utsumi, Mahesh G. Samant, Yu-Han Wu, Ku-Ding Tsuei, Claudia Felser, and Stuart S. P. Parkin. Transparent conducting oxide induced by liquid electrolyte gating. *Proceedings of the National Academy of Sciences*, 113(40):11148–11151, October 2016. 45, 50, 62, 65, 82

[76] Qing Hua Wang, Kourosh Kalantar-Zadeh, Andras Kis, Jonathan N. Coleman, and Michael S. Strano. Electronics and optoelectronics of two-dimensional transition metal dichalcogenides. *Nature Nanotechnology*, 7(11):699–712, November 2012. 45, 50, 65

[77] Q. X. Liu, S. Zein El Abedin, and F. Endres. Electroplating of mild steel by aluminium in a first generation ionic liquid: A green alternative to commercial Al-plating in organic solvents. *Surface and Coatings Technology*, 201(34):1352–1356, October 2006.

[78] Peng Wang, Shaik M. Zakeeruddin, Pascal Comte, Ivan Exnar, and Michael Grtzel. Gelation of Ionic Liquid-Based Electrolytes with Silica Nanoparticles for Quasi-Solid-State Dye-Sensitized Solar Cells. *Journal of the American Chemical Society*, 125(5):1166–1167, February 2003.

[79] Giovanni B. Appetecchi, Maria Montanino, Andrea Balducci, Simon F. Lux, Martin Winterb, and Stefano Passerini. Lithium insertion in graphite from ternary ionic liquid-lithium salt electrolytes: I. Electrochemical characterization of the electrolytes. *Journal of Power Sources*, 192(2):599–605, July 2009. 110

[80] Alexey Izgorodin, Orawan Winther-Jensen, Bjorn Winther-Jensen, and Douglas R. MacFarlane. CdS thin-film electrodeposition from a phosphonium ionic liquid. *Physical Chemistry Chemical Physics*, 11(38):8532–8537, 2009. 45

[81] A. T. Wong, J. H. Noh, P. R. Pudasaini, B. Wolf, N. Balke, A. Herklotz, Y. Sharma, A. V. Haglund, S. Dai, D. Mandrus, P. D. Rack, and T. Z. Ward. Impact of gate geometry on ionic liquid gated ionotronic systems. *APL Materials*, 5(4):042501, April 2017. 47, 65, 67

[82] Jaewoo Jeong, Nagaphani B. Aetukuri, Donata Passarello, Steven D. Conradson, Mahesh G. Samant, and Stuart S. P. Parkin. Giant reversible, facet-dependent, structural changes in a correlated-electron insulator induced by ionic liquid gating. *Proceedings of the National Academy of Sciences*, 112(4):1013–1018, January 2015. 49, 50

[83] Guy Dubuis, Yizhak Yacoby, Hua Zhou, Xi He, Anthony T. Bollinger, Davor Pavuna, Ron Pindak, and Ivan Boovi. Oxygen Displacement in Cuprates under Ionic Liquid Field-Effect Gating. *Scientific Reports*, 6:32378, August 2016. 50, 82, 83

[84] Mingyang Li, Wei Han, Xin Jiang, Jaewoo Jeong, Mahesh G. Samant, and Stuart S. P. Parkin. Suppression of Ionic Liquid Gate-Induced Metallization of SrTiO3(001) by Oxygen. *Nano Letters*, 13(10):4675–4678, October 2013. 50

[85] Meeghage Madusanka Perera, Ming-Wei Lin, Hsun-Jen Chuang, Bhim Prasad Chamlagain, Chongyu Wang, Xuebin Tan, Mark Ming-Cheng Cheng, David Tomnek, and Zhixian Zhou. Improved Carrier Mobility in Few-Layer MoS2 Field-Effect Transistors with Ionic-Liquid Gating. *ACS Nano*, 7(5):4449–4458, May 2013. 49

[86] Pushpa Raj Pudasaini, Joo Hyon Noh, Anthony Wong, Amanda V. Haglund, Sheng Dai, Thomas Zac Ward, David Mandrus, and Philip D. Rack. Ionic

Liquid versus SiO2 Gated a-IGZO Thin Film Transistors: A Direct Comparison. *ECS Journal of Solid State Science and Technology*, 4(9):Q105–Q109, January 2015. 49, 50, 51, 52

[87] Priscilla Kailian Ang, Shuai Wang, Qiaoliang Bao, John T. L. Thong, and Kian Ping Loh. High-Throughput Synthesis of Graphene by IntercalationExfoliation of Graphite Oxide and Study of Ionic Screening in Graphene Transistor. *ACS Nano*, 3(11):3587–3594, November 2009. 49

[88] Zhuangchun Wu, Zhihong Chen, Xu Du, Jonathan M. Logan, Jennifer Sippel, Maria Nikolou, Katalin Kamaras, John R. Reynolds, David B. Tanner, Arthur F. Hebard, and Andrew G. Rinzler. Transparent, Conductive Carbon Nanotube Films. *Science*, 305(5688):1273–1276, August 2004. 50

[89] J. T. Ye, Y. J. Zhang, R. Akashi, M. S. Bahramy, R. Arita, and Y. Iwasa. Superconducting Dome in a Gate-Tuned Band Insulator. *Science*, 338(6111):1193–1196, November 2012. 49, 50

[90] Yijin Zhang, Jianting Ye, Yusuke Matsuhashi, and Yoshihiro Iwasa. Ambipolar MoS2 Thin Flake Transistors. *Nano Letters*, 12(3):1136–1140, March 2012. 50, 65

[91] Clayton J. Dahlman, Gabriel LeBlanc, Amy Bergerud, Corey Staller, Jacob Adair, and Delia J. Milliron. Electrochemically Induced Transformations of Vanadium Dioxide Nanocrystals. *Nano Letters*, 16(10):6021–6027, October 2016.

[92] Simone Fabiano, Xavier Crispin, and Magnus Berggren. Ferroelectric Polarization Induces Electric Double Layer Bistability in Electrolyte-Gated Field-Effect Transistors. *ACS Applied Materials & Interfaces*, 6(1):438–442, January 2014. 65, 66

[93] Se Hyun Kim, Kihyon Hong, Wei Xie, Keun Hyung Lee, Sipei Zhang, Timothy P. Lodge, and C. Daniel Frisbie. Electrolyte-Gated Transistors for Organic and Printed Electronics. *Advanced Materials*, 25(13):1822–1846, April 2013. 50

[94] Honggu Chun and Taek Dong Chung. Iontronics. *Annual Review of Analytical Chemistry*, 8(1):441–462, 2015. 50, 65

[95] Jacek Kos and Stanisaw Lamperski. Electric double layer in molten salts: Toward a more realistic model. *Electrochimica Acta*, 213:574–577, September 2016. 50, 59

[96] Seyeoul Kwon, Joo Hyon Noh, Jiyong Noh, and Philip D. Rack. Quantitative Calculation of Oxygen Incorporation in Sputtered IGZO Films and the Impact on Transistor Properties. *Journal of The Electrochemical Society*, 158(3):H289–H293, March 2011. 52

[97] Andreas Herklotz, Er-Jia Guo, Anthony T. Wong, Tricia L. Meyer, Sheng Dai, T. Zac Ward, Ho Nyung Lee, and Michael R. Fitzsimmons. Reversible Control of Interfacial Magnetism through Ionic-Liquid-Assisted Polarization Switching. *Nano Letters*, February 2017. 61

[98] Till Cremer, Manuela Killian, J. Michael Gottfried, Natalia Paape, Peter Wasserscheid, Florian Maier, and Hans-Peter Steinrck. Physical Vapor Deposition of [EMIM][Tf2n]: A New Approach to the Modification of Surface Properties with Ultrathin Ionic Liquid Films. *ChemPhysChem*, 9(15):2185–2190, October 2008. 65

[99] Henrik Toss, Negar Sani, Simone Fabiano, Daniel T. Simon, Robert Forchheimer, and Magnus Berggren. Polarization of ferroelectric films through electrolyte. *Journal of Physics: Condensed Matter*, 28(10):105901, 2016. 65

[100] T. Tybell, C. H. Ahn, and J.-M. Triscone. Ferroelectricity in thin perovskite films. *Applied Physics Letters*, 75(6):856, 1999. 65, 66, 68

[101] Ennio Fatuzzo. Theoretical Considerations on the Switching Transient in Ferroelectrics. *Physical Review*, 127(6):1999–2005, September 1962. 66

[102] Christopher T. Nelson, Peng Gao, Jacob R. Jokisaari, Colin Heikes, Carolina Adamo, Alexander Melville, Seung-Hyub Baek, Chad M. Folkman, Benjamin Winchester, Yijia Gu, Yuanming Liu, Kui Zhang, Enge Wang, Jiangyu Li, Long-Qing Chen, Chang-Beom Eom, Darrell G. Schlom, and Xiaoqing Pan. Domain Dynamics During Ferroelectric Switching. *Science*, 334(6058):968–971, November 2011. 66

[103] Anton V. Ievlev, Petro Maksymovych, Morgan Trassin, Jan Seidel, Ramamoorthy Ramesh, Sergei V. Kalinin, and Olga S. Ovchinnikova. Chemical State Evolution in Ferroelectric Films during Tip-Induced Polarization and Electroresistive Switching. *ACS Applied Materials & Interfaces*, 8(43):29588–29593, November 2016. 66

[104] C.-Y. Kuo, Z. Hu, J. C. Yang, S.-C. Liao, Y. L. Huang, R. K. Vasudevan, M. B. Okatan, S. Jesse, S. V. Kalinin, L. Li, H. J. Liu, C.-H. Lai, T. W. Pi, S. Agrestini, K. Chen, P. Ohresser, A. Tanaka, L. H. Tjeng, and Y. H. Chu. Single-domain multiferroic BiFeO3 films. *Nature Communications*, 7:12712, September 2016. 66

[105] David I. Woodward, Jesper Knudsen, and Ian M. Reaney. Review of crystal and domain structures in the ${\mathrm{PbZr}}_{x}{\mathrm{Ti}}_{1\ensuremath{-}x}{\mathrm{O}}_{3}$ solid solution. *Physical Review B*, 72(10):104110, September 2005. 66

[106] Chun-Lin Jia, Valanoor Nagarajan, Jia-Qing He, Lothar Houben, Tong Zhao, Ramamoorthy Ramesh, Knut Urban, and Rainer Waser. Unit-cell scale mapping of ferroelectricity and tetragonality in epitaxial ultrathin ferroelectric films. *Nature Materials*, 6(1):64–69, January 2007. 66, 68

[107] Lu Jiang, Woo Seok Choi, Hyoungjeen Jeen, Takeshi Egami, and Ho Nyung Lee. Strongly coupled phase transition in ferroelectric/correlated electron oxide heterostructures. *Applied Physics Letters*, 101(4):042902, July 2012. 66, 95

[108] Ho Nyung Lee, Serge M. Nakhmanson, Matthew F. Chisholm, Hans M. Christen, Karin M. Rabe, and David Vanderbilt. Suppressed Dependence of Polarization on Epitaxial Strain in Highly Polar Ferroelectrics. *Physical Review Letters*, 98(21):217602, May 2007. 68

[109] A. K. Tagantsev, I. Stolichnov, E. L. Colla, and N. Setter. Polarization fatigue in ferroelectric films: Basic experimental findings, phenomenological scenarios, and microscopic features. *Journal of Applied Physics*, 90(3):1387–1402, August 2001. 74

[110] Benjamin C. Lee, Engin Ipek, Onur Mutlu, and Doug Burger. Architecting phase change memory as a scalable dram alternative. In *ACM SIGARCH Computer Architecture News*, volume 37, pages 2–13. ACM, 2009. 81

[111] Bryan L. Jackson, Alvaro Padilla, Alex G. Schrott, Rohit S. Shenoy, Blent N. Kurdi, Chung H. Lam, Dharmendra S. Modha, Bipin Rajendran, Gregory S. Corrado, Matthew Breitwisch, Geoffrey W. Burr, Roger Cheek, Kailash Gopalakrishnan, Simone Raoux, and Charles T. Rettner. Nanoscale electronic synapses using phase change devices. *ACM Journal on Emerging Technologies in Computing Systems*, 9(2):1–20, May 2013.

[112] Matthias Wuttig. Phase-change materials: Towards a universal memory? *Nature Materials*, 4(4):265–266, April 2005. 81

[113] Woo Seok Choi, Hyoungjeen Jeen, Jun Hee Lee, S. S. Ambrose Seo, Valentino R. Cooper, Karin M. Rabe, and Ho Nyung Lee. Reversal of the Lattice Structure in ${\mathrm{SrCoO}}_{x}$ Epitaxial Thin Films Studied by Real-Time Optical Spectroscopy and First-Principles Calculations. *Physical Review Letters*, 111(9):097401, August 2013. 81

[114] H. Jeen, W. S. Choi, J. W. Freeland, H. Ohta, C. U. Jung, and H. N. Lee. Topotactic Phase Transformation of the Brownmillerite SrCoO2.5 to the Perovskite SrCoO3. *Advanced Materials*, 25(27):3651–3656, July 2013. 81

[115] Hyoungjeen Jeen, Zhonghe Bi, Woo Seok Choi, Matthew F. Chisholm, Craig A. Bridges, M. Parans Paranthaman, and Ho Nyung Lee. Orienting Oxygen Vacancies for Fast Catalytic Reaction. *Advanced Materials*, 25(44):6459–6463, November 2013.

[116] Hyoungjeen Jeen, Woo Seok Choi, Michael D. Biegalski, Chad M. Folkman, I.-Cheng Tung, Dillon D. Fong, John W. Freeland, Dongwon Shin, Hiromichi Ohta, Matthew F. Chisholm, and Ho Nyung Lee. Reversible redox reactions in an epitaxially stabilized SrCoOx oxygen sponge. *Nature Materials*, 12(11):1057–1063, November 2013. 81

[117] Qiyang Lu, Yan Chen, Hendrik Bluhm, and Bilge Yildiz. Electronic Structure Evolution of SrCoOx during Electrochemically Driven Phase Transition Probed by in Situ X-ray Spectroscopy. *The Journal of Physical Chemistry C*, 120(42):24148–24157, October 2016. 83

[118] Qiyang Lu and Bilge Yildiz. Voltage-Controlled Topotactic Phase Transition in Thin-Film SrCoO $_x$ Monitored by In Situ X-ray Diffraction. *Nano Letters*, 16(2):1186–1193, February 2016. 81

[119] Chandrima Mitra, Randy S. Fishman, Satoshi Okamoto, Ho Nyung Lee, and Fernando A. Reboredo. Ground-state and spin-wave dynamics in

Brownmillerite SrCoO 2.5 a combined hybrid functional and LSDA + U study. *Journal of Physics: Condensed Matter*, 26(3):036004, 2014.

[120] Chandrima Mitra, Tricia Meyer, Ho Nyung Lee, and Fernando A. Reboredo. Oxygen diffusion pathways in brownmillerite SrCoO2.5: Influence of structure and chemical potential. *The Journal of Chemical Physics*, 141(8):084710, August 2014.

[121] Hassan A. Tahini, Xin Tan, Udo Schwingenschlgl, and Sean C. Smith. Formation and Migration of Oxygen Vacancies in SrCoO3 and Their Effect on Oxygen Evolution Reactions. *ACS Catalysis*, 6(8):5565–5570, August 2016. 81

[122] M. James, D. Cassidy, K. F. Wilson, J. Horvat, and R. L. Withers. Oxygen vacancy ordering and magnetism in the rare earth stabilised perovskite form of SrCoO3. *Solid State Sciences*, 6(7):655–662, July 2004. 81

[123] T. Nagai, W. Ito, and T. Sakon. Relationship between cation substitution and stability of perovskite structure in SrCoO3-based mixed conductors. *Solid State Ionics*, 177(3940):3433–3444, January 2007.

[124] Octolia Togibasa Tambunan, Min Young Lee, Deok Hyeon Kim, Kadek Juliana Parwanta, and Chang Uk Jung. Phase transformation of the brownmillerite SrCoO2.5 thin film through alkaline water electrolysis. *Journal of the Korean Physical Society*, 64(12):1845–1848, June 2014. 81

[125] Raoul Scherwitzl, Pavlo Zubko, I. Gutierrez Lezama, Shimpei Ono, Alberto F. Morpurgo, Gustau Catalan, and Jean-Marc Triscone. Electric-Field Control of the Metal-Insulator Transition in Ultrathin NdNiO3 Films. *Advanced Materials*, 22(48):5517–5520, December 2010. 82, 110

[126] Donata Passarello, Simone G. Altendorf, Jaewoo Jeong, Mahesh G. Samant, and Stuart S. P. Parkin. Metallization of Epitaxial VO2 Films by Ionic Liquid

Gating through Initially Insulating TiO2 Layers. *Nano Letters*, 16(9):5475–5481, September 2016. 83, 110

[127] Thomas D. Schladt, Tanja Graf, Nagaphani B. Aetukuri, Mingyang Li, Andrea Fantini, Xin Jiang, Mahesh G. Samant, and Stuart S. P. Parkin. Crystal-Facet-Dependent Metallization in Electrolyte-Gated Rutile TiO2 Single Crystals. *ACS Nano*, 7(9):8074–8081, September 2013. 89

[128] Anthony T Wong, Christianne Beekman, Hangwen Guo, Wolter Siemons, Zheng Gai, Elke Arenholz, Yayoi Takamura, and Thomas Zac Ward. Strain driven anisotropic magnetoresistance in antiferromagnetic La0. 4sr0. 6mno3. *Applied Physics Letters*, 105(5):052401, 2014. 92, 98, 99, 101, 104

[129] Claude Chappert, Albert Fert, and Frdric Nguyen Van Dau. The emergence of spin electronics in data storage. *Nature Materials*, 6(11):813–823, November 2007. 94

[130] Y. Y. Wang, C. Song, B. Cui, G. Y. Wang, F. Zeng, and F. Pan. Room-Temperature Perpendicular Exchange Coupling and Tunneling Anisotropic Magnetoresistance in an Antiferromagnet-Based Tunnel Junction. *Physical Review Letters*, 109(13):137201, September 2012. 103

[131] A. B. Shick, S. Khmelevskyi, O. N. Mryasov, J. Wunderlich, and T. Jungwirth. Spin-orbit coupling induced anisotropy effects in bimetallic antiferromagnets: A route towards antiferromagnetic spintronics. *Physical Review B*, 81(21):212409, June 2010. 95, 103

[132] X. Marti, I. Fina, C. Frontera, Jian Liu, P. Wadley, Q. He, R. J. Paull, J. D. Clarkson, J. Kudrnovsk, I. Turek, J. Kune, D. Yi, J.-H. Chu, C. T. Nelson, L. You, E. Arenholz, S. Salahuddin, J. Fontcuberta, T. Jungwirth, and R. Ramesh. Room-temperature antiferromagnetic memory resistor. *Nature Materials*, 13(4):367–374, April 2014. 94, 95, 103

[133] M. J. Rozenberg, I. H. Inoue, and M. J. Snchez. Strong electron correlation effects in nonvolatile electronic memory devices. *Applied Physics Letters*, 88(3):033510, January 2006.

[134] K. S. Takahashi, M. Gabay, D. Jaccard, K. Shibuya, T. Ohnishi, M. Lippmaa, and J.-M. Triscone. Local switching of two-dimensional superconductivity using the ferroelectric field effect. *Nature*, 441(7090):195–198, May 2006. 95

[135] T. Jungwirth, Jairo Sinova, J. Maek, J. Kuera, and A. H. MacDonald. Theory of ferromagnetic (III,Mn)V semiconductors. *Reviews of Modern Physics*, 78(3):809–864, August 2006. 95, 100

[136] Wei Ning, Zhe Qu, You-Ming Zou, Lang-Sheng Ling, Lei Zhang, Chuan-Ying Xi, Hai-Feng Du, Run-Wei Li, and Yu-Heng Zhang. Giant anisotropic magnetoresistance in bilayered La1.2sr1.8mn2o7 single crystals. *Applied Physics Letters*, 98(21):212503, May 2011. 100

[137] Jeng-Bang Yau, X. Hong, A. Posadas, C. H. Ahn, W. Gao, E. Altman, Y. Bason, L. Klein, M. Sidorov, and Z. Krivokapic. Anisotropic magnetoresistance in colossal magnetoresistive La1xSrxMnO3 thin films. *Journal of Applied Physics*, 102(10):103901, November 2007. 100

[138] Run-Wei Li, Huabing Wang, Xuewen Wang, X. Z. Yu, Y. Matsui, Zhao-Hua Cheng, Bao-Gen Shen, E. Ward Plummer, and Jiandi Zhang. Anomalously large anisotropic magnetoresistance in a perovskite manganite. *Proceedings of the National Academy of Sciences*, 106(34):14224–14229, August 2009. 95, 100, 101

[139] A. Bhattacharya, X. Zhai, M. Warusawithana, J. N. Eckstein, and S. D. Bader. Signatures of enhanced ordering temperatures in digital superlattices of (LaMnO3)m(SrMnO3)2m. *Applied Physics Letters*, 90(22):222503, May 2007. 96

[140] C. Aruta, G. Ghiringhelli, A. Tebano, N. G. Boggio, N. B. Brookes, P. G. Medaglia, and G. Balestrino. Strain induced x-ray absorption linear dichroism in $La_{0.7}Sr_{0.3}MnO_3$ thin films. *Physical Review B*, 73(23):235121, June 2006. 96

[141] A-M Haghiri-Gosnet and J-P Renard. CMR manganites: physics, thin films and devices. *Journal of Physics D: Applied Physics*, 36(8):R127–R150, April 2003. 97

[142] M. Egilmez, M. M. Saber, A. I. Mansour, Rongchao Ma, K. H. Chow, and J. Jung. Dramatic strain induced modification of the low field anisotropic magnetoresistance in ultrathin manganite films. *Applied Physics Letters*, 93(18):182505, November 2008. 100

[143] Mercy Mathews, Ferry M. Postma, J. Cock Lodder, R. Jansen, Guus Rijnders, and Dave H. A. Blank. Step-induced uniaxial magnetic anisotropy of La0:67sr0:33mno3 thin films. *Applied Physics Letters*, 87(24):242507, December 2005. 100

[144] A. Khapikov, L. Uspenskaya, I. Bdikin, Ya Mukovskii, S. Karabashev, D. Shulyaev, and A. Arsenov. Magnetic domains and twin structure of the La0.7sr0.3mno3 single crystal. *Applied Physics Letters*, 77(15):2376–2378, October 2000. 100

[145] Amlan Biswas, M. Rajeswari, R. C. Srivastava, T. Venkatesan, R. L. Greene, Q. Lu, A. L. de Lozanne, and A. J. Millis. Strain-driven charge-ordered state in $\{\mathrm{La}\}_{0.67}\{\mathrm{Ca}\}_{0.33}\{\mathrm{MnO}\}_{3}$. *Physical Review B*, 63(18):184424, April 2001. 100

[146] Guixin Cao, Jincang Zhang, Yan Xu, Shipeng Wang, Jian Yu, Shixun Cao, Chao Jing, and Xuechu Shen. Action of strong coupling on steplike magnetization and transport properties in phase-separated manganite. *Applied Physics Letters*, 87(23):232501, December 2005. 102

[147] M. Tokunaga, N. Miura, Y. Tomioka, and Y. Tokura. High-magnetic-field study of the phase transitions of ${R}_{1-x}{\mathrm{Ca}}_{x}{\mathrm{MnO}}_{3}$ ($R=\mathrm{Pr},$ Nd). *Physical Review B*, 57(9):5259–5264, March 1998. 102

[148] Z. Fang, I. V. Solovyev, and K. Terakura. Phase Diagram of Tetragonal Manganites. *Physical Review Letters*, 84(14):3169–3172, April 2000. 103

[149] T. Akimoto, Y. Maruyama, Y. Moritomo, A. Nakamura, K. Hirota, K. Ohoyama, and M. Ohashi. Antiferromagnetic metallic state in doped manganites. *Physical Review B*, 57(10):R5594–R5597, March 1998. 103

[150] R. Kajimoto, H. Yoshizawa, H. Kawano, H. Kuwahara, Y. Tokura, K. Ohoyama, and M. Ohashi. Hole-concentration-induced transformation of the magnetic and orbital structures in ${\mathrm{Nd}}_{1-x}{\mathrm{Sr}}_{x}{\mathrm{MnO}}_{3}$. *Physical Review B*, 60(13):9506–9517, October 1999. 103

[151] Jin-Yeol Kim, Jae-Taek Kim, Eun-Ah Song, Young-Kun Min, and Hiro-o Hamaguchi. Polypyrrole Nanostructures Self-Assembled in Magnetic Ionic Liquid as a Template. *Macromolecules*, 41(8):2886–2889, April 2008. 110

[152] Bert Mallick, Benjamin Balke, Claudia Felser, and Anja-Verena Mudring. Dysprosium Room-Temperature Ionic Liquids with Strong Luminescence and Response to Magnetic Fields. *Angewandte Chemie International Edition*, 47(40):7635–7638, September 2008.

[153] I. de Pedro, D. P. Rojas, J. Albo, P. Luis, A. Irabien, Jess A. Blanco, and J. Rodrguez Fernndez. Long-range magnetic ordering in magnetic ionic liquid: Emim[FeCl 4]. *Journal of Physics: Condensed Matter*, 22(29):296006, 2010. 110

[154] Honghe Zheng, Kai Jiang, Takeshi Abe, and Zempachi Ogumi. Electrochemical intercalation of lithium into a natural graphite anode in quaternary ammonium-based ionic liquid electrolytes. *Carbon*, 44(2):203–210, February 2006. 110

[155] M. Holzapfel, C. Jost, A. Prodi-Schwab, F. Krumeich, A. Wrsig, H. Buqa, and P. Novk. Stabilisation of lithiated graphite in an electrolyte based on ionic liquids: an electrochemical and scanning electron microscopy study. *Carbon*, 43(7):1488–1498, June 2005. 110

Vita

Anthony Thomas Wong was born in 1989. Growing up in North Carolina, Anthony attended Oak Grove Elementary, and Adams Elementary schools in Cary, NC. He then attended Martin Magnet Middle School in Raleigh before attending Cary High School in Cary, NC. Anthony Graduated in June of 2007, after which he enrolled at Virginia Polytechnic Institute and State University. As an undergraduate, he took multiple co-op and internship opportunities in research fields, while earning his bachelors degree in Materials Science and Engineering in December of 2011. After concluding his undergraduate career, Anthony entered into the Materials Science and Engineering department at the University of Tennessee to pursue his doctoral degree, attaining his masters along the way in December of 2016. Anthony achieved his doctoral degree in May of 2017.